Reinforced concrete structures: A review of corrosion mechanisms and advances in electrical methods for corrosion monitoring

Romain Rodrigues, Stéphane Gaboreau, Julien Gance, Ioannis Ignatiadis, Stéphanie Betelu

To cite this version:

Romain Rodrigues, Stéphane Gaboreau, Julien Gance, Ioannis Ignatiadis, Stéphanie Betelu. Reinforced concrete structures: A review of corrosion mechanisms and advances in electrical methods for corrosion monitoring. Construction and Building Materials, 2020, pp.121240. 10.1016/j.conbuildmat.2020.121240 . hal-02979786v1

HAL Id: hal-02979786
https://brgm.hal.science/hal-02979786v1

Submitted on 3 Nov 2020 (v1), last revised 27 Dec 2022 (v2)

HAL is a multi-disciplinary open access archive for the deposit and dissemination of scientific research documents, whether they are published or not. The documents may come from teaching and research institutions in France or abroad, or from public or private research centers.

L'archive ouverte pluridisciplinaire **HAL**, est destinée au dépôt et à la diffusion de documents scientifiques de niveau recherche, publiés ou non, émanant des établissements d'enseignement et de recherche français ou étrangers, des laboratoires publics ou privés.

Reinforced concrete structures: a review of corrosion mechanisms and advances in electrical methods for corrosion monitoring

Romain Rodrigues[a*], Stéphane Gaboreau[b], Julien Gance[a], Ioannis Ignatiadis[b], Stéphanie Betelu[b*]

[a]: IRIS Instruments, 1 avenue Buffon, 45100 Orléans, France.

[b]: BRGM (French Geological Survey), 3 avenue Claude Guillemin, 45060 Orléans Cedex 2, France.

* Corresponding authors:

Romain Rodrigues: rodrigues.irisinstruments@gmail.com

Stéphanie Betelu: s.betelu@brgm.fr

Abstract

Steel corrosion is the main cause of deterioration of reinforced concrete (RC) structures. We provide an up-to-date review on corrosion mechanisms and recent advances in electrical methods for corrosion monitoring. When assessing corrosion mechanism, the inherent heterogeneity of RC structures and the significant effect of environmental factors remain major issues in data interpretations. The steel surface condition and local inhomogeneities at the steel-concrete interface appear to have an important effect on corrosion initiation. Considering uniform corrosion in atmospherically exposed reinforced concrete, the two main influencing factors of the corrosion process are the water content and the pore structure at the steel-concrete interface. However, irrespective of the depassivation mechanism, i.e. carbonation or chloride-induced corrosion, non-uniform corrosion is expected to be the main process for RC structures due to local variations in environmental exposure or the presence of interconnected rebars with different properties. Future studies may then be focused on their effect on macrocell corrosion to gain further insights in the corrosion mechanisms of RC structures. Concerning corrosion monitoring using electrical methods, the half-cell potential technique with potential mapping is accurate for locating areas with a high corrosion risk. Recent developments in the measurement of concrete resistivity have shown that the use of electrical resistivity tomography allows to consider appropriately the inherent heterogeneity of concrete and provides more insights on transport phenomena (e.g. water and salts ingress) in the material. Nevertheless, during the corrosion propagation stage, the polarization resistance remains the most important parameter to be determined as it provides quantitative information of the corrosion rate. If conventional three-electrode configuration methods can supply an accurate determination in the case of uniform corrosion, they often fail in the case of macrocell corrosion in field experiments. Recent advances have shown that a four-electrode configuration without any connection to the rebar can rather be used for the non-destructive testing and evaluation of corrosion. If studies are still required to quantify the corrosion rate, this method appears sensitive to localized corrosion and thus more suitable to field investigations. Finally, the coupling of numerical simulations with complementary electrical and other non-destructive testing methods is essential for consolidating the results to provide a better diagnosis of the service life of RC structures.

Keywords: steel-reinforced concrete; carbon steel; corrosion mechanism; corrosion rate; non-destructive testing.

1. Introduction

Concrete and cement-based materials are among the main man-made materials used world-wide in both civil and industrial structures, due to their high mechanical strength and low porosity. Reinforcement with steel rebars has improved the performance of structural elements without modifying the macroscopic cementitious matrix properties [1]. Properly designed and adapted to its environment, reinforced concrete (RC) is an extremely durable material as the concrete is a protective barrier for the rebars. This allowed the development of RC structures, such as bridges, dams or nuclear powerplants [2–4]. Nevertheless, such materials degrade over time, becoming more fragile.

One of main fragilities is related to corrosion of the steel rebars, an electrochemical process that involves the anodic dissolution of iron and the cathodic reduction of oxygen, the pore solution of concrete acting as the electrolyte. This phenomenon develops under the influence of aggressive agents, e.g. CO_2 and Cl^-, that infiltrate the concrete up to the rebar [5–9]. The degradation of the protective layer formed on steel surface in sound concrete results in accelerated corrosion of the rebar, affecting progressively the performance of RC structures. The resulting corrosion products precipitate and generate tensile stress, promoting the appearance of cracks to an unacceptable level regarding their service life [5–9]. Such degradation can result in the collapse of structures such as bridges or buildings. When the first cracks are noticed on the concrete surface, corrosion has generally reached an advanced stage and maintenance action is required. The continuous aging of structures created several decades ago results in aggravated situations as many operate beyond their service life, drastically increasing the economic impact of corrosion [10,11]. The control of such infrastructures is thus of major importance, requiring reliable monitoring techniques that can be used without disturbing the integrity of the structures.

Several techniques have been developed for understanding the mechanism and kinetics of the corrosion of steel in concrete. Some techniques focus on determining concrete properties for evaluating the ingress of aggressive agents, while others focus on the rebar properties [12–21]. Among such techniques, electrical/electrochemical methods have been widely developed as they allow the evaluation of the corrosion rate, which is essential when determining the need for future maintenance of RC structures once the steel rebar is depassivated. Three main parameters are generally determined for assessing this parameter: corrosion potential, concrete resistivity, and polarization resistance.

This review describes first the constituents of RC structures, i.e. cement-based materials, carbon steel rebar and steel-concrete interface. We then present didactically an up-to-date knowledge of corrosion mechanisms of steel in concrete as a prerequisite to appropriate the different phenomena and evaluate the main factors influencing the corrosion rate. The review is then focused on the use of electrical methods for the non-destructive testing and evaluation (NDT) of corrosion, with the current state-of-the-art monitoring techniques, their advantages and drawbacks, and recent advances in indirect electrical methods which do not required any connection to the reinforcement for the assessment of corrosion, which have been largely ignored in recent reviews. The interest of combining several NDT for field inspection is also developed to overcome the limitation of measuring instantaneous corrosion rates and to improve the estimation of the service life of RC structures. Finally, we present conclusions and perspectives for future researches in corrosion science and engineering.

2. Composition of reinforced concrete structures

2.1. Cement-based materials

Cement-based materials are composed of binder (hydrated cement) and aggregates of different sizes and compositions. Cement is produced by heating a mixture of limestone and raw clay minerals (or other materials of similar bulk composition) [22]. Though OPC was the most common cement-based material used world-wide over the past decades, other cement formulations have been designed to adapt the materials to their environmental setting. Organic and inorganic admixtures act on the workability of cement-based materials or improve their performance. Supplementary cementitious materials (SCMs), such as fly ash or blast furnace slag (BFS) [23,24], are also used as partial replacement of clinker for reducing waste and greenhouse-gas emissions, as the cement industry is one of the largest CO_2 emitters in the world [25]. Such materials differ in their microstructure and macroscopic behaviour, but their description fall outside the scope of this review.

The reaction of cement with water, called hydration, results in the formation of a hydrated cement paste (HCP). The latter is composed of many hydration products, e.g. calcium silicate hydrates (C-S-H) and portlandite $Ca(OH)_2$, but also unhydrated cement particles [26–28]. Over a variable curing period, the cement develops its physical and chemical properties. In laboratory experiments, curing can take place under optimal conditions in terms of relative humidity (RH) and temperature, which allows the definition of standard specimens for research purposes [29]. However, curing conditions are often difficult to control in the field, for which reason a different standard practice has been proposed [30]. Hence, the results obtained from laboratory samples must be used with special care if the objective is to extrapolate them to real structures as their intrinsic properties may significantly differ.

After curing, C-S-H represents ~50-60% of the weight of HCP and is responsible for its cohesion [31]; it consists of lamellar nanoparticles with negatively charged silicate layers compensated by interlayer calcium ions, the charge depending on the calcium-to-silica ratio [32]. Their surface chemistry and inter-particles interaction are the driving force of the cohesive properties of hydrated cement, controlling the interactions with charged molecules [31,33]. The role of confined water in C-S-H micropores was demonstrated through molecular dynamic simulation [34,35]. Because of these points, understanding the distribution of water in C-S-H and their thermodynamic and hydration properties is of prime importance when considering the strength and transfer properties of cement materials [36–41]. Nonetheless, all the hydrates must be considered as they play a role in the cement-paste properties.

Over the service life of a structure, different thermodynamic equilibria between the solid and liquid phases will develop in the cement-based material, governed by both its environmental setting and its degradation level [42]. The solubility of each phase will dictate the composition of the pore water [43]. At an early stage, the pore solution pH is highly alkaline, between 12.5 and 13.5. With the leaching and dissolution of the materials by chemical attacks, portlandite maintains a pH of about 12.5. During the third stage, the pore solution pH is essentially controlled by C-S-H and is buffered in the range 12.5 to 10 [44]. Finally, at later stage, the pH is controlled by all stages of concrete degradation.

At a macroscopic scale, both microstructure and reactivity of hydrates control the physical and chemical reactions affecting the durability of cement-based materials. The microstructure of the cement paste is highly heterogeneous through the coagulation of nanometric hydrates whose heterogeneities range from macroscopic to nanoscopic scales. In addition to the intra-particles (micro) and inter-particles (meso) porosity of hydrates, the microstructure consists of capillary pores which can range from nanometres up to millimetres. The volume and size of these macropores depend upon the water-to-cement (w/c) ratio, the size of the aggregates and the degree of hydration [45–50]; they are mainly interconnected through a mesoscopic pore network. The presence of aggregates in cement-based materials also introduces important changes with the formation of additional porous regions, known as interfacial transition zones (ITZs). As ITZ may in part be caused by artefacts from sample preparation for microscope analysis, e.g. edge rounding, scratches or imperfect cuts, the experimental protocol for specimen preparation must be reported to avoid any misleading [51].

Cracks also are important features in the microstructure of concrete, introducing additional porosity in HCP. Cracks and microcracks are caused by a multitude of different physical and chemical processes, such as mechanical loading, shrinkage, creep, thermal variations, and expansive chemical reactions [22]. To some extent, almost all cementitious materials are affected by one or more of these processes at different times and, consequently, cracks are endemic to the material. A good knowledge of the structure and microstructure of the concrete is thus essential for assessing concrete durability. Notably, the determination of pore throat and pore size distribution is required for assessing the constrictivity and tortuosity of concrete. Both parameters are mainly determined by mercury intrusion porosimetry (MIP) [52], kerosene porosity, or by imaging methods, e.g. backscattered electron (BSE) imaging [28,53–55] and X-ray micro-computed tomography (X-ray µCT) [56,57]. The last technique is also used for estimating the size and distribution of aggregates in the structure. Spectral induced polarization can also provide relevant information on the mean pore size, pore size distribution and connected porosity of low pH concrete [58].

2.2. *Carbon steel reinforcement bars*

The role of steel reinforcement bars (rebars) is to improve the mechanical properties of the structure, as they provide tensile strength, ductility and crack-growth resistance [1]. Several types of rebar can be used, e.g. carbon steel, epoxy-coated steel, galvanized steel, stainless steel and different alloy steels, but only carbon steel is considered in this review. Generally, ribbed rebars are used in RC structures to provide a strong and interlocking connection between steel and concrete.

The chemical composition—metallic and non-metallic elements—of the rebar may vary considerably as several steel grades exist in the world. The distribution of the microstructural phases of steel, e.g. ferrite, cementite, pearlite, martensite, austenite and/or bainite, and the presence of lattice defects or inclusions (e.g. manganese sulphide MnS) can influence corrosion susceptibility, but only few studies are available on this purpose for the corrosion in cement-based materials. If the influence of steel microstructure on corrosion susceptibility has been demonstrated under immersed conditions in simulated concrete pore solution [59–62], the ferritic-martensitic microstructure having generally a better corrosion resistance, the effect of non-uniform water distribution in porous material exposed to atmospheric conditions must be investigated to determine the corrosion susceptibility in concrete.

After hot rolling and forging, a thin and brittle oxide coating called *mill scale* spontaneously forms on steel surface. It is mainly composed of wüstite (FeO), magnetite (Fe_3O_4), hematite (α-Fe_2O_3) and maghemite (γ-Fe_2O_3) [63]. A *native rust* layer later forms during transport, handling and storage of the rebar. Some defects such as cracks, voids and crevices are common between the steel and these initial oxide layers [64]. The composition, thickness and electrochemical properties of both mill scale and native rust are thus very different from one steel to another due to the different manufacturing processes [63–65]. Consequently, even the as-received grade is not well defined, which creates difficulties for ensuring reproducibility of the measurements [65]. If mill scale and native rust can be removed by different processes, e.g. sandblasting, chemical cleaning or mechanical polishing [66], the results from such processes must be used with special care as they are generally not performed for engineered structures.

The role of mill scale and native rust layer on the corrosion resistance of steel in still unclear [67–69]. Some studies indicate that it does not affect the corrosion rate or may have a beneficial effect due to the protective behaviour of the layer in the case of a dense and uniform mill scale [70,71], but most studies affirm that it has a negative effect on the corrosion rate as it inhibits the development of an effective passive layer on the rebar or decreases its electrical resistance [72–77]. It was also shown that the corrosion rate is greater for rebars exposed to natural weathering (pre-rusted rebars) than for the as-received rebars [78]. The initial surface state of the rebar and the distribution of native rust are thus major parameters controlling the corrosion susceptibility, and a non-uniform mill scale layer can create weak points for corrosion initiation [79,80]. Hence, as for cement-based materials, a detailed description of the rebar grade, composition, microstructure and initial surface condition is necessary for a correct interpretation of the data and the development of database for the assessment of corrosion mechanisms.

2.3. Steel-concrete interface

The steel-concrete interface is the most important part of the structure when it comes to determining corrosion mechanisms and corrosion rates of steel rebar [63,80,81]. The embedding of steel in concrete is intended to protect the steel from corrosion. Indeed, in the alkaline medium of the pore solution, a passive film forms spontaneously on the steel surface during the first days/weeks of exposure [82–84]. Such passivation is initiated by the formation of adsorbed species ($FeOH_{ads}$ and $Fe(OH)^+_{ads}$), $HFeO_2^-$ and $Fe(OH)_2$ [85], and the aging of this passive film results in a progressive decrease in the corrosion rate to values below 0.1 µm year^{-1} (often described as “no corrosion takes place”). This change is attributable to thickening of the film and to the decrease in Fe^{2+} content in its inner layer [86,87], which corresponds to the oxidation of magnetite Fe_3O_4 to Fe(III) oxide and oxyhydroxide, e.g. Fe_2O_3 or FeOOH [88–90]. The passive film shows an *n*-type semiconductive behaviour [91,92], but this reaction results in decreasing the electronic conductivity of the film, as Fe(III) oxides are less conductive than magnetite [90]. The resulting passive film is about 10-15 nm thick and is mainly composed of iron oxides and oxyhydroxides, with a progressive increase in valence state and in hydroxide content from inner to outer interface [87,93]. Some elements of the cement paste, e.g. Ca^{2+}, Na^+ and K^+, can also occur in the passive film, affecting its properties [94,95].

The concrete part of the interface can be seen as another ITZ [63]. The casting direction and orientation of the rebar in the structure affect the distribution of $Ca(OH)_2$ and the porosity of HCP at the steel-concrete interface. For example, the area under a horizontal rebar is exposed to very different conditions, having a $Ca(OH)_2$ content close to 0 and a much higher porosity than the bulk concrete [96,97]. Conversely, for vertical rebars, the steel-concrete interface is relatively uniform without obvious macroscopic defects [97,98]. This difference is explained by the settlement, segregation and bleeding of fresh concrete that can result in the accumulation of defects under horizontal rebar [98]. When several horizontal rebars are present in the structure, the upper ones have generally more defects, which is known as the top-bar effect. Special attention must be paid during concrete pouring to limit the formation of these defects that can be preferential seat for corrosion initiation. Other defects, such as cracks, slips and separations, are the result of tensile load on the structure [63]. They all affect the quality of the interface, and thus the corrosion rate [99]. The coalescence of ITZs and cracks can form interconnected porous channels that dramatically increase concrete permeability, creating preferential pathways for the ingress of aggressive agents to the rebar. Finally, the use of spacers and the presence of welding spots can induce supplementary local heterogeneities.

The local characteristics of the steel-concrete interface are important parameters as the latter is the seat of the corrosion process. Several techniques can be used to determine the chemistry and microstructure of the interface, such as EDS and BSE imaging [96,100,101]. Special care must be done during sample preparation for such analyses to reduce as much as possible any damage to the steel-concrete interface [102,103]. Alternatively, X-ray µCT can be used to examine non-destructively the rebar/cement contact and any heterogeneities such as air voids (Fig. 1).

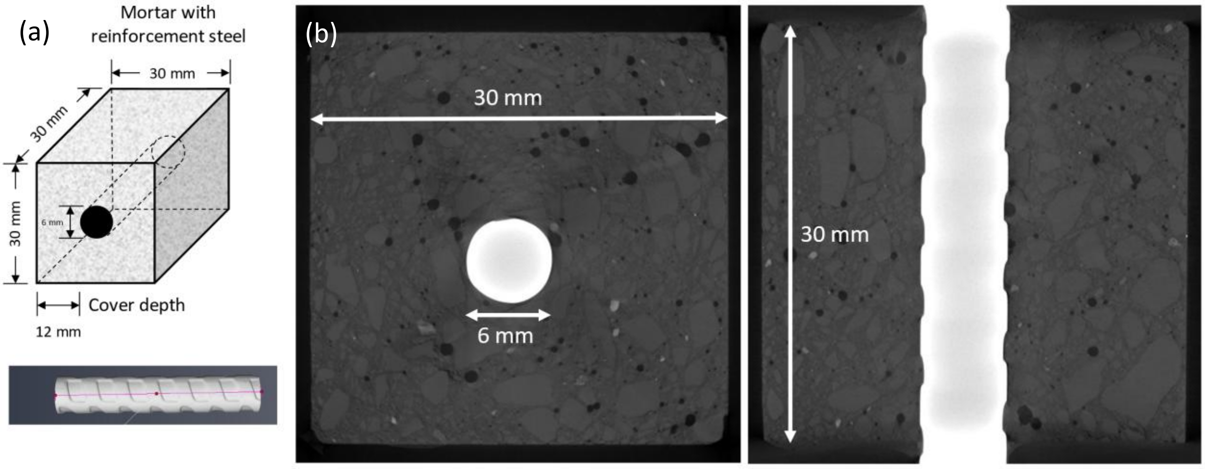

Figure 1. (a) Schematic representation of a mortar sample [cement (CEM I 52.5 R, Lafarge)=25 wt%, sand (0-4 mm)=75 wt%, w/c ratio=0.5] with one ribbed black carbon steel rebar (Φ=6 mm). (b) X-ray micro-computed tomography 2D slices acquired under 140 kV and a 26 µm voxel size. The slices show concrete heterogeneities (shape and orientation of the aggregates, presence of air bubbles), the shape of the rebar and the structure of the steel-concrete interface. Courtesy: S. Gaboreau.

3. Corrosion mechanisms of carbon steel in concrete

As proposed by Tuutii [104], the service life of RC structures can be divided into two main time periods: an initiation stage and a propagation stage. The first corresponds to the ingress of aggressive agents—CO_2 and chloride—in the concrete to the rebar, resulting in a progressive disruption of the passive film on the steel surface. The propagation stage is the active state of corrosion until the degree of corrosion reaches the damage limit tolerated by building standards. Generally, steel corrosion is considered in a passive state if the current density is below 0.1 $\mu A\ cm^{-2}$, and in the active state for values over 1 $\mu A\ cm^{-2}$ [105]. Based on Tuutii's model, other models considered the change in corrosion rate during the service life of reinforced concrete [106–108], or included additional stages for differentiating rust expansion, cover cracking and spalling/delamination in the definition of service life (Fig. 2) [109–111]. However, the level of deterioration is not linear as concrete cracking and spalling may accelerate the corrosion rate, whereas the production of corrosion products in cracked concrete may fill the pores, thus decreasing the corrosion rate.

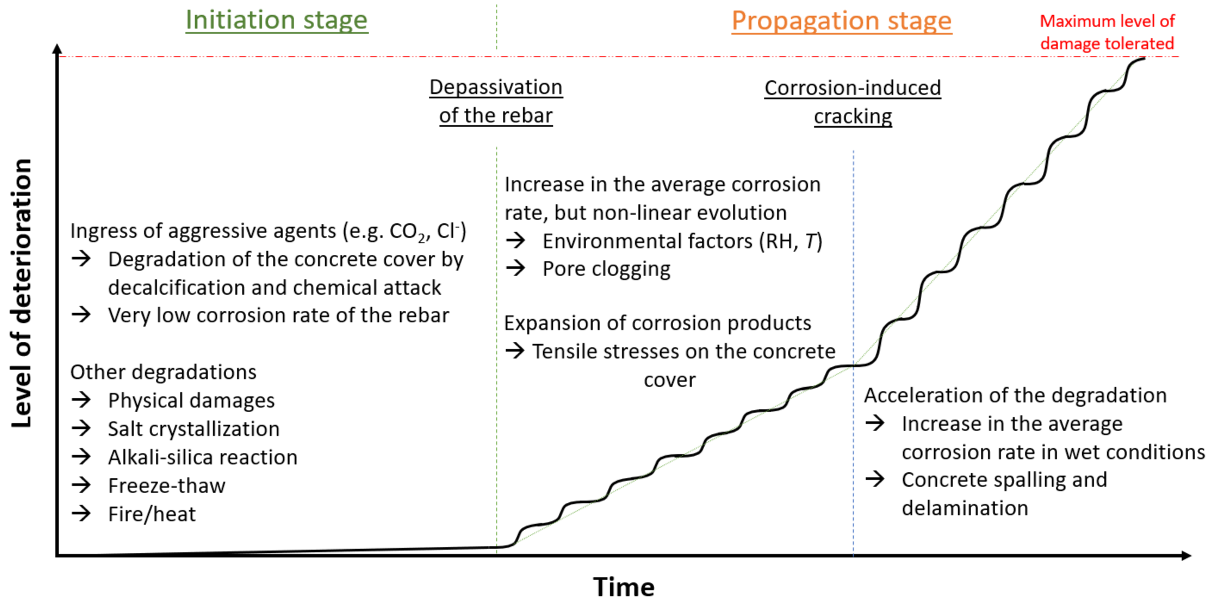

Figure 2. Schematic representation of the service life of RC structures, adapted from Tuutti's diagram [106].

Estimating the service life of reinforced concrete requires knowledge of the two main stages of steel corrosion in concrete [112]. Notably, models coupling transport and electrochemical processes are required for improving the prediction of service life [111,113]. Hereafter we discuss the thermodynamic and kinetic aspects of corrosion, the mechanisms of carbonation- and chloride-induced corrosion—here developed separately but locally occurring simultaneously—and the formation and consequence of iron corrosion products on the durability of RC structures. Table 1 summarizes the main conclusions of this section.

Table 1. Summary of the main conclusion regarding mechanisms of carbonation- and chloride-induced corrosion of steel in concrete.

Mechanism	**Corrosion initiation**	**Corrosion propagation**	**Main corrosion products**
Carbonation	* Ingress of CO_2 from the atmosphere Higher penetration rate in the 50-70% RH range Dissolution in water as carbonic acid * Decalcification of concrete Reaction with Ca-bearing hydrated phases Non-uniform carbonation front Decrease in the pH of the pore solution * Depassivation of the rebar	* Corrosion rate is mainly influenced by the water content and the pore size distribution in the vicinity of the rebar for atmospherically exposed RC structures * Volume expansion of corrosion products Pore clogging Tensile stress in the concrete cover Formation of corrosion-induced cracks Increase in the average corrosion rate Concrete spalling and delamination	* Intermediate products: Chukanovite $Fe_2(OH)_2CO_3$ Carbonate green rust GR(CO_3^{2-}) Siderite $FeCO_3$ * Final products: Magnetite Fe_3O_4 Goethite α-FeOOH Lepidocrocite γ-FeOOH
Chloride	* Ingress of Cl^- from marine environment or the use of de-icing salts Non-uniform penetration of Cl^- in the material up to the rebar Series of depassivation/repassivation until the chloride content is high enough * Depassivation of the rebar	* Autocatalytic mechanism of pitting Deepest pits are generally observed in the vicinity of interfacial air voids Formation of macrocell with high corrosion rates * Volume expansion of corrosion products Pore clogging Tensile stress in the concrete cover Formation of corrosion-induced cracks Increase in the average corrosion rate Concrete spalling and delamination	* Intermediate products: Ferrous hydroxychloride Chloride green rust GR(Cl^-) * Final products: Magnetite Fe_3O_4 Goethite α-FeOOH Lepidocrocite γ-FeOOH Feroxyhyte δ-FeOOH Akaganeite β-FeOOH (Cl^- excess)
Combined	See above Carbonation of Friedel's salt and other chloride-binding phases will release free Cl^- [114–116]	See above The corrosion rate is higher when both Cl^- and CO_2 act together as compared to their individual contribution [117,118]	See above

3.1. Electrochemical, thermodynamic and kinetic aspects of corrosion

The corrosion of steel in concrete is an electrochemical process that involves the anodic dissolution of iron and, generally, the cathodic reduction of oxygen [119,120]. Depending on the availability of oxygen and the pH near the steel surface, it is also possible to observe the reduction of proton [121]. Finally, an electrical connection between the anode and the cathode is required for transferring the electrons, and an electrolytic environment for transferring the ions in solution (Fig. 3).

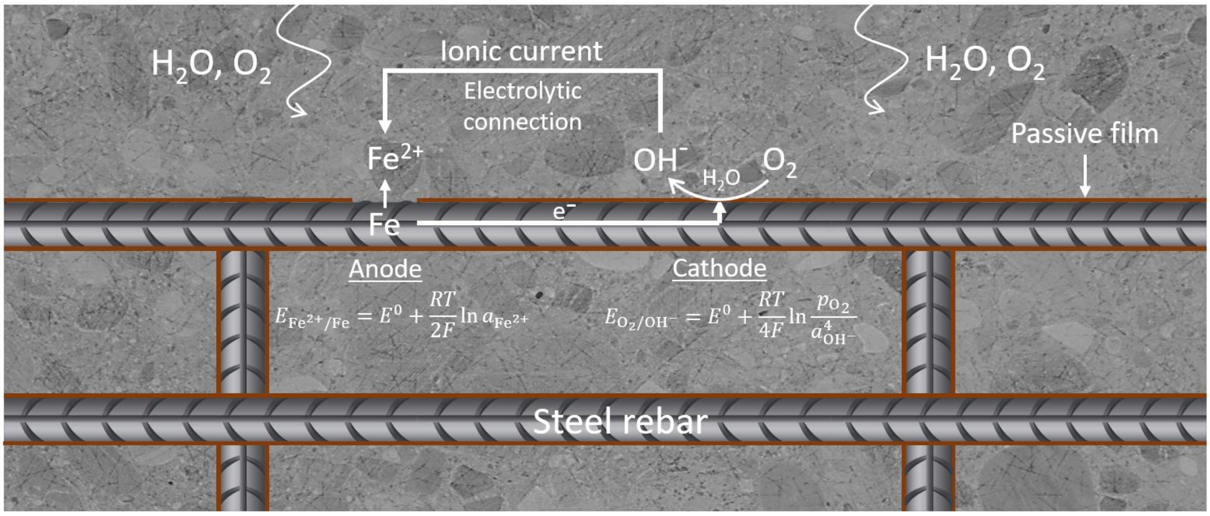

Figure 3. Schematic representation of the corrosion of steel in concrete, involving iron oxidation, oxygen reduction, and the electrical connection and ionic current between the anodic and cathodic sites.

The general principle of steel corrosion in concrete can be explained with the stability diagram of the Fe/H_2O system (potential-pH or Pourbaix diagram) [122]. Depending upon the experimental conditions, i.e. total Fe content and temperature, the predominance of species can be quite different (Fig. 4). As shown in section 2.2, the thin (~10-15 nm) and passive film developed on the steel surface is preserved under alkaline conditions (passivation domain). If this passive layer remains intact, iron is in the passivation domain and corrosion is slow (less than 0.1 µA cm^{-2}, "passive rebar"). Unfortunately, the continuous degradation of reinforced concrete in environments containing CO_2 and Cl^- affects the integrity of the passive layer. Iron changes to the corrosion domain, which results in the acceleration of corrosion (higher than 1 µA cm^{-2}, "actively corroding rebar") and the progressive loss of steel cross section associated with the formation of corrosion products.

The electrochemical kinetics of corrosion are given by the Butler-Volmer equation (Eq. 1) [123]:

$$i = i_0 \left\{ \exp\left[\frac{\alpha_a nF}{RT}(E - E_{corr})\right] - \exp\left[-\frac{\alpha_c nF}{RT}(E - E_{corr})\right] \right\} \qquad \text{(Eq. 1)}$$

where i is the current density (A m^{-2}), i_0 is the exchange current density or corrosion current density i_{corr} (A m^{-2}), α_a and α_c are the anodic and cathodic charge transfer coefficient, respectively, n is the number of electrons exchanged in the reaction, F is the Faraday constant (96485 C mol^{-1}), R is the universal gas constant (8.314 J mol^{-1} K^{-1}), T is the absolute temperature (K), E is the electrode potential (V) and E_{corr} is the corrosion potential (V). The term $\frac{\alpha nF}{RT}$ is equivalent to the term $\frac{\ln(10)}{\beta}$, where β is the Tafel slope (special case of the Butler-Volmer equation, see section 4.3). As it will be developed in the following sections, the corrosion rate depends upon:

- the water content [124,125]. When RH increases to ~70%, the adsorption of water vapour occurs on external surfaces of C-S-H [38], and the resulting water film is thin and can be considered electrically inactive (high resistance to ionic transport). The further increase in RH from ~70 to ~95% enables the adsorption of multilayer water molecules and the filling up of mesopores [38], decreasing the resistance to ionic transport in concrete;
- the temperature, which affects the kinetic parameters of the corrosion process, such as Tafel slopes, exchange current density and equilibrium potential [126,127];
- the pore size distribution [124,125] and the presence of interfacial voids [128];
- the transport properties of aggressive agents in concrete, notably their diffusion coefficients [129,130], and the availability of dissolved oxygen in the cathodic areas, i.e. presence of a cathodic limited current or not [131];
- the transport of Fe^{2+} and the nature and distribution of precipitated corrosion products [132].

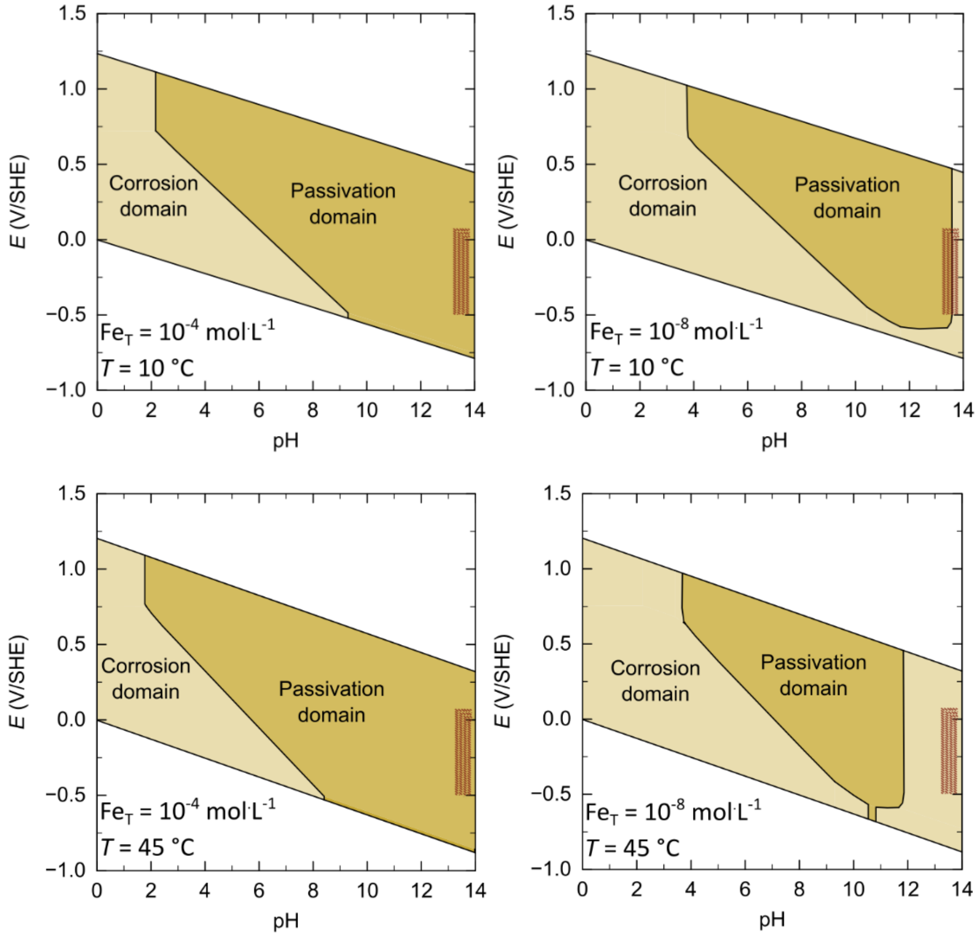

Figure 4. Simplified stability diagrams of the Fe/H_2O system indicating the corrosion domain (dissolved iron species) and the passivation domain (precipitated iron species) in the domain of water stability for two total iron content and two temperatures. The hatched area represents the pH and potential range generally reported for carbon steel in sound OPC concrete. These predominance diagrams were obtained with PhreePlot software and the Thermoddem database [133]. Fe-bearing phases considered for calculation were $Fe(OH)_2$,

magnetite (am), ferrihydrite (6L), goethite and lepidocrocite, which are the main corrosion products of steel in concrete.

3.2. Carbonation-induced corrosion

3.2.1. CO_2 penetration and concrete carbonation

Atmospheric carbon dioxide ($pCO_2 \approx 0.04\%$) can penetrate into cement-based material mainly by absorption into interconnected capillary pores on the concrete surface and by diffusion in depth through the pore network and microcracks [134]. CO_2 diffusion coefficient increases when increasing the water-to-cement ratio as the total porosity of the cement paste increases. The rate of CO_2 penetration is highest at low RH, when the pores are mostly air-filled [135–137]. The presence of salt in concrete also contributes to block the ingress of CO_2 due to pore clogging [138]. During its ingress, CO_2 dissolves in the pore water and forms carbonic acid H_2CO_3. According to the speciation of CO_2 [139], carbonic acid dissociates in HCO_3^- and CO_3^{2-} depending on the pH of the pore solution.

Carbonation of concrete is the reaction between CO_2 and Ca-bearing hydrated phases, e.g. portlandite, C-S-H and ettringite. The reaction kinetics appear governed by the exposure conditions [134,140]. All reactions with hydrated phases occur in solution and are therefore more important and more rapid in saturated concrete. However, as the rate of CO_2 penetration is highest at low RH, it is often reported that the carbonation rate is highest in the 50-70% RH range [135,141]. Environmental exposure affects the rate of carbonation; for example, the more rainy days, the lower the carbonation rate [142]. This rate depends also on concrete porosity, and thus on the w/c ratio. A low w/c ratio and a high compressive strength are required to limit as much as possible the carbonation depth, especially in severe environmental conditions [138,143,144]. It is also dependent on the temperature, the CO_2 partial pressure, the alkaline reserve in the concrete (CO_2 binding capacity), and the presence of cracks [134,145,146]. All these parameters are required for an accurate modelling of carbonation processes in RC structures [147–150].

Carbonation induces changes in mechanical properties and microstructure of cement-based materials [134,151,152]. It results notably in the formation of calcium carbonates $CaCO_3$, calcite being the most stable phase [134]. For OPC concrete, its precipitation results in a lower permeability through total porosity reduction [153] and loss of interconnectivity due to pore clogging as $CaCO_3$ occupies a larger volume than $Ca(OH)_2$ [154]. However, as the capillary porosity increases [155], the ionic migration through the cement paste can be increased because of carbonation. But as shrinkage and cracking of the concrete can occur in parallel, it is difficult to predict the change only due to carbonation [134].

As the carbonation of concrete exposed to atmospheric conditions is a slow process, especially for OPC concrete (a few tens of millimetres in 20 years [156]), accelerated laboratory tests are generally performed in an CO_2-rich atmosphere under conditions where the rate of carbonation is maximum (≈50-70% RH). As shown by several authors, these accelerated tests are representative of the natural carbonation in terms of changes in mineralogy, microstructure, water retention and cracking as long as the CO_2 content is low (pCO_2 <3-4%), even if carbonation is only partial and the formation of metastable $CaCO_3$ phases, i.e. aragonite and vaterite, is promoted instead of calcite [157,158].

3.2.2. *Depassivation and corrosion mechanisms*

Despite possible self-healing of concrete, carbonation is responsible for a decrease in pH of the pore solution from above 13 to below 9, which results in dissolution of the passive layer of the rebar when the carbonation front reaches its surface [150,159]. According to the Pourbaix diagram (Fig. 4), the process will progressively change from the passivation domain to that of corrosion [160,161]. It is commonly assumed that the corrosion induced by carbonation is generalized and relatively homogeneous [92]. Considering this case, steel is uniformly depassivated, and the anodic and cathodic areas are located at adjacent locations. The term ‘microcell corrosion’ is used for describing this situation [162]. However, because of the heterogeneous structure of concrete (cracks, pore size distribution and interconnectivity), the carbonation front is seldom perfectly uniform on RC structures, and a spatial variability in the carbonation depth near the rebar can be observed [163]. The local variation in indoor and outdoor exposure is also responsible for the steepness of the reaction front [164]. This non-uniformity will create different steel-concrete interface along the same rebar, allowing the formation of ‘macrocell corrosion’ [156]. In addition, the presence of load-induced cracks will affect the steel-concrete interface independently of the crack-opening size, promoting local carbonation and damage of the interface [165]. In structures where steel rebars with different conditions are interconnected, macrocell corrosion is thus expected to be the main corrosion process [162,166]. It is, however, still important to consider both microcell and macrocell components, as the neglect of one of these components may result in underestimating the degree of corrosion [167–169]. A schematic representation of the supposed mechanism of carbonation-induced corrosion is shown in Fig. 5.

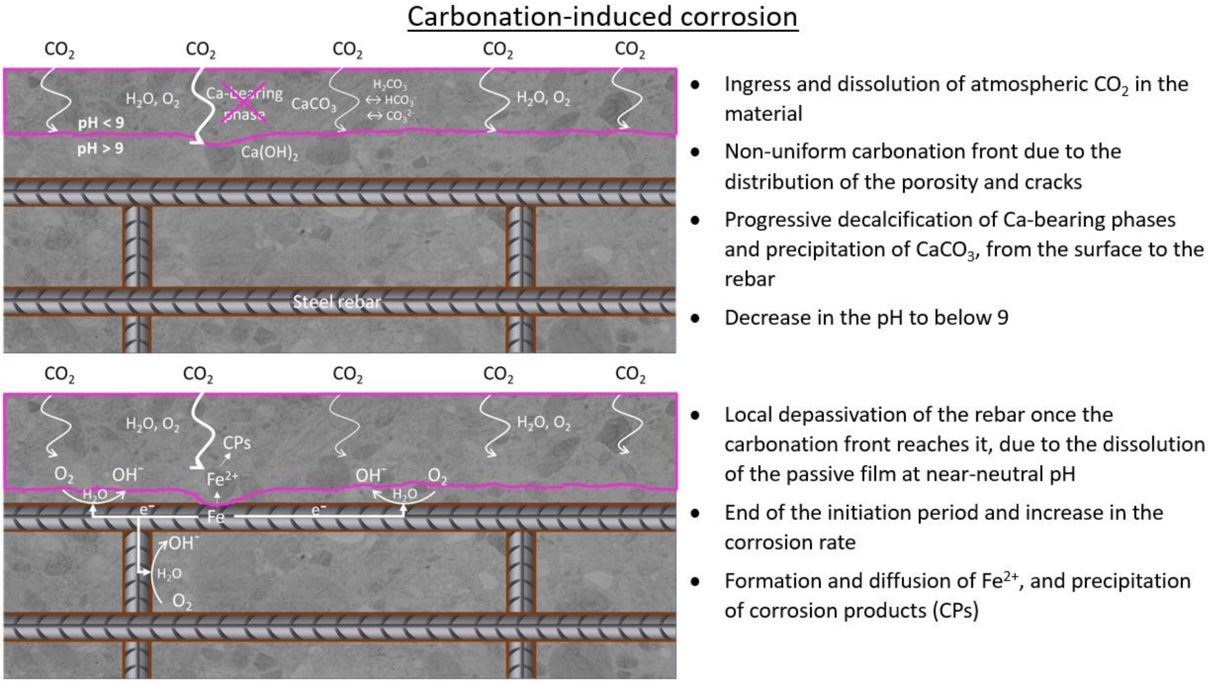

- Ingress and dissolution of atmospheric CO_2 in the material
- Non-uniform carbonation front due to the distribution of the porosity and cracks
- Progressive decalcification of Ca-bearing phases and precipitation of $CaCO_3$, from the surface to the rebar
- Decrease in the pH to below 9

- Local depassivation of the rebar once the carbonation front reaches it, due to the dissolution of the passive film at near-neutral pH
- End of the initiation period and increase in the corrosion rate
- Formation and diffusion of Fe^{2+}, and precipitation of corrosion products (CPs)

Figure 5. Schematic representation of the mechanism of carbonation-induced corrosion of steel in concrete according to the literature cited in the text.

The evolution of the corrosion rate in carbonated concrete is still not fully understood. For each concrete composition, it is highly dependent upon water content and pore size distribution [170]. Different degree of saturation and porosity could thus explain the different corrosion rates observed in carbonated concrete. Some authors reported that the corrosion rate increases up to 90-95% RH before decreasing due to a limitation of the oxygen availability at high RH, indicating the presence of a cathodic limited current [104,129,171]. However, other authors reported that the corrosion rate increases continuously up to 99% RH [124,125,170]. Even at high RH, the material is hardly fully water-saturated as saturation cannot happen only by capillary condensation or capillary suction in large pores (the size being dependent on the pore geometry). This suggests that cathodic control of the corrosion rate due to a limited availability of O_2 is relevant only under long-term immersion, i.e. when all gaseous and dissolved O_2 is depleted in concrete [124]. This confirms that the two main influencing factors of the corrosion rate of steel in atmospherically exposed RC structures are the water content and the pore structure [125]. Consequently, corrosion is under activation control: the corrosion rate increases during wetting exposure until the electrochemically active surface is water-filled, and then decreases during drying exposure [172]. This mechanism controlling the corrosion rate has been proposed for uniformly depassivated rebars in very thin samples. Further studies are required to confirm the validity of the kinetics of iron corrosion for larger cover depth and when the macrocell component is also considered, as non-uniform corrosion is expected on real structures.

3.3. Chloride-induced corrosion

3.3.1. Chloride penetration

The presence of chloride in the concrete can result from chloride-contaminated components of aggregates or contaminated construction water, or by diffusion from the environment, e.g. exposure to a marine environment (e.g. XS microenvironment with wetting/drying cycles) or the use of de-icing salts (i.e. $CaCl_2$, $MgCl_2$, NaCl) in winter [7]. The penetration of chloride occurs mainly through capillary pores as free chlorides Cl^- by capillary suction, diffusion and permeation [7]. Thus, the initiation time of corrosion strongly depends upon transport parameters, such as the diffusion coefficient of total chloride in concrete [173].

It is, however, difficult to predict correctly this parameter as it may be influenced by many others. First, the diffusion is affected by pore size distribution and pore interconnectivity in the concrete, which is related to the w/c ratio. It is recommended to use a low w/c ratio (0.4-0.5) for increasing the length of the initiation stage, as the total porosity will be decreased [174]. Second, a part of the free chlorides can be physically adsorbed on different hydrates such as C-S-H and monosulfoaluminates (AFm), or can chemically react with other phases such as tri-calcium aluminate (C_3A) to form Friedel's salt when the chloride content is sufficient [175,176]. Physical adsorption depends mainly on the specific surface area of the cement paste, while chemical adsorption through formation of Friedel's salt is mainly related to the monocarboaluminate content in the paste [177]. SCMs with high alumina and calcium content can also play a role in the chloride binding capacity, and thus on the durability of RC, by limiting Cl^- ingress to the rebar [177]. Finally, diffusion of Cl^- is affected by water content, temperature, and the properties of the electrical double layer [176,178,179]. The diffusion coefficient varies also in the ITZs of concrete as a function of their volume and tortuosity [180]. As for CO_2 and other aggressive species, the presence of cracks in the concrete or the presence of defects at the steel-concrete interface may provide further preferential paths for the ingress of chloride to the steel surface [181–184]. Irrespective of the factors affecting chloride penetration, determining the rate of Cl^- ingress is required for modelling the service life of the initiation stage of corrosion [185–187].

For accelerating the rate of Cl^- ingress and thus to initiate more rapidly chloride-induced corrosion, several procedures were investigated, e.g. mixing chloride salt in the cement paste or the electromigration/rapid chloride permeability test (RCPT). However, the results obtained by mixing chloride salt directly in the cement paste can only be used for determining the effect of contaminated aggregates or water, as the passive film will not form properly on the rebar [168] and the hydration products will be different, affecting the microstructure of the concrete [65]. RCPT can also affect the concrete microstructure [188] and thus cracks formation. Thus, the results obtained from accelerated tests must be used with care if they aim at understanding corrosion mechanisms.

3.3.2. Depassivation and corrosion mechanisms

As for carbonation-induced corrosion, there still is a lack in the physical understanding of the depassivation mechanism of steel exposed to chloride ions [92,187]. Two models are generally proposed: the ion exchange model [189] and the point defect model [190]. In the first one, depassivation is the result of the adsorption and ingress of Cl^- through the outer film layer and the progressive thinning of the inner film until dissolution. In the second one, chloride ions remain adsorbed on the film surface and act as a catalyst in the formation of Fe vacancies on the oxide/electrolyte interface, which then diffuse to the oxide/metal interface while O vacancies diffuse in the opposite direction. The combination of Fe vacancies results in the formation of voids and thus in depassivation of the rebar. It appears that the lattice structure of this film and the presence of defects strongly affect the depassivation mechanism [191]. Recent experiments of steel corrosion in simulated concrete pore solutions have shown the modification of the structure and electronic properties of the passive film exposed to chloride. Notably, an increase in the Fe^{3+}/Fe^{2+} ratio was observed in association with a decrease in film thickness [91,93,192–194]. The donor density N_D of the passive film increases in the presence of chloride, resulting in a higher electric conductivity and thus lower corrosion resistance of the film, suggesting the incorporation of chloride ions in the passive film [195]. However, molecular dynamics and density functional theory simulations support the point defect model, as no ingress of chloride has been observed in any simulation [196,197].

It is often reported that a minimum chloride content is required for observing the depassivation of steel, so-called the critical chloride content or the chloride threshold value C_{crit}. It is expressed either as the total chloride content relative to binder weight [198], or as the chloride ion activity relative to the pH of the pore solution [199]. Even if only free chlorides are suspected to cause steel corrosion [200], chlorides bounded onto solid phases represent a potential reservoir of free chlorides for corrosion [198]. This is notably observed in the case of the carbonation of chloride-contaminated concrete as carbonation decreases the chloride-binding capacity of hydrates [116,201]. C_{crit} ranges from 0.04 to 8.34% by binder weight, or from 0.01 to 45 in terms of $[Cl^-]/[OH^-]$ molar ratio [199]. It depends on many parameters such as RH, temperature, the pH of the pore solution, local characteristics at the steel-concrete interface and the exposed area of rebar [64,77,202–208]. Though the concept of the chloride threshold value is well accepted, it does not allow an accurate estimation of service life in all cases, even with complex transport models [187,209]. In addition, C_{crit} values obtained from small-scale laboratory samples are hardly applicable to real structures as the preparation conditions are not as well controlled in the field [210] and local inhomogeneities at the steel-concrete interface create a size effect [211]. A test method for mimicking realistic conditions in laboratory specimens is still required [65]. If the weakest-link theory is a suitable option to consider the size effect of corrosion [211], a more practical solution consists in measuring C_{crit} value on samples taken from existing structures. This overcomes the limited applicability of laboratory data and provides case-specific input data to improve the prediction of the service life of the investigated structure [187].

Once the passive film is locally disrupted, anodic dissolution occurs if the water content and oxygen availability are sufficient for the cathodic reduction [212,213]. Due to the localized presence of chloride in the concrete, iron dissolution generates small pits though the surrounding steel surface still retains its passive film. Chloride ions are attracted to the metal dissolution sites for maintaining electroneutrality [214], resulting in the enhancement of iron solubility in the pit due to the formation of iron chlorocomplexes and chloride green rust GR(Cl^-) [215]. Pit stability depends upon the competitive migration between Cl^- and OH^-, which depends on the mobility and concentration of both ions. In the case of insufficient Cl^-, a depassivation/repassivation sequence is expected to occur due to the precipitation of iron(II) hydroxide inside the pit [216]. A sufficient $[Cl^-]/[OH^-]$ ratio is thus needed for achieving stable pit growth. After iron dissolution, the hydrolysis of ferrous iron ions creates local acidification in the pit [217,218] and iron chloride ions $Fe(H_2O)_{(n-m)}Cl_m^{(z-m)+}$ will diffuse outside the pit where they will be dissociated being no longer stable under higher pH conditions. Due to the presence of well-defined anodic and cathodic areas, chloride will migrate back to the anode for further chloride attack, while ferrous iron ions will migrate to the cathode in an oxygen-rich region, where it will precipitate. As a result, an aggressive microenvironment is preserved in the pit, and an autocatalytic process explains the corrosion process in chloride-contaminated concrete. A schematic representation of the supposed mechanism of chloride-induced corrosion of steel is shown in Fig. 6.

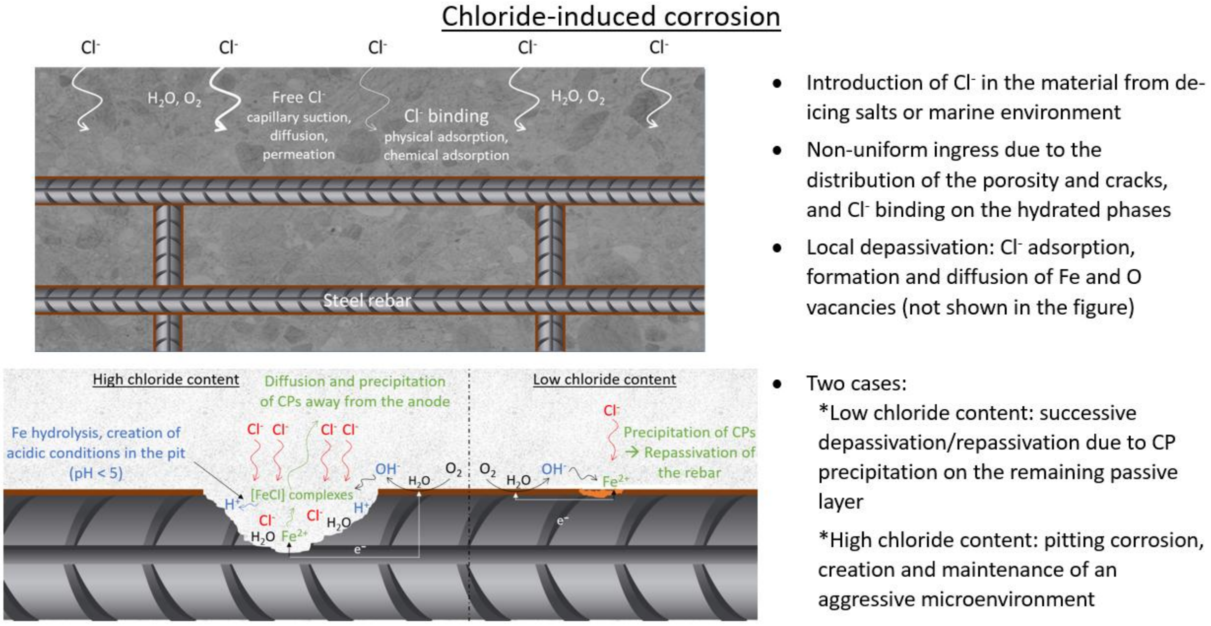

- Introduction of Cl^- in the material from de-icing salts or marine environment
- Non-uniform ingress due to the distribution of the porosity and cracks, and Cl^- binding on the hydrated phases
- Local depassivation: Cl^- adsorption, formation and diffusion of Fe and O vacancies (not shown in the figure)
- Two cases:
  *Low chloride content: successive depassivation/repassivation due to CP precipitation on the remaining passive layer
  *High chloride content: pitting corrosion, creation and maintenance of an aggressive microenvironment

Figure 6. Schematic representation of the mechanism of chloride-induced corrosion of steel in concrete according to the literature cited in the text.

Macrocells with very high corrosion rates are expected in chloride-induced corrosion [219], resulting in important local thinning of steel depending on concrete resistivity [216], driving voltage and cathode-to anode ratio [216]. The growth of anodic sites is more rapid close to the anode/cathode boundary than deeper down in the centre of the pit, due to the non-uniform distribution of current densities [123]. Hence, the extension of the pit is greater across the surface than in depth and the ratio between maximum and average corrosion depth, also called the “pitting factor”, ranges between 2.5 and 10 [220,221]. Corrosion should thus be measured over the entire defective area to predict accurately the mechanical behaviour of a corroded structure [222].

In marine environments, in which RC structures are partially immersed, the cathode-anode distance is an important parameter in the corrosion process. Indeed, it has been shown that the macrocell corrosion current can be provided by a cathode located at large distances from the anode [223,224]. Experiments and numerical simulations have shown that a non-negligible current can be provided by cathodes located in unsaturated zones up to several meters away from the anodic area, depending on the geometry of the structure and its resistivity, which was here considered uniform [224]. Hence, even if O_2 is depleted near the anodic areas, the cathodic reaction may not be the rate-determining step of corrosion as it can occur far away from them. Nonetheless, resistivity differs in immersed zones compared to tidal and unsaturated zones [225], affecting the distribution of the current between anodic and cathodic areas. Further studies are thus required to gain more insights on this macrocell current by considering representative gradients of concrete resistivity in marine environment.

3.4. Nature and reactivity of corrosion products and their impact on durability of the material

Different corrosion products (CPs) are observed in RC structures. Table 2 lists possible CPs in concrete with their volume expansion [5,214,226,227].

Table 2. List of possible iron corrosion products in concrete with their volume expansion (NC=unknown).

Corrosion products	Formula	Valence	Volume expansion
Iron(II) hydroxide	$Fe(OH)_2$	Fe(II)	3.7
Chukanovite	$Fe_2(OH)_2CO_3$		NC
Siderite	$FeCO_3$		NC
Ferrous hydroxychloride	$\beta\text{-}Fe_2(OH)_3Cl$		NC
Chloride green rust	$Fe^{II}_3Fe^{III}(OH)_8Cl, 2\ H_2O$	Fe(II-III)	NC
Carbonate green rust	$Fe^{II}_4Fe^{III}_2(OH)_{12}CO_3, 2\ H_2O$		NC
Sulphate green rust	$Fe^{II}_4Fe^{III}_2(OH)_{12}SO_4, 8\ H_2O$		NC
Magnetite	Fe_3O_4		2.1
Hematite	$\alpha\text{-}Fe_2O_3$	Fe(III)	2.1
Maghemite	$\gamma\text{-}Fe_2O_3$		2.4
Iron(III) hydroxide	$Fe(OH)_3$		4.2
Ferrihydrite	$Fe_2O_3, 3\ H_2O$		6.5
Goethite	$\alpha\text{-}FeOOH$		3.0
Akaganeite	$\beta\text{-}FeOOH$ $(\beta\text{-}FeO_{1-x}(OH)_{1+x}Cl_x)$		3.5
Lepidocrocite	$\gamma\text{-}FeOOH$		3.2
Feroxyhyte	$\delta\text{-}FeOOH$		2.8

Iron dissolution results first in the production of ferrous iron Fe^{2+} in solution. Then, iron(II) hydroxide $Fe(OH)_2$ is assumed to be the main precursor of precipitated CPs [218]. If several intermediates can then be formed, they are rapidly oxidized in the presence of oxygen. With a low oxygen supply, partial oxidation is common, resulting in the formation of magnetite Fe_3O_4. With a high oxygen supply, complete oxidation results in the formation of Fe(III) oxides and oxyhydroxides, collectively referred to as “rust”. The occurrence of CPs depends mainly on the nature of the rebar and the environmental parameters.

The presence of the rust layer is of great importance as it is directly implied in the mechanism of steel corrosion. It acts as a porous electrode where oxygen reduction can occur [228]. Notably, the exchange current density of O_2 reduction is higher where rust is present as compared to a surface where only mill scale occurs [229]. The reduction of rust, notably FeOOH, can also be seen as the cathodic reaction related to iron dissolution [230,231]. Due to the difference in electric conductivity and morphology of the different CPs, determining their local distribution is important as it can influence the rate-determining step of corrosion [232].

3.4.1. Nature and distribution of CPs in carbonation-induced corrosion

In carbonated media, chukanovite $Fe_2(OH)_2CO_3$, siderite $FeCO_3$ and carbonate green rust $GR(CO_3^{2-})$ are expected to form as intermediates, and the oxidation of chukanovite results in the formation of lepidocrocite and goethite [233]. Feroxyhyte can also be observed in addition to these two products [234]. Because of the very low solubility of iron oxyhydroxides at near-neutral conditions in carbonated concrete, they tend to precipitate in the porosity at the vicinity of the rebar to form a ‘corrosion layer’ [218]. The accumulation of precipitates under confined conditions will cause an expansive pressure, resulting in cracks formation in concrete.

The transport of Fe^{2+} away from the rebar must thus be considered for the evolution of the corrosion rate and the formation of corrosion-induced cracks. It depends on (i) Fe^{2+} content and (ii) concrete porosity. Indeed, precipitation will occur only after Fe^{2+} saturation in the solution is reached. If the corrosion rate is slow, which is the case of natural corrosion in carbonated concrete, no saturation of Fe^{2+} ions is expected close to the steel surface, resulting in their diffusion away from the interface [132]. According to Nernst equation, increasing Fe^{2+} content in the vicinity of the rebar increases the anodic reversible potential, resulting in a decrease of the corrosion rate. Hence, an increase in total porosity of concrete will facilitate the diffusion of Fe^{2+} away from the rebar, resulting in a decrease of the anodic reversible potential and in the increase of the effective corrosion current density [125].

Nonetheless, a maximum effective current density is expected beyond a certain opening of the pore structure, from which the system tends to behave as a bulk solution in terms of transport properties (no more transport limitation due to concrete porosity) [125]. The diffusion of Fe^{2+} away from the rebar competes with the diffusion of O_2 in the opposite direction. Hence, the diffusion of Fe^{2+} can be very limited, depending on the pH, as it is oxidized in Fe^{3+} and precipitates rapidly as Fe(III)-bearing species, Fe^{3+} being much less soluble than Fe^{2+}. We must note that even if a thick corrosion layer develops at the vicinity of the rebar, a “virtual” diffusion of Fe^{2+} can still occur across this layer through electron transfer in the Fe(III) layer, i.e. sorption of one Fe^{2+} on one side and release of another Fe^{2+} on the other side, as proposed for Fe diffusion at the steel-bentonite interface [235].

3.4.2. Nature and distribution of CPs in chloride-induced corrosion

For chloride-induced corrosion, several intermediates can be formed, such as ferrous hydroxychloride or chloride green rust $GR(Cl^-)$, which is thermodynamically stable in the alkaline pore solution and can be observed near the rebar [215,236]. A large variance in the final CPs is reported in the literature, the products being a mixture of magnetite, goethite, lepidocrocite and/or ferrihydrite [237–239]. In addition, in the presence of a large excess of chloride, ferrous hydroxychloride β-$Fe_2(OH)_3Cl$ is suspected to be formed as an intermediate product before its oxidation in GR(Cl^-), which can be later oxidized into akaganeite with an increased chloride content [240,241]. Currently, there is no physical explanation for this variance, probably because the mechanism of steel depassivation is still not fully understood [92].

In addition to the local acidic conditions induced in the pit, the presence of chloride increases the solubility of Fe^{2+} ions, which prevents their rapid precipitation and allows their diffusion and migration away from the pit [218]. CPs accumulate first between the steel and the mill scale and then penetrate adjacent porous zones [242]. This penetration strongly depends upon the distribution of the hydration products and the concrete porosity around the rebar. As they diffuse away from the pit, ferrous chloride ions are no longer stable due to the higher pH of the pore solution and rapidly precipitate, filling the pores ('corrosion-filled paste') [243] and impeding further diffusion of Fe^{2+}. As corrosion continues, new CPs tend to precipitate near the surface of the rebar, which finally results in the formation of corrosion-induced cracks [244]. Hence, major localized loss of steel cross-section may occur before the appearance of cracks on concrete surface in the case of chloride-induced corrosion.

3.4.3. Impact on the structural performance of RC structures

The formation of solid-state CPs plays a major role in the structural performance and service life of RC structures [92]. Even if it can be up to 6.5, as shown in Table 2, the expansion coefficient of the mixture of CPs in concrete generally varies between 2 and 4 [245–247]. This volume expansion will exert a radial pressure on concrete, generating corrosion-induced cracks if CPs grow under confined conditions [239,248,249]. The cracking process can be split into three stages: corrosion products filling, concrete cover stress and concrete cover cracking [250]. If the first stage progressively modifies the porosity and can help in preventing corrosion if pore clogging occurs, the two other stages result in accelerated corrosion as they create preferential paths for the ingress of aggressive agents. The time-to-cracking of the concrete related to steel corrosion is thus largely dependent upon its porosity.

Moreover, environmental parameters such as temperature can accentuate the cracking process. Indeed, the morphology of the oxide layer can change with temperature [251], and partially reversible redox reactions have been observed during temperature cycling between 5 and 45 °C [252]. The valence state of the shell and the hydroxide content (i.e. oxidation and hydration: transformation of magnetite into goethite or lepidocrocite) is positively correlated with temperature increase, leading to an augmentation in the corrosion potential of the rebar [253]. Thus, the corrosion potential is more linked to redox activity of the oxide layer than to oxygen availability, as the concentration of oxygen decreases with a temperature increase [252]. The opposite trend is observed when temperature decreases (i.e. dehydration and reduction), resulting in a "breathing" of the shell with temperature cycling that can affect the stability of the passive film [253].

The development of CPs and the possible formation of corrosion-induced cracks can be monitored with scanning electron microscopy (SEM), energy dispersive X-ray spectrometry (EDS), X-ray diffraction (XRD), Raman spectroscopy and X-ray µCT (Fig. 7) [128,254–258]. Four different parts can be observed in the material: the steel, the dense product layer, the transformed medium and the binder [259,260]. The mill scale can also be sometimes differentiated [261,262]. As the rust distribution is generally non-uniform on the steel surface [263], several models have been developed for predicting corrosion-induced concrete cracking [264–266]. Though the models adequately predict the time-to-cracking for the experiments for which they were calibrated, their predictions may not be as accurate for fitting the results obtained in other studies with different experimental conditions [267]. Hence, the development of a general model for corrosion cracking is still required.

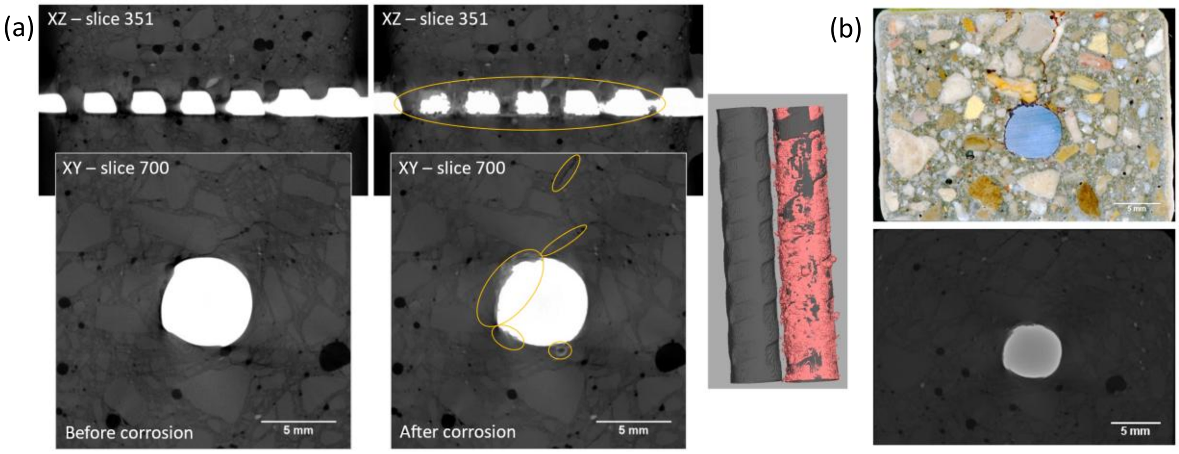

Figure 7. (a) X-ray µCT 2D slices acquired on a mortar sample like the one of Fig. 1, comparing the same sample before and after corrosion. The 2D slices are extracted from the 3D volume at the same position to visualize the development of corrosion products. The rebar is shown before and after corrosion by thresholding the corrosion products (in pink). X-ray µCT images show that the corrosion products fill the porosity (air voids) and generate cracks on the mortar around the rebar up to its surface (surrounded in yellow). (b) Comparison of surfaces by optical and X-ray µCT acquisition. After accelerated corrosion, the sample was cut to observe the distribution of corrosion products in the sample. Though X-ray µCT is a great technique to determine the distribution of phase and porosity of the material, some corrosion products are hardly detected. Courtesy: S. Gaboreau.

4. Electrical methods for non-destructive testing and evaluation of corrosion

Non-destructive testing and evaluation (NDT) of the corrosion of steel in concrete is a major issue for predicting the service life of reinforced concrete structures [18]. Among the different techniques, electrical methods allow evaluating the corrosion rate, a parameter of prime importance for estimating the service life of RC structures in the propagation stage. These methods require the use of an electrical system with two-, three- or four-electrode configurations to determine three main parameters: corrosion potential E_{corr}, concrete resistivity ρ and polarization resistance R_p [268]. Table 3 summarizes the different techniques presented in detail in this section, with their methodology and main advantages and drawbacks.

Table 3. List of electrical methods for the assessment of the corrosion rate of steel in concrete, with their main advantages and drawbacks.

Method	**Methodology**	**Advantages and drawbacks**
Corrosion potential/ Half-cell potential	Measurement of the open-circuit potential difference between the rebar and a reference electrode placed on the concrete surface or embedded in the concrete	✓ Fast measurement ✓ Allow the identification of the main defect points with high corrosion risk × No quantitative information of the corrosion rate × Absolute value is highly affected by concrete conditions (geometry, resistivity, presence of cracks), composition of the pore solution (pH, chloride or sulphide content), the condition of the steel rebar (cathode-to-anode ratio), the availability of oxygen near the steel surface and environmental factors (RH, T) ➔ Results must be interpreted only as potential gradients × Electrical connection to the rebar is required ➔ Measurements can be performed using at least two reference electrodes placed on concrete surface and the results must be interpreted as potential vectors [269–271]
Concrete resistivity (Wenner configuration)	Injection of a direct or alternating current between the two outer electrodes and measurement of the resulting potential difference between the two inner electrodes Usual parameter: • $0.01 < f$ (kHz) < 10	✓ Fast measurement ✓ Provide insights on concrete durability ✓ Allow the identification of the main defect points with high corrosion risk ✓ Corrosion rate can be estimated based on recommendations and correlations with concrete resistivity × No unique correlation could be determined between the two parameters × Absolute value is highly affected by concrete conditions (geometry, resistivity, presence of cracks), composition of the pore solution, environmental factors (RH, T), and the presence of the rebar ➔ Electrical resistivity tomography (ERT) must be performed to consider accurately the inherent heterogeneity of concrete and to account for the rebar effect in the measurement
Linear polarization resistance (LPR)	Linear sweep voltammetry in the anodic or cathodic direction around the corrosion	✓ Fast measurement ✓ Good agreement with gravimetric loss in case of active corrosion

	potential Usual parameters: • Sweep rate = 10 mV min^{-1} • E_{corr} ±10-20 mV	✖ Electrical connection to the rebar is required ✖ Use of the Stern-Geary relation to convert R_p in corrosion current ✖ Concrete resistivity must be determined using another technique to compensate the ohmic drop ✖ Determining the polarized area on RC structures is challenging ✖ The corrosion rate in the case of passive corrosion is overestimated ➔ Slower sweep rate (<2.5 mV min^{-1}) must be used to improve the measurement of corrosion rate in this case
Tafel scan	Methodology similar to LPR Usual parameters: • Sweep rate = 10 mV min^{-1} • E_{corr} ±150-250 mV	✓ Provide directly the corrosion current instead of R_p ✖ Electrical connection to the rebar is required ✖ Can cause irreversible changes to the rebar due to the strong polarization ✖ Determining the polarized area on RC structures is challenging
Galvanostatic pulse (GP)	Injection of a direct current between the rebar and a counter electrode during, and measurement of the resulting potential difference between the rebar and a reference electrode Usual parameters: • I = 5-500 µA (ΔE < 20 mV) • t = 5-30 s	✓ Fast measurement in general ✓ Good agreement with gravimetric loss in case of active corrosion ✖ Electrical connection to the rebar is required ✖ Use of the Stern-Geary relation to convert R_p in corrosion current ✖ Determining the polarized area on RC structures is challenging ✖ The corrosion rate in the case of passive corrosion is overestimated ➔ Longer measurement time (>100 s) must be used to improve the measurement of corrosion rate in this case
Electrochemical impedance spectroscopy (EIS)	Injection of an alternating potential between the rebar and a counter electrode during, and measurement of the resulting current between the rebar and a reference electrode Usual parameters: • E = 10 mV RMS • $10^{-3} < f\,(\text{Hz}) < 10^{5}$	✓ Good agreement with gravimetric loss in case of active and passive corrosion ✓ Provide insights on the corrosion mechanism ✖ Electrical connection to the rebar is required ✖ Selection of the electrical equivalent circuit is of prime importance to determine accurately R_p ✖ Use of the Stern-Geary relation to convert R_p in corrosion current ✖ Measurement time is long ➔ Possibility to limit the use of low frequencies but the accuracy of the R_p

		value obtained in this case may be less accurate, irrespective of the selected EEC ➔ Alternatively, harmonic analysis of the signal obtained at only one low frequency in the time-domain can be done to obtain the corrosion current ✗ Determining the polarized area on RC structures is challenging
Indirect GP	Methodology similar to GP, but using a four-electrode configuration placed on the concrete surface, where two probes are used to inject the direct current and two probes are used to measure the resulting potential difference	✓ Fast measurement in general ✓ Good agreement with gravimetric loss in case of active corrosion and passive corrosion for highly resistive concrete ✓ No electrical connection to the rebar is required ✓ 'Self-confinement' of the current to determine the polarized area ✗ Simulations are required to determine the current distribution in the material ✗ Studies are still required to quantify accurately the corrosion rate
Indirect EIS	Methodology similar to EIS, but using a four-electrode configuration placed on the concrete surface, where two probes are used to inject the alternating current and two probes are used to measure the resulting potential difference	✓ Method sensitive to non-uniform corrosion that can separate the contribution of actively corroding areas and passive areas ✓ No electrical connection to the rebar is required ✗ Measurement time is long ✗ Studies are still required to provide quantitative information on the corrosion rate

4.1. Corrosion potential

Corrosion potential E_{corr}, also referred to as half-cell potential, is the open circuit potential (OCP) of the rebar.

4.1.1. Measurement

The measurement is done with a two-electrode configuration, connecting the rebar—the first half of the cell—and a reference electrode (RE)—the other half of the cell—through a high-impedance voltmeter (Fig. 8) [272]. The method was first referenced as the ASTM C876 standard test method for half-cell potentials of uncoated reinforcing steel in concrete. A local breakout of the concrete cover is generally required to create a sound contact as the rebar is not readily accessible [273]. The reference electrode is a silver-chloride electrode, a copper-sulphate electrode (CSE), or a saturated-calomel electrode (SCE), which are mostly commercialized as liquid- or gel-filled electrodes. This kind of RE is placed on the concrete surface, requiring a good electrolytic contact with the concrete. This is generally ensured using a sponge wetted with an appropriate solution with a similar pH than that of the pore solution to reduce as much as possible junction potentials [274]. As the position of the electrode and the type of electrolytic contact both affect the OCP measurements, this information must be reported in all studies.

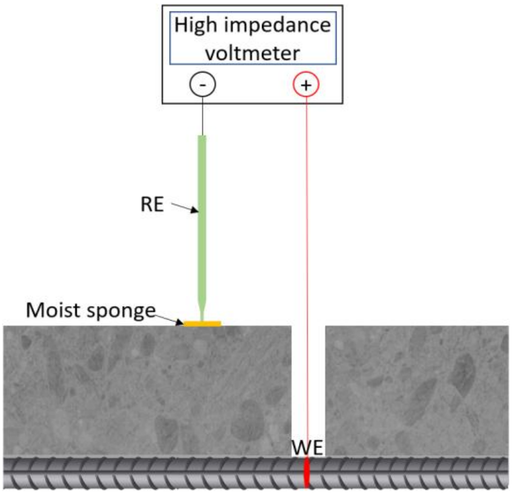

Figure 8. Schematic diagram of the measuring system of corrosion potential using a surface reference electrode.

Alternatively, concrete-embeddable solid-state metal/metal oxide reference electrodes such as manganese oxide MnO_2, activated-carbon and graphite electrodes or pseudo-reference electrodes with graphene-cement composites have shown a good stability in concrete for several months or years [275–278]. Silver-based screen-printed electrodes provide another cost-effective sensing system [279]. This is particularly interesting for new structures as the electrodes can directly be embedded during their construction, and for existing structures after maintenance actions [280]. As the pore solution ensures the electrolytic contact with embeddable electrodes, the contact resistance is less problematic and the liquid junction potential is expected to be more constant over time, which can then improve the quality of the data. However, the system is less flexible as the electrodes are fixed.

As the inspection of RC structures can be challenging, recent advances have indicated the feasibility of using climbing robots/flying drones for the monitoring of the corrosion potential [281]. The advantages of this approach are to guarantee the operator safety, especially in locations hardly accessible, and potentially to decrease the global cost of inspection.

4.1.2. Interpretation of results and recommendations

As corrosion is non-uniform along the rebar, differences in electrochemical and streaming potential values are expected between actively corroding and passive areas. The distribution of the equipotential lines in the material will be affected by the electric current flowing between these areas. Hence, the use of the half-cell potential technique requires the definition of a grid of measurements on the structure. The measured values can widely range in the water stability domain. Irrespective of the reference electrode used, they should be reported *versus* the standard hydrogen electrode (SHE) at the measurement temperature. The results can be presented as table, map or in statistical representations, depending on the size of the element and the number of data acquired [282].

The first version of the ASTM C876 standard recommended to interpret the corrosion potential based on the absolute values for evaluating the probability of corrosion in the measured area [283]. For values over -200 mV/CSE (≈116 mV/SHE), the probability of steel corrosion activity is less than 10%. For values below -350 mV/CSE (≈-34 mV/SHE), the probability of steel corrosion activity is over 90%; in between the probability of such activity remains uncertain.

For a better insight into areas with a high corrosion risk, the RILEM recommendations (2003) [282] and the revised ASTM C876 standard (2009) [283] advise the use of potential gradients rather than absolute potential values. The proposed methodology consists of mapping the potential of the entire area of inspection and comparing the relative potential values. This requires the definition of an accurate grid of measurements points, as a decrease in grid space increases the probability of finding the precise location of actively corroding spots [284]. If the grid size remains regular during measurements, it is also possible to use statistical representations, e.g. histograms, frequency distribution or cumulative probability plot, in order to compare more globally different parts of the structure [282]. Also, even if there is no electrical continuity along the rebar, meaningful information about macrocell corrosion can still be obtained using potential gradients [285].

4.1.3. Relation to corrosion rate

Many studies have tried to relate the corrosion potential to the corrosion rate, but no quantitative correlation has been found. When measurements are made in highly controlled conditions (RH, T), a robust correlation exists between the two parameters for small specimens, especially for the high corrosion probability range [286]. However, in field investigation, the environmental factors cannot be so controlled. In addition, measurements are influenced by several other factors, e.g. concrete conditions (geometry, resistivity, cover depth, presence of cracks), the composition of the pore solution (pH, chloride or sulphide content), the condition of the steel rebar (cathode-to-anode ratio), and the availability of oxygen near the steel surface [168,272,284,287,288]. For example, very negative potential values can simply be the results of a low level of oxygen. Hence, it is strongly recommended to perform measurements at once in short time, as much as possible, in order to limit any variation of these influencing factors. Despite being one of the most used technique for corrosion monitoring in field, the half-cell potential technique must be used only as a qualitative test for locating areas with a high corrosion risk on RC structures.

4.2. Concrete resistivity

Concrete resistivity (ρ, expressed in Ω m)—also referred to as electrical resistivity—is the ability of the material to oppose electrical circulation [289]. The initial resistivity of concrete is generally between 10 and 10^6 Ω m [290,291]. This value is mainly influenced by the w/c ratio, the type of binder, the size of the aggregates and the conditions of curing and storage, as they affect pore solution composition and concrete porosity [291,292]. Both parameters are important as they govern the corrosion process. Due to concrete degradation by the ingress of aggressive agents or the formation of corrosion-induced cracks, the resistivity is expected to change during the entire service life of RC structures. It is thus necessary to monitor concrete resistivity over time to assess the evolution of corrosion process.

4.2.1. Measurement

The resistivity is directly linked to the concrete resistance R_Ω (Ω) with the following equation (Eq. 2):

$$\rho = kR_\Omega = k\frac{\Delta V}{I} \qquad \text{(Eq. 2)}$$

where ΔV is the potential difference (V), I is the injected current (A), and k is a geometric factor (m) that depends on the geometry and size of the sample, but also on the experimental device. Indeed, different procedures exist for measuring concrete resistivity [291]. In the bulk resistivity cell (uniaxial configuration, Fig. 9a), two parallel metal plates with moist sponges or a conductive gel, placed at the ends of the concrete sample, apply a current and the resulting potential difference on the two plates is measured [293]. In this case, the geometric factor k is (Eq. 3):

$$k = \frac{A}{L} \qquad \text{(Eq. 3)}$$

where A is the cross-sectional area perpendicular to the current (m²) and L is the sample length (m). Even if the measurement of resistivity is rapid, this technique is used in laboratory experiments but hardly applicable to field work. The resistivity can also be measured using a four-electrode device (generally equipped with stainless-steel probes) on the concrete surface, in which two electrodes C_1 and C_2 inject a current and two electrodes P_1 and P_2 measure the resulting potential difference. Two systems are commonly used, the linear four-point probe and the square-array four-point probe, but other configurations, for example with embedded probes, exist as well [294]. In Wenner configuration (Fig. 9b), where C_1 and C_2 are the two external electrodes and P_1 and P_2 are the two internal electrodes with a similar probe spacing a (m), the geometric factor is (Eq. 4):

$$k = \frac{2\pi}{\frac{1}{a} - \frac{1}{2a} - \frac{1}{2a} + \frac{1}{a}} = 2\pi a \qquad \text{(Eq. 4)}$$

It is important to note that the use this relation assumed that the concrete is homogeneous and isotropic with a semi-infinite geometry, which is not the case for small concrete samples. To correct boundary effect and determine accurate geometric factors, it is possible to perform numerical simulations to determine a correcting factor for Eq. 4 [295] or to calibrate the device using an electrolyte of known resistivities in a core holder of similar geometry than the concrete sample.

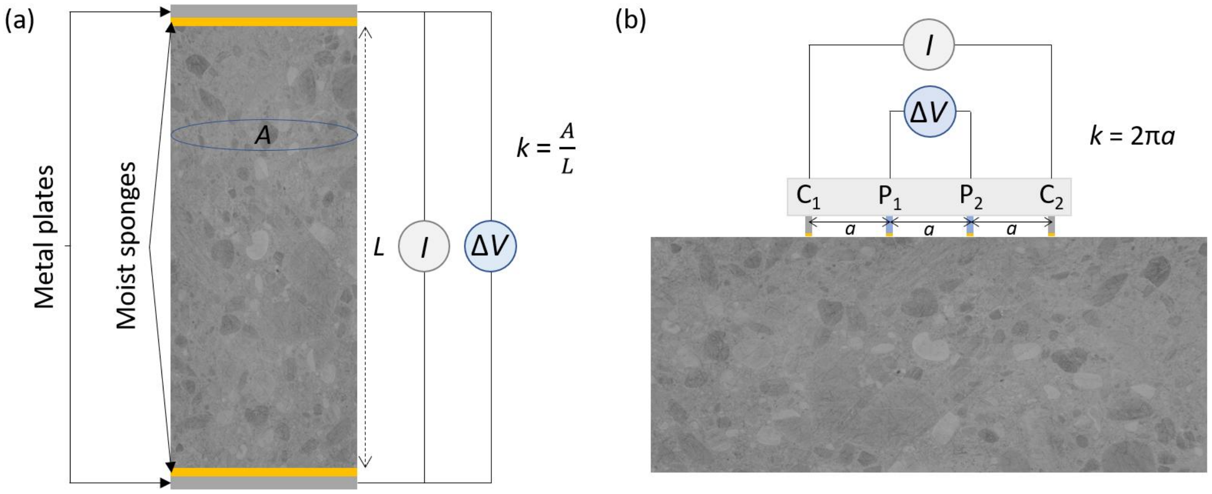

Figure 9. Schematic representation of the resistivity measurement. (a) Bulk resistivity, (b) Surface resistivity in the Wenner configuration (typically, *a* = 5 cm).

The material and size of the electrodes and the way the electrolytic contact with the concrete surface is made can also affect the measurements, as can the measuring frequency. If the concrete resistivity can be measured either in DC or in AC mode, measurements are generally made in AC mode to avoid electrodes polarization [290,296]. Generally, measurements are carried out in the frequency range of 0.5 to 10 kHz in the bulk configuration, and in the range of 0.01 to 10 kHz in the Wenner configuration [297]. Impedance spectroscopy must be done to determine the frequency at which the imaginary part of the impedance (reactance) is minimum to correctly assess the concrete resistance. This frequency must be defined case by case as it varies with concrete microstructure and moisture conditions.

4.2.2. Relation to concrete durability

From the concrete resistivity, one can determine the formation resistivity factor F_R, that represents the microstructural aspect of the concrete [294], according to the modified parallel law (Eq. 5):

$$F_{\mathrm{R}} = \frac{1}{\varphi_{\mathrm{R}}\beta_{\mathrm{R}}} = \frac{\rho}{\rho_0} \qquad \text{(Eq. 5)}$$

where φ_R is the porosity of the system and β_{R} is the connectivity of the pore system, ρ is the resistivity of the bulk sample, and ρ_0 is the resistivity of the pore solution [298]. The formation factor is also defined as the ratio of the resistivity of the bulk sample and the resistivity of the pore solution [299]. It can thus be used for determining the capillary porosity and pore tortuosity of fresh and hardened concrete [300,301]. This factor is also related to the diffusion coefficient through the Nernst-Einstein relationship (Eq. 6) [302,303]:

$$F_{\mathrm{R}} = \frac{D_0}{D} \qquad \text{(Eq. 6)}$$

where D_0 is the self-diffusion coefficient of the ionic species in water (e.g. D_0=2.032 10^{-9} m² s^{-1} for Cl^-) and D is the effective diffusion coefficient (m² s^{-1}). After determining the resistivity of the pore solution experimentally or theoretically [304–306], the diffusion coefficient of chloride in concrete can be determined in order to estimate the time to corrosion initiation by using Fick's second law of diffusion [294,307]. It is also possible to combine the formation factor with Langmuir or Freundlich adsorption isotherm, and to predict either chloride ingress with the Nernst-Planck equation [308,309] or the apparent chloride diffusion coefficient in concrete [310]. The use of concrete resistivity therefore is a good indicator of the concrete durability in terms of ion diffusivity and fluid transport [311–313].

The measurement of concrete resistivity is influenced by several parameters that can adversely affect the determination of the formation factor. The main such factors are water content and temperature; an increase in one of these two increases the ionic transport in the pore solution and decreases the resistivity of the concrete [291,314–316]. The effect of temperature is even more complicated as it also affects the solubility of the hydrated phases in concrete, resulting in a change in pore solution composition [317]. Normalization of the temperature effect on concrete resistivity has been used for predicting the resistivity variation due to temperature changes [318]. As the concrete surface interacts directly with the surrounding atmosphere, the exposure conditions must be correctly defined as they will impact the concrete resistivity and create a resistivity gradient. As discussed in Section 3.2.1, concrete carbonation results in a progressive change of the concrete microstructure, also creating a resistivity gradient in the concrete [319].

When using a four-electrode configuration, other parameters must be considered when performing the measurement as some assumptions are made to interpret the data, i.e. concrete is homogeneous and isotropic with a semi-infinite geometry [320]. The size and geometry of the specimen must then be considered accurately for determining the geometrical factor *k* as the assumption of a semi-infinite medium cannot be respected for small samples [314,321]. In addition, the presence of cracks and the distribution of aggregates in the concrete are inconsistent with a homogeneous and isotropic material [291]; regardless of the type of cracks, the measurements will be under- or over-estimated if they are made nearby [322]. Finally, the presence of rebar affects the measurement of resistivity as a distortion of the current field or a short-circuit are likely to occur (known as rebar effect) [291,323,324], decreasing the part of the current flowing only in the concrete. Several studies have shown that the rebar diameter and spacing, the concrete cover depth, the direction of the probe, the probe spacing and the distance from the rebar all affect the measurements [295,324–332]. Hence, the recommendation suggests measuring the concrete resistivity as far as possible from the reinforcement to obtain the most accurate value [290,296]. If measurements are performed close to the rebar mesh, the most suitable configuration to determine the resistivity has the probe located parallel to and midway between the top rebars [329]. If measurements are done in front of a rebar, a rebar factor can be defined and applied in Eq. 4 for correcting the resistivity for the rebar effect [295,333].

4.2.3. Relation to corrosion rate

Many studies have tried to correlate concrete resistivity with corrosion rate of steel, as the rate-determining step of corrosion can be related to the ionic transport between anode and cathode which is dependent on concrete resistance [334]. It is generally assumed that the corrosion rate is inversely proportional to concrete resistivity, especially when corrosion is in active state [334–339]. According to RILEM recommendation, the risk of corrosion is high when concrete resistivity is lower than 100 Ω m and negligible when it is higher than 1000 Ω m for OPC concrete [290,296]. However, it is not specified whether these values consider the rebar effect while it highly decreases the measured apparent resistivity. Even if a wide scatter exists [105], accurate correlations between the two parameters have been proposed [340,341] and empirical correlations have also been successfully determined for the monitoring of real structures (e.g. [342]). However, this apparent relationship does not mean that the resistance of concrete dominates the overall resistance of the process. In fact, it can be attributed to the degree of pore water saturation as both parameters are influenced by the water content. Indeed, increasing the water content lowers concrete resistivity and increases corrosion rate, and vice versa [170].

If the RILEM recommendation is still commonly used, the range of resistivity values for assessing corrosion activity varies with the studies. For example, the limit of resistivity values indicating high corrosion intensity varies between 50 and 200 Ω m, while the limit of resistivity values indicating low corrosion intensity varies between 85 and 2000 Ω m [334]. This discrepancy can notably be related to the influence of the type of binder on the absolute value of resistivity [334]. It has been shown that a rebar can corrode at relative similar rates when embedded in a low resistive mortar prepared only with Portland cement or in a high resistive mortar prepared with a mix of Portland cement and fly ash [343]. If the cement type is known, the absolute resistivity can be compared to reference value for that cement type obtained in laboratory in the relevant exposure conditions to determine more accurately the risk of corrosion [105,290]. Otherwise, it is very challenging to use these critical values in the case of existing structures with lacking information about their composition. Finally, we must remember that the specimen size has a great influence on the corrosion process [211], which can explain the scatter between laboratory and field experiments.

Hence, no general correlation between concrete resistivity and corrosion rate could be determined [337,343–345]. It has also been shown that concrete resistivity and corrosion rate evolve differently with temperature, the first following an Arrhenius-type equation [346] and the second following the Eyring law [347], which could also explain the absence of a general correlation between them. To sum up, the use of concrete resistivity can be interesting for evaluating non-destructively the risk of corrosion and estimating the range of corrosion rate when the cement type is known. It is also possible to compare the gradient in resistivity to obtain a meaningful information on the risk of corrosion, as for the half-cell potential technique. However, it cannot be used as a unique method for determining precisely the corrosion rate. It is nevertheless a parameter of prime interest that must be measured as accurately as possible for further determination of the corrosion rate, as discussed in sections 4.3.1 and 4.3.2.

4.2.4. Interest of electrical tomography

The concrete resistivity measured as presented in the above sections corresponds to an "apparent" resistivity that considers all elements in the investigated area. Therefore, this value only reflects an average value on a defined volume and does not consider the inherent heterogeneity of concrete [348]. A multi-electrode device, consisting of an assemblage of single devices with four electrodes, can be used to perform an electrical resistivity tomography (ERT) of the concrete [348,349]. With such method, it is possible to determine the resistivity at different levels/depths in order to reconstruct the spatial distribution of the resistivity in the material (Fig. 10). Results are presented as pseudo-sections showing the distribution of apparent resistivities in the material. Inversion models are then required to determine the "true" resistivities at the corresponding depth of the concrete from the measured apparent resistivities. Softwares such as Res2Dinv and Res3Dinv are commonly used for such inversion, especially in geophysics [350], but further research is required to define a standardized method for measuring and inversion modelling in reinforced cement-based materials [351]. After performing the inversion algorithm, pseudo-sections of true resistivities are obtained. As a result, the rebar effect observed on the apparent resistivities has been removed as the resistivities are now correctly distributed in the volume [352].

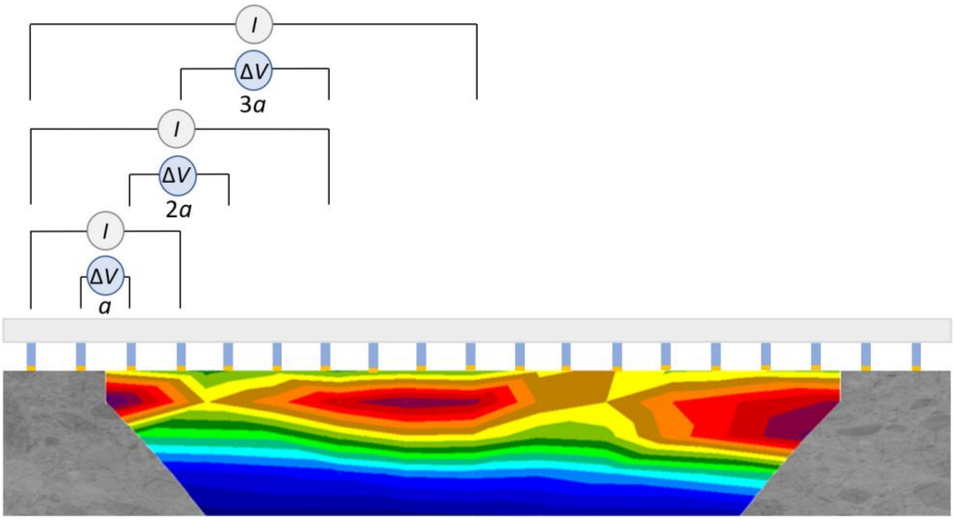

Figure 10. Schematic representation of a multi-electrode device in Wenner configuration for ERT measurements. Several probes spacing, e.g. a, 2a and 3a as shown in the figure, are required to investigate the concrete section in depth. A 2D pseudo-section of true resistivities after inversion with Res2Dinv is also provided to illustrate possible results. Courtesy: J. Gance.

One limitation when performing ERT is the variation in contact resistance between the electrodes and the concrete surface, which affects the quality of the obtained data. Systems using embeddable electrodes are being developed to ensure a good electrolytic contact during the entire measurement [353,354]. Other limitation concerns the low spatial resolution of electrical tomography [351]. It has to be noted that the probe configuration has an impact on the sensitivity of the measurement: for example, the Wenner array has a good sensitivity to vertical changes but a low sensitivity to horizontal changes [350]. Thus, using several probe configurations and spacing, complementary data may be obtained to increase the data quality and the spatial resolution. An accurate grid of electrodes is thus required for the monitoring of RC structures.

Studies have shown that ERT can be used to visualize the carbonation process, the ingress of water and chloride and all transport properties in the material over time, in both undamaged and cracked cement-based materials [351,355–358]. Indeed, for Portland-based materials, an increase in concrete resistivity can generally be attributed to the carbonation front due to pore clogging while a decrease can be attributed to the ingress of water and chlorides or the formation of cracks. However, all these phenomena are susceptible to occur simultaneously depending on the exposure environment. It is then necessary to determine first the influence of each phenomenon separately on the range of resistivity values in order to determine if it is possible to differentiate the contribution of each parameter on the resistivity profile. ERT measurements must be done over time to compare the relative evolution of resistivity pseudo-sections to determine the actual level of concrete deterioration. The results could also be used to determine the diffusion of CO_2, carbonates and chlorides in the material to better predict the length of the initiation stage. During the propagation stage, ERT measurements could give insights on the water content of the material, especially in the vicinity of the rebar, to determine if steel corrosion occurs in wet or dry conditions at the time of the measure. Despite all these opportunities, many challenges in electrical tomography remain open to its applicability in field studies [351].

4.3. Polarization resistance

Polarization resistance (R_p, expressed in Ω) is the resistance of the rebar to oxidation during the application of an external potential, i.e. during polarization of the rebar. Several electrochemical methods have been developed for determining R_p [105,338,359], using three- or four-electrode configurations. The different techniques discussed hereafter are based on the application of an external perturbation on the system to polarize the rebar. The electrochemical noise technique, which appears as a great tool for corrosion analysis because measurements are performed without any electrical perturbation, is not discussed as its applicability to RC structures is still limited.

4.3.1. Measurement in three-electrode configuration

In the three-electrode configuration, the electrochemical system consists of a working electrode (WE) —the steel rebar—, a reference electrode (RE, as described in section 4.1.1) used for measuring the rebar potential, and a counter electrode (CE, generally stainless steel, titanium or platinum) that closes the electrical circuit (Fig. 11). Providing a description of the electrode configuration is important as all three electrodes can influence the measurement [360,361]. Hence, data on the type and position of the RE, the material and the geometry of the CE, and the use of surface electrodes with a specific electrolytic contact or embedded electrodes should be provided in all studies [362].

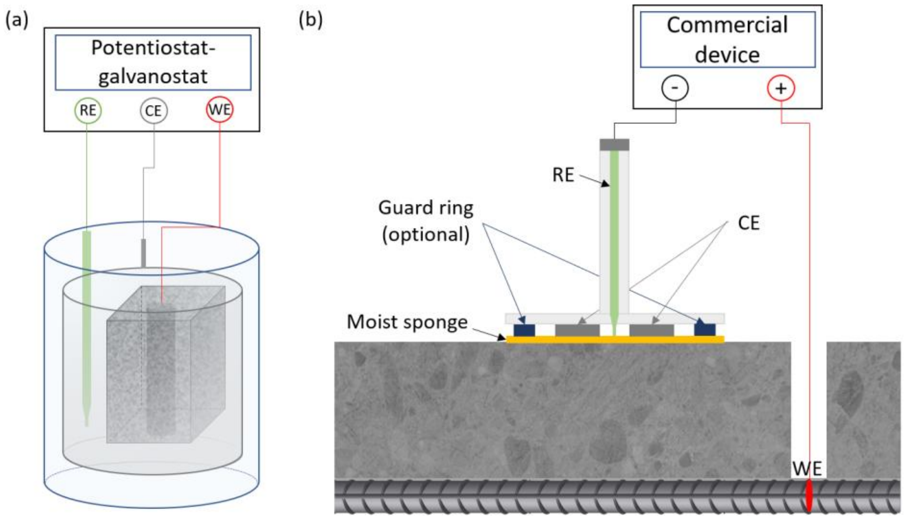

Figure 11. Schematic representation of a three-electrode configuration. (a) For laboratory experiments, measurements are generally performed on small samples in solution using a potentiostat-galvanostat; the rebar acts as the working electrode (WE), the reference electrode (RE) is generally a saturated calomel electrode (SCE) and the counter electrode (CE) is a mesh cylinder that surrounds the sample to homogenize as much as possible the current distribution in the material. Alternatively, RE and CE can be embedded in concrete. (b) In the field, measurements are generally made with a commercial device equipped with a RE in the centre and a CE (disc with inner and outer diameter), both placed on a moist sponge on the concrete

surface. Optionally, an auxiliary electrode known as the guard ring is used to supposedly confine the current to a known area of steel.

The linear polarization resistance (LPR) technique consists of applying a small potential sweep on the rebar around its open circuit potential (generally OCP±10-20 mV, either in the anodic or in the cathodic direction) and recording the resulting current (Fig. 12) [117,363]. Alternatively, the measurement can be made by applying a current sweep and recording the resulting potential [364]. Polarization resistance is given by the tangent for zero net current of the potential-current curve (Eq. 7).

$$\frac{\Delta E}{\Delta I} = R_{\mathrm{p}} \qquad \text{(Eq. 7)}$$

Please note that the slope is not directly equal to R_p, but represents the sum of polarization resistance and concrete resistance [16]. It is therefore necessary to compensate the ohmic drop R_Ω to determine IR-free values of R_p [105,365]. If another technique must be used in complement to determine R_Ω, some instrumentation directly incorporates an automatic compensation of the ohmic drop.

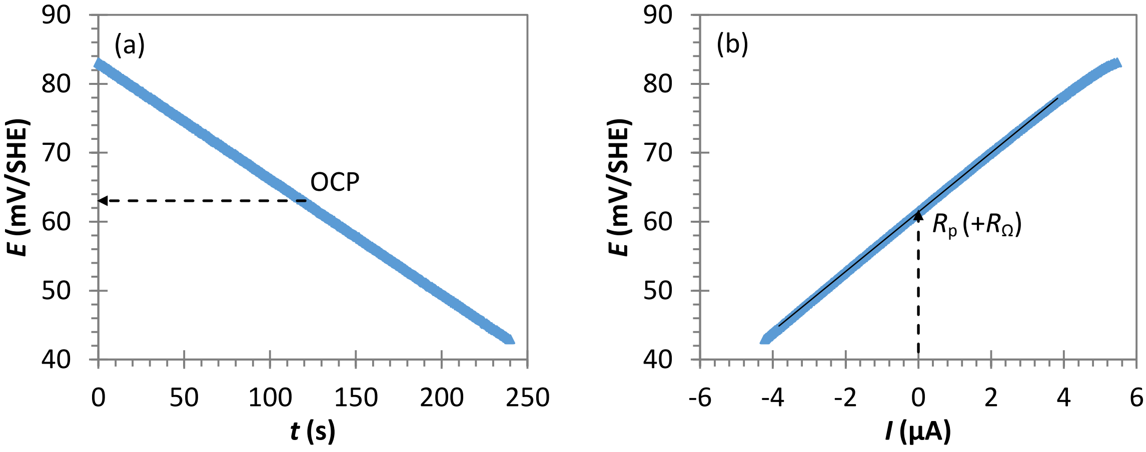

Figure 12. Example of an LPR measurement in the cathodic direction from +20 mV to -20 mV *vs.* OCP. (a) Evolution of the potential with time applying a potential sweep of 10 mV min^{-1}, (b) Evolution of the potential with a current during the potential sweep, allowing the determination of R_p.

The sweep rate is a critical parameter for accurate evaluation of the polarization resistance, as it is required that the system is stabilized at each potential during the measurement. Typically, in agreement with gravimetric mass loss (ASTM G1 standard), a reliable measurement of R_p for active corrosion (i.e. current density values over 1 µA cm^{-2}) can be obtained using a sweep rate between 2.5 and 10 mV min^{-1} in potentiodynamic mode [105], 10 mV min^{-1} being the common recommended value (ASTM G5 standard). However, in the case of passive reinforcements, the corrosion current density is overestimated by a factor of between 2 and 10 compared to the gravimetric study using this sweep rate value [366]. To obtain a closer value than that expected for passive corrosion (i.e. below 0.1 µA cm^{-2}), slower sweep rates—even less than 2.5 mV min^{-1}—should be used. In controlled conditions such as in laboratory experiments, this is not a problem as the time required for measuring generally is not a limiting factor, and LPR experiments can be systematic. However, for field investigations, as the measurement time is a critical parameter, the results obtained for passive rebar must be used with care as the polarization resistance will probably be underestimated [366,367].

The second method used for determining R_p is the pulse technique. The measurements are generally made in galvanostatic mode [368,369], but they can also be done in potentiostatic [370–372] or coulostatic mode [373,374]. In the galvanostatic mode (galvanostatic pulse, GP), a low anodic DC current (generally I_{app}=5-500 µA) is applied to the reinforcement during a short time (typically 5-30 s for active corrosion) in anodic or cathodic direction and the transient potential is recorded until stabilization [105]. Rapidly after the polarization, a strong potential increase occurs due to the ohmic resistance of the concrete; a further progressive increase until reaching a steady state occurs afterwards due to the electrical double layer effect (Fig. 13). For validating the assumption of linearity between current and potential, the potential shift should not exceed 20 mV [105]. When the current is turned off, a similar behaviour as that recorded during the charge occurs during discharge.

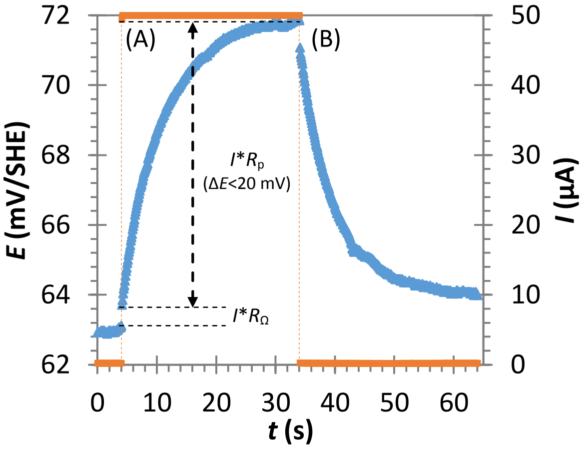

Figure 13. Example of GP measurement in the anodic direction showing the injection of 50 µA during 30 s and the evolution of ΔE with time during (A) the charge (current applied) and (B) the discharge (no current applied).

Based on the Randles circuit, which consists of the ohmic resistance R_Ω in series with a parallel combination of the double layer capacitance C_{dl} and the polarization resistance R_p, the polarization at any time t can be expressed as (Eq. 8):

$$E_t = I_{\mathrm{app}}\left[R_{\mathrm{p}} * \left[1 - \exp\left(\frac{-t}{R_{\mathrm{p}}C_{\mathrm{dl}}}\right)\right] + R_\Omega\right] \qquad \text{(Eq. 8)}$$

The expression is generally linearized for calculating R_p and C_{dl} (Eq. 9):

$$\ln(E_{\max} - E_t) = \ln(I_{\mathrm{app}} * R_{\mathrm{p}}) - \frac{t}{R_{\mathrm{p}}C_{\mathrm{dl}}} \qquad \text{(Eq. 9)}$$

where E_{max} is the steady-state potential value. A curve fit can also be used for calculating the different parameters (Eq. 10):

$$E_t(t) = K_0 - K_1 \exp\left(\frac{-t}{K_2}\right) = I_{\mathrm{app}}(R_{\mathrm{p}} + R_\Omega) - (I_{\mathrm{app}}R_{\mathrm{p}}) \exp\left(\frac{-t}{R_{\mathrm{p}}C_{\mathrm{dl}}}\right) \qquad \text{(Eq. 10)}$$

Alternatively, a modified Randles circuit using a parallel combination of a constant phase element (CPE) and a polarization resistance R_p in series with a Warburg element Z_W, can be used for modelling the steel-concrete interface [375].

The area of the rebar that is polarized during measurement must be determined for an accurate conversion of the polarization resistance in corrosion rate. An auxiliary electrode—known as the guard ring (Fig. 11b)—is often used for confining the polarization to a known surface of the rebar, generally assumed to be the area below the counter electrode [376]. When modelling galvanostatic pulse measurements with a finite-element method, it was shown that in the case of uniform corrosion, for small concrete samples with one carbon steel rebar, a decrease in concrete resistivity or an increase in cover depth result in an increased lateral dispersion of the current on the rebar, i.e. in a decrease in the part of the current under the counter electrode, both in the presence (see [377]) or absence (see Fig. 14) of a guard ring. Thus, assuming that only the area below the CE is polarized, only a fraction of the total current impressed by the counter electrode must be considered for a correct assessment of polarization resistance, this fraction depending mainly on concrete resistivity, cover depth, the geometry of the CE and the size of the sample (border effects).

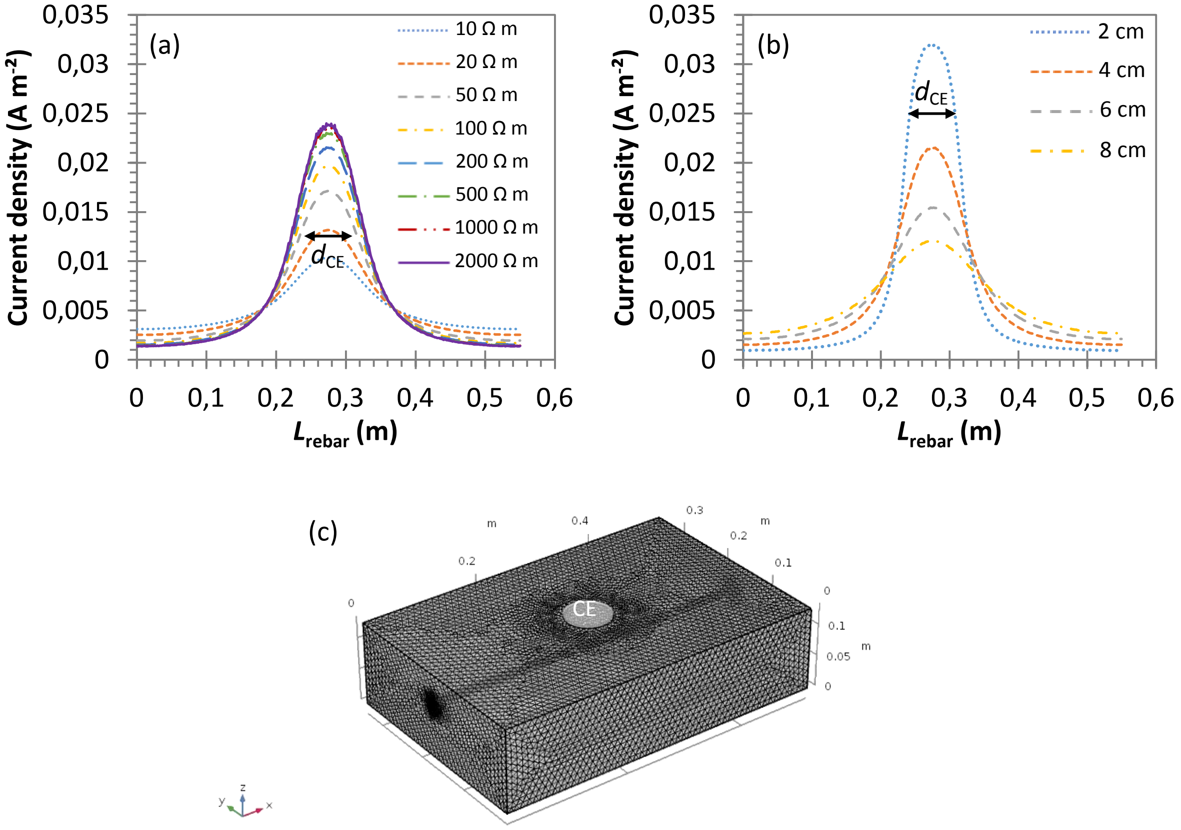

Figure 14. Effect of concrete parameters on the distribution of current density along the upper ridge (the most strongly polarized part) of the rebar using the GP technique in the case of uniform corrosion (i_0=10 µA cm^{-2}). (a) Concrete resistivity ρ (Ω m) for 4 cm cover depth, (b) Cover depth (cm) for ρ=200 Ω m. Simulations solved a secondary current distribution in a temporal study (evaluated here at 30 s) with a finite-element method using COMSOL Multiphysics 5.3a software. The dimension of the concrete domain was 55x34x13 cm^3 with one low-carbon steel pure iron rebar (Φ=12 mm, σ=5.10^6 S m^{-1}). The concrete domain acts as the electrolyte with uniform conductivity and electric isolation at the external boundaries of the material. Potential and current density distribution were solved with Ohm's law and charge conservation law in the concrete domain with

extremely fine mesh. The corrosion reaction on the steel surface was modelled as boundary condition (electrode surface) using the general Butler-Volmer equation (Eq. 1, with $\alpha_a=\alpha_c=0.5$, $E_{corr}=-0.78$ V, $T=20$ °C). (c) The counter electrode of the GP device was modelled using several geometries, here shown as a 7-cm-diameter cylinder on the concrete surface directly above the rebar centre. A current source was applied to the counter electrode at 100 µA. The positive sign in the y-axis indicates anodic polarization.

In the case of passive rebar, longer times (>100 s) are needed to reach a steady-state potential compared to active corrosion. This can be explained by the low capacity of the passive rebar to consume an anodic polarizing current, resulting in the lateral propagation of current into the rebar, especially when the latter is long [377]. Duration of the pulse is thus the most important parameter in the determination of polarization resistance as it can be significantly underestimated with short-time measurements [377,378]. Hence, as for the LPR technique, the results obtained from GP measurements in the field must be used with care in the case of passive reinforcements if the steady-state potential is not reached.

In the case of a non-uniform corrosion, where anodic and cathodic zones are spatially separated but electrically connected, the direction and magnitude of polarization will affect the current distribution on the rebar [379]. Generally, in anodic polarization mode, the anodic zones will receive more current per area than the cathodic zones, while the opposite is true in cathodic polarization mode [377,379]. Due to the different ohmic and capacitive contributions of the anodic and cathodic areas, it is important to consider the spatial and time-dependent distribution of the impressed current to correctly interpret the results obtained from GP measurements [380].

The third method to determine R_p is electrochemical impedance spectroscopy (EIS) [381,382]. This consists of applying a small-amplitude alternating potential difference (5-20 mV peak-to-peak) or current at different frequencies f and measuring the resulting current or potential, respectively. For a potential modulation (Eq. 11):

$$E(t) = |\Delta E| \cos(\omega t) \qquad \text{(Eq. 11)}$$

the current response is (Eq. 12):

$$I(t) = |\Delta I| \cos(\omega t + \varphi) \qquad \text{(Eq. 12)}$$

where ω is the angular frequency (rad, with $\omega=2\pi f$) and φ is the phase (°).

In AC condition, the property related to the opposition of a circuit to an electrical current is called impedance (Z). Each circuit element, whether resistor, capacitor or inductor, has an impedance. If the resistance created by a resistor is independent of the frequency ($Z_R=R$), the resistance created by a capacitor or an inductor depends on the frequency ($Z_C=\frac{1}{j\omega C}$ and $Z_L=j\omega L$), creating a phase shift between voltage and current. As the sinusoidal current or voltage can be represented as a rotating vector, the impedance can be divided into two components, a real component and an imaginary one (Eq. 13) [382]:

$$Z = Z_{\mathrm{re}} + jZ_{\mathrm{im}} \qquad \text{(Eq. 13)}$$

where the real component is the resistance R and the imaginary one is the reactance X (conductance or inductance). The modulus and phase of the impedance are then defined (Eqs. 14-15):

$$|Z(\omega)| = \sqrt{Z_{\mathrm{re}}(\omega)^2 + Z_{\mathrm{im}}(\omega)^2} \tag{Eq. 14}$$

$$\varphi(\omega) = \tan^{-1}\left(\frac{Z_{\mathrm{im}}(\omega)}{Z_{\mathrm{re}}(\omega)}\right) \tag{Eq. 15}$$

Different data plots are used to represent the results obtained by EIS. The Nyquist plot is obtained by plotting Z_{re} on the x-axis and $-Z_{\mathrm{im}}$ on the y-axis (Fig. 15a). The R_{p} value is determined at low frequencies where the plot intercepts the x-axis (on the right side of the plot), considering the concrete resistance that is determined at high frequencies (on the left side). The Bode plot is obtained by plotting log(f) on the x-axis and $|Z|$ or φ on the y-axis (Fig. 15b). On a Bode plot using the Z modulus, the R_{p} value is determined according to the low-frequency plateau (on the left side), by considering the concrete resistance that is determined at high frequencies (on the right side). In practice, only part of the low-frequency loop is obtained, and the plot must be extrapolated for obtaining the R_{p} value by using an equivalent electrical circuit (EEC) [375,383,384]. Selection of the EEC is crucial to accurately evaluate the corrosion process. Among the different EECs [385–387], some of the most used for simulating steel corrosion in concrete—involving several resistances and capacitors representing the properties of the electrolyte, the corrosion reaction or even the passive film—are shown on Fig. 15c. Commonly, the capacitive elements are replaced by constant-phase elements (CPE, also noted Q) to consider the non-ideal behaviour of the physical elements (leaking capacitor, $Z_{\mathrm{CPE}} = \frac{1}{Q(j\omega)^n}$) [388,389].

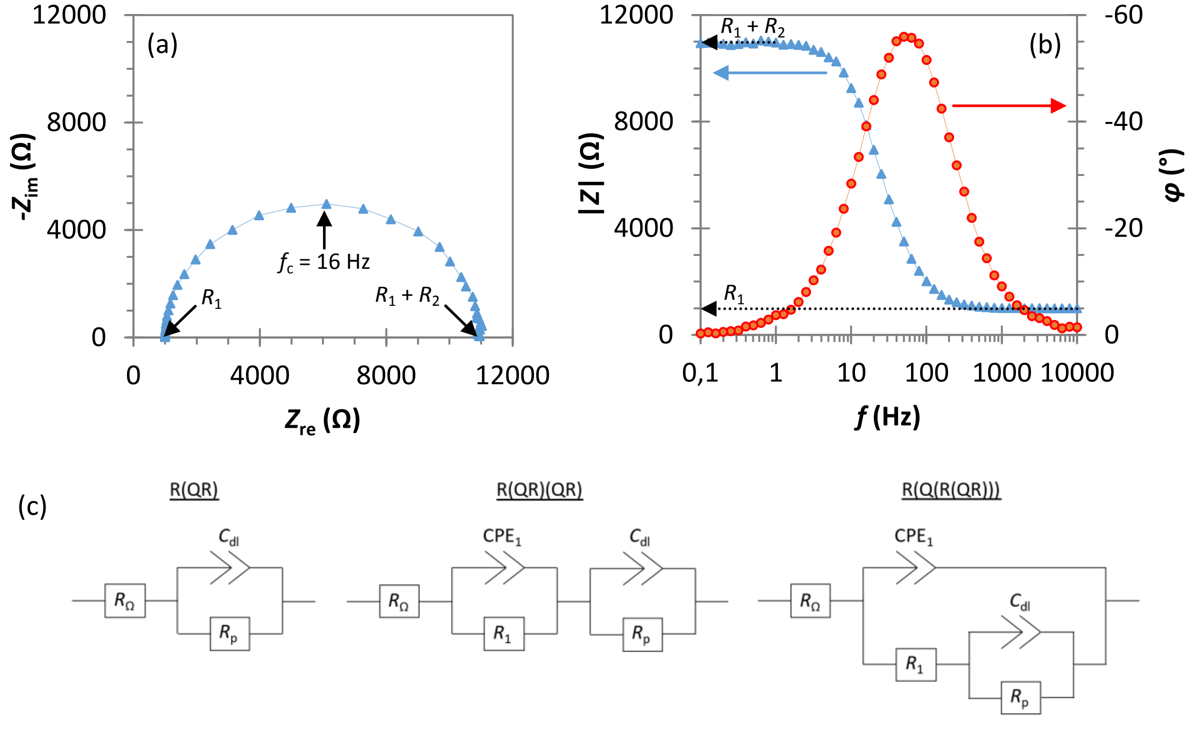

Figure 15. Example of (a) Nyquist plot and (b) Bode plot obtained at 10 mV RMS between 10^4 and 10^{-1} Hz with 10 points per decade using a dummy cell with parameters R_1=1000 Ω, R_2=10000 Ω and C=1 µF. (c) Examples of electrical equivalent circuits for fitting the experimental results in the case of steel corrosion in concrete, from left to right: R(QR), R(QR)(QR) and R(Q(R(QR))). In addition to the resistance of the electrolyte, the polarization resistance and the double layer capacitance, the additional parameters can be attributed to the passive film.

EIS is a powerful technique for mechanistic investigations as it can be used to determine several parameters, such as the bulk concrete properties at high frequencies [390–392], the mass-transfer phenomena and diffusion coefficients [393–395], or the properties of the passive film on the steel surface at low frequencies [90]. In alkaline solutions, it was shown that EIS measurements can provide insight into the mechanism of the cathodic reduction at the oxide layer of carbon steel, allowing characterization of the oxide film [396]. The proposed methodology includes the use of a power-law distribution and a complex capacitance representation of the data when using a CPE for describing the film impedance [396].

The main advantages of the two DC methods are the short time and "standard" equipment required for the measurements as compared to EIS. However, the latter generally provides a more accurate value of polarization resistance in the case of passive reinforcement [366]. If it is possible to limit the use of low frequencies to decrease to time required for analysis, the accuracy of the R_p value obtained in this case may be affected irrespective of the selected EEC. Alternatively, an analysis of the alternative current and potential in the time-domain can also be performed at only one selected frequency [397,398]. The methodology consists of a fast-Fourier transform and subsequent harmonic analysis of the time-domain signal. The advantage of the harmonic analysis is that it doesn't required any conversion of the polarization resistance as it provides directly the corrosion current density and the Tafel constants, in addition to decreasing the measurement time. A good agreement with conventional techniques is found as long as the selected frequency is lower than the characteristic frequency f_c, i.e. the frequency at which the imaginary component of the impedance reaches its maximum [398]. More studies are still required to demonstrate the applicability of this technique for the monitoring of RC structures.

Several drawbacks in the determination of the polarization resistance with this three-electrode configuration exist for field experiments. First, the area of the counter electrode must be larger than the reinforcement to avoid any perturbation during measurement [361], which is hardly feasible in real structures. It is also difficult to assess the area of steel polarized during the measurement. Though the use of a guard ring with modulation has been proposed to confine the current below the counter electrode, many studies have shown that it often fails and contributes to the polarization of the rebar, thus compromising the measurement [156,377,379,399–404]. Notably, in the case of macrocell corrosion, the polarized area can be different than the supposed confinement area if the anodic site is located far from the counter electrode [402]. During anodic polarization, the current from the counter electrode and the guard ring will preferentially polarize the active area as the current follows the path of lowest polarization resistance. During cathodic polarization, this current will spread over the passive areas, showing the incapacity of the guard ring to effectively confine the current whatever the polarization direction [405]. Finally, the main drawback of this configuration is the need of an electrical connection to the rebar, requiring breakout of local parts of the concrete to make the measurement. Alternatives have thus been proposed to tackle this issue, as discussed hereafter.

4.3.2. Measurement in four-electrode configuration

Several techniques have been proposed for estimating the polarization resistance without connection to the rebar, which can be referred to as indirect polarization, using a four-electrode array on the concrete surface [366,406–413]. The most common one is the Wenner configuration, where the four electrodes are aligned with a constant electrode spacing (as already shown in Fig. 9b). Measurements can be done by imposing a direct current [414–416] or an alternative current at several frequencies [417–421]. The DC method can be referred to as indirect GP—similar to time-domain induced polarization (TDIP) used in geophysics—while the AC method can be referred as indirect EIS—similar to spectral induced polarization (SIP) used in geophysics.

The material of the potential electrodes can be an important parameter, especially for time-domain measurements. Indeed, the potential difference between two polarizable electrodes, e.g. stainless steel, is unstable due to self-potential. This self-potential must be accurately determined for correcting both polarization resistance and double layer capacitance obtained from the transient potential induced by the current injection. Electrodes of the second kind, e.g. Ag/AgCl or $Cu/CuSO_4$, can be used as they are more stable, non-polarizable and thus have lower self-potential values than stainless steel [422]. The size and geometry of the electrodes may also influence the measurement.

In four-electrode configuration, only a fraction of the current injected on concrete surface polarizes the rebar, the rest will flow exclusively in concrete. The current distribution in the material depends on the time or frequency of measurement and the state of the rebar. For an actively corroding rebar, the distribution is very similar at high and low frequencies due to the low polarization resistance, the current penetrating the rebar perpendicularly to its surface [411]. The current distribution is symmetric about the centre of the device, one side being anodically polarized and the other being cathodically polarized [377]. By numerical simulations, it was shown that an increase in the concrete resistivity, a decrease in the cover depth and a decrease in the rebar diameter result in the increase in the total current that reach the rebar [377]. In addition, the increase in the electrode spacing of the monitoring device increases the total current that reach the rebar and the polarized area (Fig. 16).

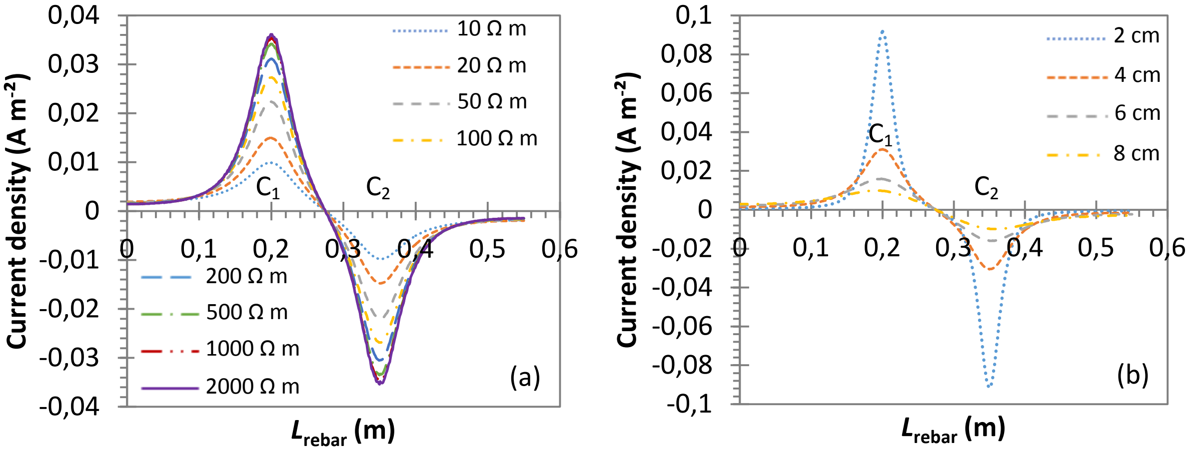

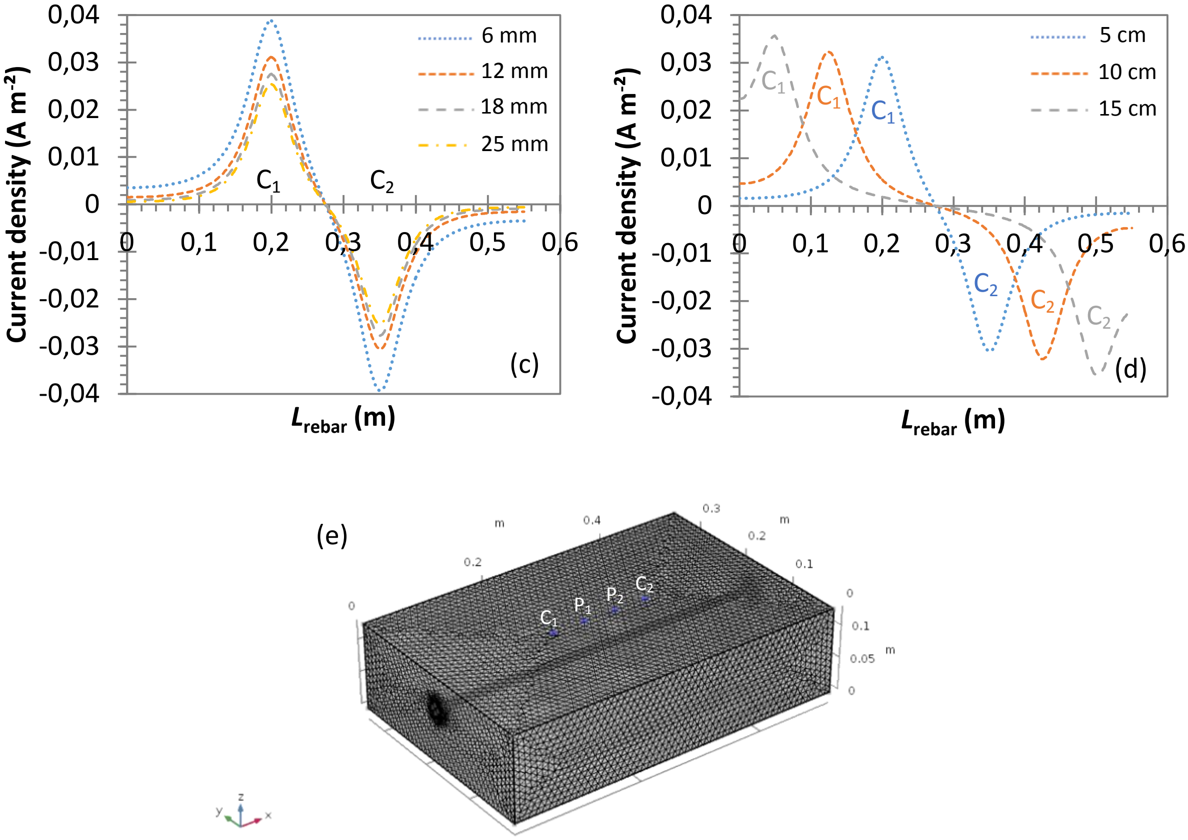

Figure 16. Effect of concrete and monitoring parameters on the distribution of the current density along the upper ridge of the rebar using the indirect galvanostatic pulse technique in case of uniform corrosion (i_0=10 µA cm^{-2}). (a) Concrete resistivity ρ (Ω m) for 4 cm cover depth, Φ=12 mm and electrode spacing a=5 cm. (b) Cover depth (cm) for ρ=200 Ω m, Φ=12 mm and a=5 cm. (c) Rebar diameter (mm) for ρ= 200 Ω m, 4 cm cover depth and a=5 cm (d) Electrode spacing a (cm) for ρ=200 Ω m, 4 cm cover depth and Φ=12 mm. Details of the simulations and input parameters are on Fig. 14. The four electrodes of the Wenner device were modelled as perfect point objects on the concrete surface (e). Point current sources impressed 100 µA in C_1 and -100 µA in C_2. The positive sign in the y-axis indicates anodic polarization.

For passive rebar, the distribution is quite different depending on the frequency. At high frequencies, the interface behaves essentially as a capacitance and the current penetrates the rebar perpendicularly to its surface as for actively corroding rebar, whereas at low frequencies the rebar acts as an insulator and only a small part of the current polarizes the rebar [411]. The current distribution is not symmetric due to the low capacity of a passive rebar to consume an anodic-polarizing current compared to a cathodic-polarizing current. Hence, errors are expected when determining the polarization resistance. However, the system tends to become symmetric with increasing resistivity, resulting in a better estimation of the polarization resistance for highly resistive concrete (>5000 Ω m) [411]. The time required for reaching the quasi-steady-state is substantially less as compared to the conventional GP method, as shown by numerical simulations [406,412] and experiments (Fig. 17).

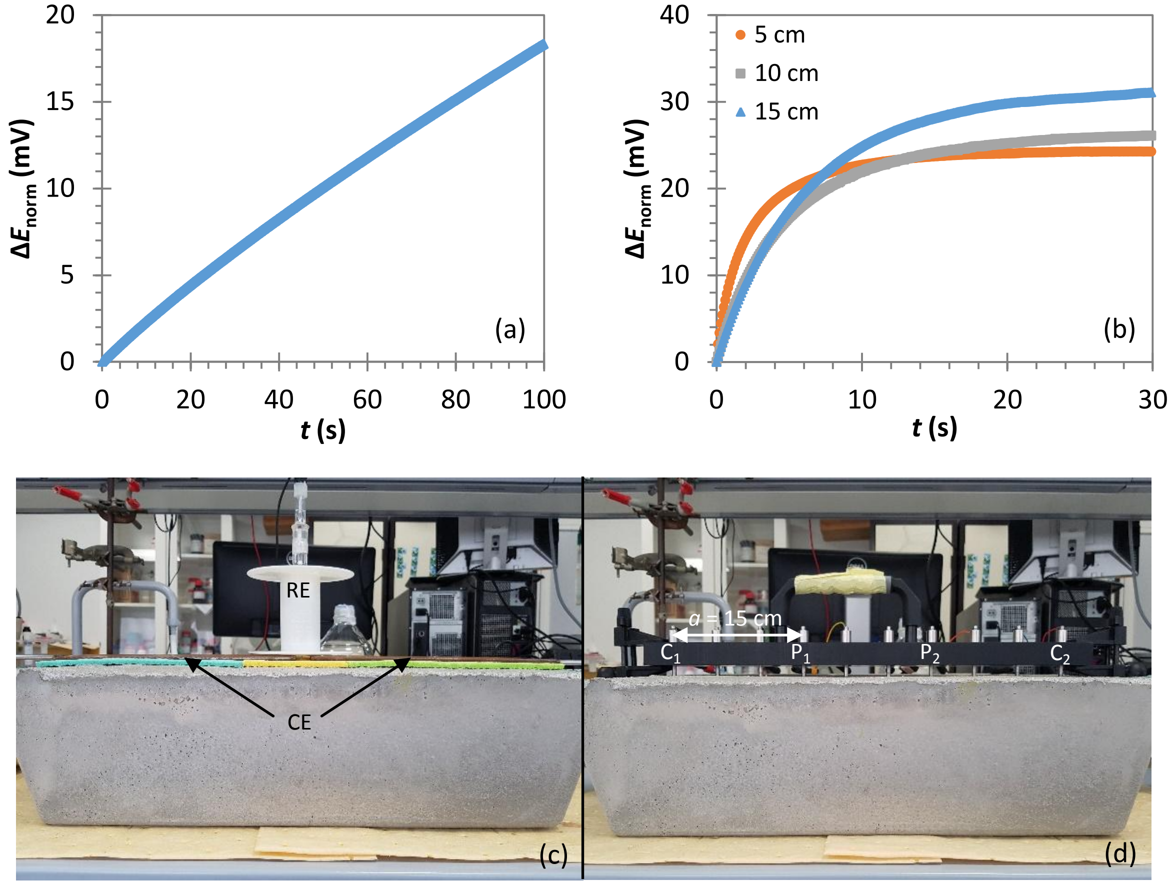

Figure 17. GP measurements using (a) three-electrode and (b) four-electrode configurations on a passive rebar. Experiments were done on a CEM I 52.5R (Lafarge) mortar sample (55x34x13 cm^3, w/c=0.4) with one ribbed carbon steel rebar (60 cm, Φ=12 mm, cover depth 3.3 cm), at constant relative humidity (dry conditions, ≈30-40% RH) and temperature (23 °C). In the three-electrode configurations (c), measurements were conducted with a mercury/mercurous sulphate reference electrode located at the centre of the sample, and a stainless-steel counter electrode (55x10 cm) placed on moist sponges on the sample surface directly above the rebar. In the four-electrode configuration (d), stainless-steel or brass electrodes (Φ_i=3 mm, Φ_e=5 mm) were used in Wenner configuration, centred directly above and parallel to the rebar. The electrolytic contact was made with moist sponges placed inside the probes. Electrode spacing a was 5, 10 or 15 cm. A potentiostat-galvanostat (PMC-2000, Princeton Applied Research) was used for galvanostatic pulse measurements. The impressed current was 10 µA between rebar and counter electrode in the three-electrode configuration, while it was 200 µA between C_1 and C_2 in the four-electrode configuration. The results indicate that a quasi-steady-state is not reached after 100 s in the three-point configuration, while it is almost reached after 30 s in the four-point configuration.

This result could be explained by the fact that the current polarizing the rebar is not constant but decreases with time before reaching a constant value, which depends notably on the exchange current density i_0 and concrete resistivity (Fig. 18). For a constant i_0, the increase in concrete resistivity results (i) in an increase in the part of the current polarizing the rebar I_{rebar}, as the current preferentially flows within the least resistive path (i.e. the rebar) and (ii) in a longer time required for reaching the quasi-steady state. For a constant resistivity, the decrease in the exchange current density i_0 results in a decrease in the total current polarizing the rebar.

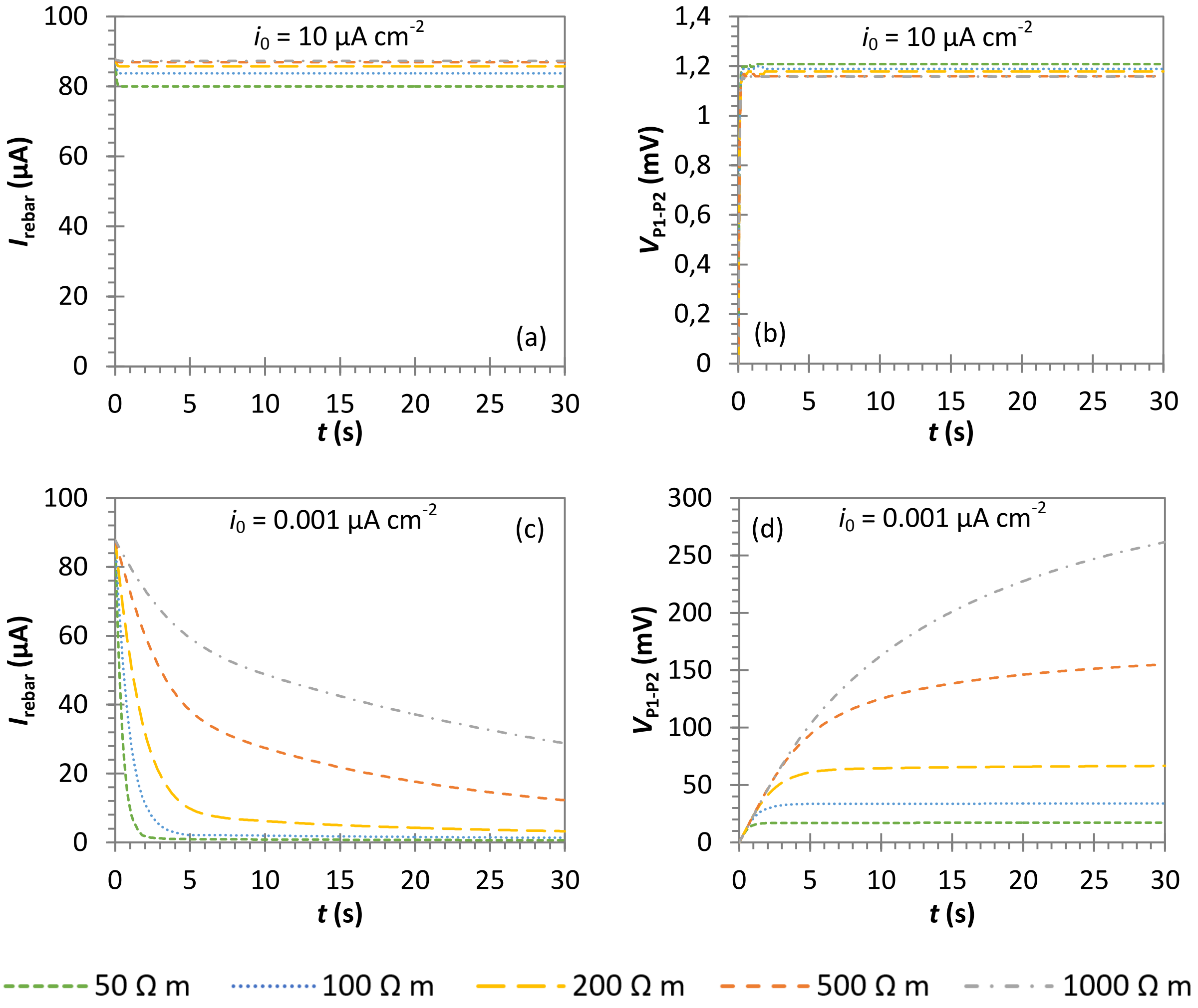

Figure 18. Effect of current exchange density i_0, considering uniform corrosion, on the current polarizing the rebar and on the potential measured between P_1 and P_2 (the ohmic drop is not shown here as the first point was normalized to 0 V), for a double layer capacitance of 0.2 F m^{-2} and for resistivities between 50 and 1000 Ω m. (a and b) i_0=10 µA cm^{-2} (active corrosion), (c and d) i_0=0.001 µA cm^{-2} (passive corrosion). Simulation details are on Figs. 14 and 16. The cover depth was fixed at 3.3 cm, like the laboratory sample presented on Fig. 17. The parameters for the Butler-Volmer equation are α_a=α_c=0.5 and E_{corr}=-0.78 V for active corrosion and α_a=0.012, α_c=0.5 and E_{corr}=0.16 V for passive corrosion.

In the case of non-uniform corrosion, it has been shown that indirect EIS method in Wenner configuration can be used to localize highly corroding areas if they are beneath to or at the vicinity of the current-injecting electrodes, as two distinct time constants can be observed instead of one time constant in uniform corrosion [421]. The authors attributed the high-frequency response to the actively corroding section and the low-frequency response to the passive areas. Otherwise, when the corroding area is located beneath the potential probes, almost no sign of active corrosion is detected. The sensitivity of this method to localize non-uniform corrosion is dependent on the length of the actively corroding area, the magnitude of the corrosion rate, and the resistivity of the cement-based material [421]. Using indirect GP method, it appears hardly possible to localize non-uniform corrosion based on a single measurement as a similar response is expected on the zero-frequency limit for both passive and localized corrosion [421]. It appears still possible to differentiate active and passive areas by performing several measurements along the rebar and comparing the results to a reference value. Reversing the polarization direction may also help to identify corroding areas.

Indeed, in GP configuration, the cathodic and anodic zones will be primarily polarized near the cathodic and anodic probes, respectively [377]. However, even close to the cathodic probe, the anodic zones will receive more current per area than the cathodic zones, the magnitude depending on the cathode-to-anode ratio and the concrete resistivity [377]. It is then expected that the resulting potential difference will be different according to the polarization direction, but this aspect must be confirmed experimentally.

Another advantage of the four-electrode configuration is the supposed self-confinement of the current in case of uniform corrosion when the rebar is long enough (>1 m), irrespective of concrete resistivity, cover depth, rebar diameter or exchange current density [411]. The sensitivity of the potential probes is different using the four-electrode compared to the three-electrode configuration. Even if a large section of the rebar is polarized, the potential probes may not be sensitive to changes that occur too far away from them. An effective polarized area which depends on the probe spacing can thus be defined [423]. If the highest sensitivity arrays are found near the potential electrodes, the measured potential difference differs depending on the probe configuration [350]. Thus, using several probe configurations and probe spacing, complementary data may be obtained to assess the different corrosion states on a single rebar [348].

Current developments of the four-electrode configuration are thus very promising, but the method is not mature and required further experimental and numerical studies. Some parameters that must be considered for its correct assessment include the contact resistance between the electrodes and the concrete surface, the non-uniformity of corrosion, and the presence of rebar mesh with different corrosion states. Also, all simulations presented previously assumed homogeneous cover depth and concrete resistivity. Gradients in concrete resistivity representative of RC structures must be applied for correct assessment of the current distribution in the material. As the sensitivity of the indirect EIS to detection of non-uniform corrosion has been demonstrated, the use of electrical tomography can be very useful to determine the distribution of the polarization resistance along large rebars and to estimate the length of the actively corroding area. Due to the similarity with concrete resistivity measurement device, the development of a multi-electrode device for characterizing both concrete resistivity and polarization resistance profiles using indirect polarization is of prime interest [424].

4.3.3. Relation to corrosion rate

Polarization resistance can be used to calculate the corrosion current I_{corr} in order to estimate the corrosion rate of steel *CR*. According to RILEM recommendation [105], the corrosion current is determined using the Stern-Geary relation (Eq. 16) [363]:

$$I_{\mathrm{corr}} = \frac{B}{R_{\mathrm{p}}} \qquad \text{(Eq. 16)}$$

where *B* is the Stern-Geary constant (V). If *B* is generally assumed to be 0.026 V for active corrosion and 0.052 V for passive corrosion of steel in concrete [425], these values do not reflect the complexity and variation with time of the corrosion process [426,427]. Accurate values of *B* should be determined empirically according to Eq. 17:

$$B = \frac{\beta_{\mathrm{a}}\beta_{\mathrm{c}}}{\ln(10) * (\beta_{\mathrm{a}} + \beta_{\mathrm{c}})} \qquad \text{(Eq. 17)}$$

where β_a and β_c are the anodic and cathodic Tafel constants (V), respectively. The Tafel constants can be determined by applying a strong polarization to the electrode (OCP±150-250 mV) and recording the current. The two coefficients are determined by plotting log(I) as a function of the overpotential η (E-E_{eq}), according to the Butler-Volmer equation (Eq. 1). Unfortunately, the Tafel slopes are often not determined on field and can be difficult to measure accurately, mainly because the anodic part of the polarization curve is not always linear [168,428–431]. Moreover, the strong polarization during the Tafel scan can cause irreversible changes to the steel rebar, which is an important drawback of this technique [432]. Hence, the use of the recommended values of 0.026 and 0.052 V can still provide an accurate estimate of the corrosion current, with generally an error of less than one order of magnitude according to the experimental values of β_a and β_c reported in the literature [162,370,431,433].

Considering uniform corrosion, Faraday's law is then often used for converting I_{corr} to CR (Eq. 18):

$$CR = \frac{I_{\mathrm{corr}} M}{nF} \qquad \text{(Eq. 18)}$$

where CR corresponds to the mass loss (g s^{-1}), I_{corr} is the corrosion current I_{corr} (A), M is the molar mass of iron (g mol^{-1}), n is the number of electrons exchanged in the reaction (n=2) and F is the Faraday constant. In terms of corrosion penetration rate (cm s^{-1}), the equation is (Eq. 19):

$$CR = \frac{I_{\mathrm{corr}} M}{nA\rho_{\mathrm{steel}} F} \qquad \text{(Eq. 19)}$$

where A is the rebar surface (cm²) and ρ_{steel} is the steel density (g cm^{-3}). For example, considering uniform corrosion of black carbon steel, a current density (I_{corr}/A) of 1 µA cm^{-2} is equivalent to a corrosion rate of 11.6 µm year^{-1} [105].

Gravimetric weight-loss tests are often done according to the ASTM G1 standard to compare the results obtained by this direct and destructive method to the results obtained indirectly from the determination of the polarization resistance. It results that LPR, GP and EIS techniques can accurately estimate the corrosion rate for actively corroding rebars in laboratory conditions, as the polarized area is known [359,366,434]. As differences in R_p values can be observed depending on the choice of the technique and its operating conditions, e.g. sweep rate, waiting time, polarization time or applied frequencies [105,378,435], it may be useful to carry out all methods to determine the most efficient one for each case, or to obtain an average value [436]. For field experiments, as the polarized area is generally not known, the accuracy of these techniques can be limited as already developed in section 4.3.1. In the four-electrode configuration, Fahim *et al.* have shown that the corrosion rate can be accurately estimated for active corrosion and even for passive corrosion in the case of a highly resistive concrete [377,411], confirming the great interest of this configuration. Further studies are still required to determine the applicability of this technique to quantify the corrosion rate on RC structures.

We must note that the Stern-Geary relationship (Eq. 16) was defined for uniform corrosion on the basis of the mixed-potential theory by Wagner and Traud, which is fundamentally not applicable for the corrosion of steel in RC structures where macrocell corrosion is expected [156,426,437,438]. For a similar reason, the use of Faraday's law for calculating the penetration rate is generally invalid, especially in the case of chloride-induced corrosion [439]. A new theoretical analysis has been proposed to calculate the corrosion rate of localized corrosion from GP measurements [380]. This approach can reduce the overestimation of the corrosion rate to a factor of maximum 2 instead a factor of 10 or more that can be obtained using the conventional Stern-Geary approach. Two elements that takes into account the different behaviour of the macrocell elements upon excitation are considered: the first is related to the fact only a fraction of the injected current flows through the anodic element and the second to the fact that this current is not constant over time during measurement. Both elements can be estimated empirically from the concrete resistivity, the cover depth and the steel surface area related to the concrete surface. As these parameters can be determined in RC structures, this approach appears feasible in engineering practice [380]. If this perspective has been proposed for the interpretation of GP measurements with the conventional three-electrode configuration, a similar approach should be done for the four-electrode configuration.

4.4. Limitation on the evaluation of corrosion rate and interest of combining NDT methods

The measurement of the polarization resistance only provides an instantaneous estimation of the corrosion rate, which is strongly dependent on the operating conditions. Hence, a single measurement cannot determine a representative annual corrosion rate if the daily and seasonal changes are not properly considered [439–441]. Considering environmental factors is essential for any accurate evaluation of the corrosion rate, in both laboratory and field studies. In real structures, the range of water content and temperature values will depend on the geographic location of the structures, and large variabilities are expected due to natural weathering through day-night and seasonal cycles, or natural wetting/drying cycles, resulting in gradients for both parameters [440,442].

However, changes in environmental conditions may not be directly observed inside concrete. Though temperature changes are rapidly reflected, even at thicknesses over 30 mm, this is not the case for RH changes for which only the surface layers are generally affected by drying processes [443–445]. Hence, temperature appears to be the primary climatic factor affecting the corrosion rate under atmospheric conditions [443]. It is important to note that the number and frequency of drying events can affect this conclusion, as the water content can become low even in depth if no wetting event occur for a long period [446]. The presence of cracks can also influence the effect of drying, which gives a greater importance of RH on the corrosion rate during corrosion propagation stage [446]. Finally, it appears that RH and T interact with each other, so they cannot be considered separately [447].

As both parameters can strongly vary, even over a single day, a measurement procedure must be defined for the accurate extrapolation of instantaneous measurements to annual corrosion rates and to incorporate the RH and T changes into service life models [448–450]. One solution is to carry out several measurements at specific times with very different conditions, at least four-times a year, to study the seasonal cycle for calculating an average value. A five-year study has shown that a power law is a good mathematical function to fit the experimental values of cumulative steel thickness loss over time for RC contaminated with chloride, exposed to both controlled and outdoor conditions [451]. This mathematical function can then be used for extrapolating the results to estimate the service life.

Under passive conditions, no strong influence of RH and T on the corrosion rate was reported [447,452]. It should thus be possible to differentiate passive and active corrosion simply by measuring the minimum and maximum corrosion rates. However, in the case of active corrosion, instantaneous corrosion rates are more affected by RH and T, with maximum values measured in moist and low resistive concrete. In addition, the corrosion rate can be orders of magnitude higher for corrosion induced by chloride (up to 1 mm year^{-1}) than by carbonation (up to 30 µm year^{-1}) in outdoor exposure [453]. Determination of the corrosion rate in extreme cases, i.e. low T and RH or high T and RH, can provide information on the expected minimum and maximum corrosion rates specific for each structure [454]. However, as the average corrosion rate can be much lower than the maximum value, this range may be too imprecise to obtain any meaningful information on the remaining service life.

Hence, it appears that determination of the corrosion rate based on measuring the polarization resistance should be complemented by other measurements. A multi-parameter approach combining electrical and other NDT methods should (i) reduce the errors resulting from measurements, and (ii) improve synergistically the estimation of service life of the reinforced concrete [5,455,456] (Fig. 19). First, a full surface inspection assesses the global state of the reinforced concrete. This includes a visual inspection of the concrete reporting any visible deterioration, e.g. surface cracks, delamination or rust [284,457]. The mapping of cracks, delamination and other defects in the concrete can be done with a crack-width ruler and acoustic-wave techniques, including the impulse-response method, impact-echo testing or ultrasonic techniques [17,458–460]. The results of the surface inspection can be provided on photography and defines the main defect points for further investigations.

Electromagnetic, elastic wave, optical sensing and infrared thermography methods are widely used in civil engineering for inspecting hard surfaces such as concrete [15,461–464]. They are mainly used for determining concrete cover depth and locating rebars with an estimate of their diameter [465]. Recent works have shown that capacitive technique and ground-penetrating radar (GPR) can also be used for monitoring rebar corrosion [466] and for providing information on water content [465,467,468] and chloride ingress [469,470]. Comparing the results obtained with ERT measurements, which can also be used to evaluate the water gradient, chloride penetration or carbonation depth [355,356], is of great interest to improve the reliability of the service life. It is also possible to complement these measurements by using embeddable chemical or optical-fibre sensors for the monitoring of pH, chloride concentration or temperature at several depths [338,471,472]. This is of great interest for assessing the initiation stage of corrosion, but their installation on existing structures can be challenging. At the end of this inspection, critical areas with a high corrosion risk can be determined.

On the weak spots, an in-depth investigation must assess the corrosion rate by determining the polarization resistance during the propagation stage of service life. The determination of the water and ionic content in concrete using ERT or embeddable chemical/optical-fibre sensors should allow to consider the environmental factors and estimate the electrochemically active surface of steel to correctly convert the polarization resistance into corrosion rate. In addition to NDT measurement, core sampling can be done at different critical locations to perform gravimetric loss tests. Though this is a destructive method, further insights on the minimum and maximum corrosion rates and other parameters of importance, e.g. concrete compressive strength, can be obtained under controlled conditions in laboratory.

Each technique provides specific information for crosschecking the results from other techniques. Data integration methods used in the operating system will further improve the overall quality of diagnosis [472], but the advantage and cost associated to each technique should be considered as well for determining the optimal methodology for each specific case. In the future, automated data collection by means of flying drones and climbing robots is expected to facilitate the inspection of RC structures and reduce the global cost of diagnosis [11]. The possibility of using a robotic device equipped with different NDT equipment is of prime interest to improve the evaluation of corrosion.

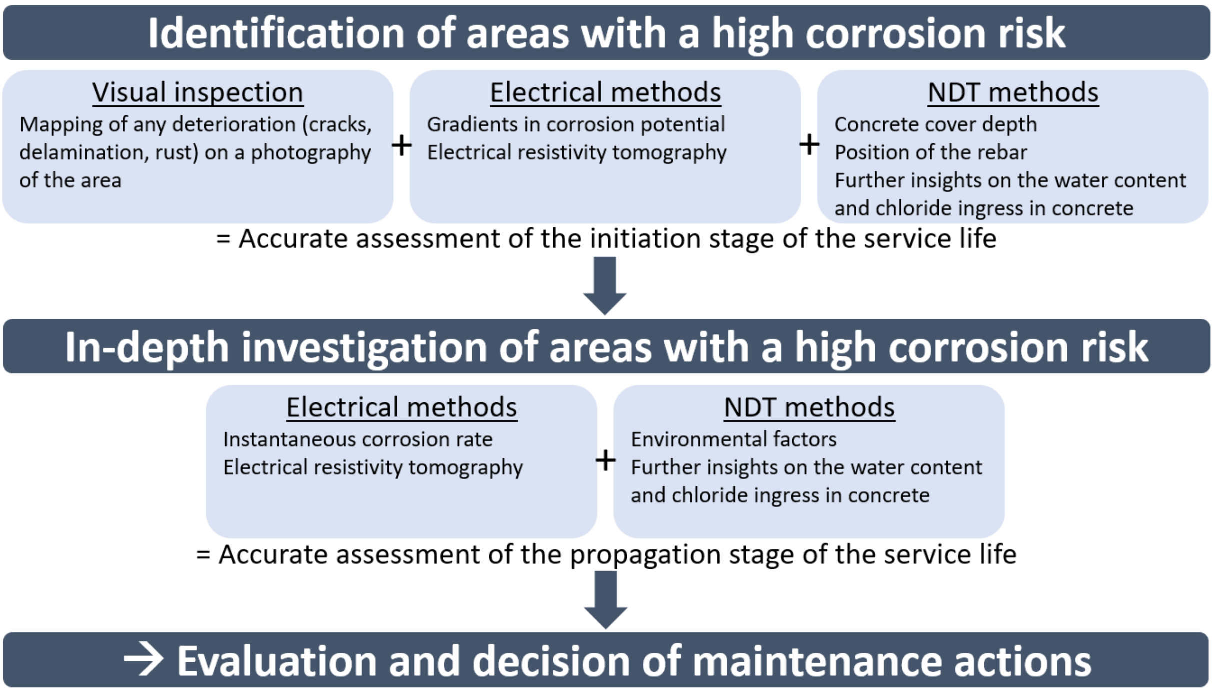

Figure 19. Procedure for the evaluation of RC structures by combining electrical and other NDT methods.

5. Conclusions and perspectives

We reviewed the current knowledge on corrosion mechanisms of carbon steel in concrete and the advances in electrical methods for non-destructive testing and evaluation of corrosion rates. One main challenge for understanding corrosion mechanisms is the heterogeneity of RC structures. Concerning cement-based materials, the knowledge of pore size distribution and pore interconnectivity is crucial as they affect the transport of aggressive agents and corrosion products through the material. Concerning steel rebar, the presence of local surface defects or inclusion substantially affects the electronic properties of the steel. The steel-concrete interface can then be very different even for replicate samples, resulting in a lack of data reproducibility. Consequently, the results obtained from different studies may be hardly comparable, especially where the description of materials and methods is incomplete. A systematic description of concrete and steel microstructures and of the operating conditions is required for the development of a database to improve our understanding of corrosion mechanisms.

Most corrosion experiments are done in laboratory conditions considering uniform corrosion on small and artificial samples. As natural corrosion is a slow process, notably because of the potentially long initiation stage, accelerated tests are generally used for studying the corrosion mechanism induced by carbonation or by chloride. However, the properties of the steel-concrete interface may not be representative of natural corrosion. In addition, the corrosion process is affected by a size effect. Hence, extrapolating laboratory results performed with a single rebar to a large structure with interconnected rebars remains challenging, and special care must be taken regarding the design and preparation of the samples to obtain meaningful information for field application.

Concerning corrosion mechanisms, the steel surface condition and local inhomogeneities at the steel-concrete interface appear to have an important effect on corrosion initiation. For actively corroding rebar, the water content and the pore size distribution around the rebar are crucial parameters when determining the electrochemically active surface for corrosion reaction. The corrosion rate increases during wetting exposure until the electrochemically active surface is water-filled, and then decreases during drying exposure. The presence and distribution of corrosion products are further parameters controlling the corrosion rate, as they can diffuse away in the concrete and control the anodic reversible potential, or they can act as depolarizing agents instead of oxygen. Hence, for atmospherically exposed RC structures, it is believed that the corrosion process is under activation control. Irrespective of the depassivation mechanism, macrocell corrosion may be the main process due to local variations in environmental exposure or the presence of interconnected rebars with different properties in engineered structures. It is then required to determine the accuracy of the proposed mechanism on non-uniform corrosion to gain further insights in the corrosion of steel in RC structures.

Regarding electrical methods, several techniques exist for determining corrosion potential, concrete resistivity and polarization resistance, which are used to assess the corrosion rate of steel. Despite being widely used, the half-cell potential technique must be used only to locate areas with a high corrosion risk as it does not permit a quantitative diagnosis of corrosion rate. Likewise, concrete resistivity is not directly related to the corrosion rate of steel. However, it is a good indicator of concrete durability in terms of water content and ion diffusivity. The use of electrical resistivity tomography allows to consider the inherent heterogeneity of concrete and provides more insights on transport phenomena in the material. It should then be possible to better predict both the initiation and the propagation stages for the assessment of the service life. Also, it has been shown that concrete resistivity influences the distribution of current within the concrete when performing any electrical measurement, so it is a parameter of prime importance for the determination of the corrosion rate.

The polarization resistance R_p remains the most important parameter during the corrosion propagation stage as it provides quantitative information on the corrosion rate. Conventional three-electrode configuration methods require a connection to the rebar to polarize it close to its natural steady-state. Good agreement with gravimetric loss for assessing the corrosion rate is well established for actively corroding rebar in laboratory. However, for passive rebar, the accurate determination of the corrosion rate can only be guaranteed when using low scan rates (<2.5 mV min^{-1}) using LPR, a long measurement time (>100 s) using GP, and low frequencies ($<10^{-3}$ Hz) using EIS. For an accurate conversion of R_p into corrosion rate, the effective polarized area of the rebar must be known but its determination appears very challenging with this conventional configuration. Even if it was developed to that issue, the use of a guard ring is not recommended as it often fails to confine the current, thus compromising the measurement. Recent studies indicate that a four-electrode configuration without any connection to the rebar is suitable for indirect polarization of the rebar. This technique ensures a self-confinement of the current, which could be helpful for determining more accurately the effective polarized area. If more studies are still required for non-uniform corrosion, especially to quantify the corrosion rate, recent advances in the development of the four-electrode configuration are promising for the assessment of non-uniform corrosion. Coupling experimental measurements with finite-element simulations appears essential to predict the remaining service life of RC structures.

Some perspectives can be proposed:

* More studies are still required to improve our understanding on corrosion mechanisms in both small-scale and large-scale structures. Alternatives for fabricating RC structures, e.g. 3D printing, may provide a solution for reducing the heterogeneity of the material; this can help to define an optimal formulation/design of concrete and to understand better corrosion mechanisms with samples of reproducible pore size distribution and steel-concrete interface conditions.

* More fundamental studies are required to convert the polarization resistance into corrosion rate, as the Stern-Geary equation—defined for uniform corrosion—generally is invalid for natural corrosion in RC structures. Currently, even with an accurate measurement of the polarization resistance, errors in the corrosion rate are to be expected with this traditional approach.

* More development on indirect polarization technique for measuring the polarization resistance is required for a complete non-destructive evaluation of corrosion on RC structures. It is required to develop monitoring device that can measure the distribution of concrete resistivity and polarization resistance in the material. The development of a single device capable of providing both parameters by electrical tomography is of great interest for the assessment of the service life of RC structures.

* A standard procedure for assessing the service life of existing RC structures must be defined. The objective is to accurately estimate an annual corrosion rate based on instantaneous corrosion rates. Models that consider seasonal variations of T and RH with only a few measurements

should be developed. For new structures, the use of various types of embedded sensors could be envisaged for automatic measurements of the environmental factors and for developing an Internet of Things (IoT) solution.

List of symbols and abbreviations used in the text

a	Electrode spacing (m)
AC	Alternating current
B	Stern-Geary constant
C_{crit}	Critical chloride content, chloride threshold value
C_{dl}	Double layer capacitance (F)
CE	Counter electrode
CPs	Corrosion products
CPE	Constant phase element
CSE	Copper-sulphate electrode
C-S-H	Calcium silicate hydrate
DC	Direct current
E	Potential (V)
E^0	Standard potential (V)
E_{corr}	Corrosion potential (V)
EEC	Electrical equivalent circuit
EIS	Electrochemical impedance spectroscopy
ERT	Electrical resistivity tomography
f	Frequency (Hz)
F	Faraday constant ($\mathrm{C\ mol^{-1}}$)
GP	Galvanostatic pulse
i	Current density ($\mathrm{A\ m^{-2}}$)
I	Current (A)
i_0	Exchange current density ($\mathrm{A\ m^{-2}}$)
ITZ	Interfacial transition zone
k	Geometric factor (m)
LPR	Linear polarization resistance
M	Molar mass ($\mathrm{g\ mol^{-1}}$)
n	Number of electrons
NDT	Non-destructive testing and evaluation
OCP	Open circuit potential (V)
OPC	Ordinary Portland cement
R	Gas constant ($\mathrm{J\ mol^{-1}\ K^{-1}}$)
R_{Ω}	Concrete resistance (Ω)
R_{p}	Polarization resistance (Ω)
RE	Reference electrode
RC	Reinforced concrete
RH	Relative humidity
SCE	Saturated-calomel electrode
SHE	Standard hydrogen electrode
t	Time (s)

T	Temperature (K)
ΔV	Potential difference (V)
w/c	Water-to-cement
WE	Working electrode
X-ray µCT	X-ray micro-computed tomography
Z	Impedance (Ω)
α_a, α_c	Anodic and cathodic charge transfer coefficients, respectively
β_a, β_c	Anodic and cathodic Tafel constants, respectively
ρ	Concrete resistivity (Ω m)
ω	Angular frequency (rad)

Conflict of interest

The authors declare no conflict of interest regarding the contents of the paper.

Acknowledgments

This study was funded by IRIS Instruments and BRGM as part of the Iris Béton project. The rebar vector design was found on Vecteezy.com. Dr H.M. Kluijver edited the English version of the manuscript.

References

[1] H. Van Damme, Concrete material science: Past, present, and future innovations, Cem. Concr. Res. 112 (2018) 5–24. https://doi.org/10.1016/j.cemconres.2018.05.002.

[2] P. Mehta, P.J.M. Monteiro, Concrete: Microstructure, Properties, and Materials, Third Edition, McGraw-Hill Companies, Inc., New York, NY, USA, 2006. https://doi.org/10.1036/0071462899.

[3] F. Bart, C. Cau-di-Coumes, F. Frizon, S. Lorente, Cement-Based Materials for Nuclear Waste Storage, Springer New York, New York, NY, 2013. https://doi.org/10.1007/978-1-4614-3445-0.

[4] V. L'Hostis, R. Gens, Performance Assessment of Concrete Structures and Engineered Barriers for Nuclear Applications, Springer Netherlands, Dordrecht, 2016. https://doi.org/10.1007/978-94-024-0904-8.

[5] J.P. Broomfield, Corrosion of Steel in Concrete: Understanding, Investigation, and Repair, E & FN Spon, 1997.

[6] S. Ahmad, Reinforcement corrosion in concrete structures, its monitoring and service life prediction – A review, Cem. Concr. Compos. 25 (2003) 459–471. https://doi.org/10.1016/S0958-9465(02)00086-0.

[7] L. Bertolini, B. Elsener, P. Pedeferri, R.B. Polder, Corrosion of Steel in Concrete: Prevention, Diagnosis, Repair, Wiley-VCH, 2013.

[8] A. Poursaee, Corrosion of Steel in Concrete Structures, Elsevier, 2016. https://doi.org/10.1016/C2014-0-01384-6.

[9] R. François, S. Laurens, F. Deby, Corrosion and its Consequences for Reinforced Concrete Structures, Elsevier, 2018. https://doi.org/10.1016/C2016-0-01228-7.

[10] R.B. Polder, W.H.A. Peelen, W.M.G. Courage, Non-traditional assessment and maintenance methods for aging concrete structures - technical and non-technical issues, Mater. Corros. 63

(2012) 1147–1153. https://doi.org/10.1002/maco.201206725.

[11] U.M. Angst, Challenges and opportunities in corrosion of steel in concrete, Mater. Struct. 51 (2018) 4. https://doi.org/10.1617/s11527-017-1131-6.

[12] D.M. McCann, M.C. Forde, Review of NDT methods in the assessment of concrete and masonry structures, NDT E Int. 34 (2001) 71–84. https://doi.org/10.1016/S0963-8695(00)00032-3.

[13] H.-W. Song, V. Saraswathy, Corrosion monitoring of reinforced concrete structures - A review, Int. J. Electrochem. Sci. 2 (2007) 1–28.

[14] S.K. Verma, S.S. Bhadauria, S. Akhtar, Review of nondestructive testing methods for condition monitoring of concrete structures, J. Constr. Eng. 2013 (2013) 1–11. https://doi.org/10.1155/2013/834572.

[15] A. Zaki, H.K. Chai, D.G. Aggelis, N. Alver, Non-destructive evaluation for corrosion monitoring in concrete: A review and capability of acoustic emission technique, Sensors. 15 (2015) 19069–19101. https://doi.org/10.3390/s150819069.

[16] A. Poursaee, Corrosion measurement and evaluation techniques of steel in concrete structures, in: Corros. Steel Concr. Struct., Woodhead Publishing, 2016: pp. 169–191. https://doi.org/10.1016/B978-1-78242-381-2.00009-2.

[17] S. Kashif Ur Rehman, Z. Ibrahim, S.A. Memon, M. Jameel, Nondestructive test methods for concrete bridges: A review, Constr. Build. Mater. 107 (2016) 58–86. https://doi.org/10.1016/j.conbuildmat.2015.12.011.

[18] D. Luo, Y. Li, J. Li, K.-S. Lim, N.A.M. Nazal, H. Ahmad, D. Luo, Y. Li, J. Li, K.-S. Lim, N.A.M. Nazal, H. Ahmad, A recent progress of steel bar corrosion diagnostic techniques in RC structures, Sensors. 19 (2018) 34. https://doi.org/10.3390/s19010034.

[19] S. Taheri, A review on five key sensors for monitoring of concrete structures, Constr. Build. Mater. 204 (2019) 492–509. https://doi.org/10.1016/j.conbuildmat.2019.01.172.

[20] D. Breysse, Non destructive assessment of concrete structures: usual combinations of techniques, in: Non-Destructive Assess. Concr. Struct. Reliab. Limits Single Comb. Tech., Springer Netherlands, Dordrecht, 2012: pp. 1–16. https://doi.org/10.1007/978-94-007-2736-6_1.

[21] J.-P. Balayssac, V. Garnier, Non-Destructive Testing and Evaluation of Civil Engineering Structures, Elsevier, 2017.

[22] H.F.W. Taylor, Cement Chemistry, 2nd Edition, Thomas Telford, London, 1997.

[23] B. Lothenbach, K. Scrivener, R.D. Hooton, Supplementary cementitious materials, Cem. Concr. Res. 41 (2011) 1244–1256. https://doi.org/10.1016/j.cemconres.2010.12.001.

[24] M.C.G. Juenger, R. Siddique, Recent advances in understanding the role of supplementary cementitious materials in concrete, Cem. Concr. Res. 78 (2015) 71–80. https://doi.org/10.1016/j.cemconres.2015.03.018.

[25] R.M. Andrew, Global CO2 emissions from cement production, Earth Syst. Sci. Data. 10 (2018) 195–217. https://doi.org/10.5194/essd-10-195-2018.

[26] J.W. Bullard, H.M. Jennings, R.A. Livingston, A. Nonat, G.W. Scherer, J.S. Schweitzer, K.L. Scrivener, J.J. Thomas, Mechanisms of cement hydration, Cem. Concr. Res. 41 (2011) 1208–1223. https://doi.org/10.1016/j.cemconres.2010.09.011.

[27] D. Marchon, R.J. Flatt, Mechanisms of cement hydration, Sci. Technol. Concr. Admixtures. (2016) 129–145. https://doi.org/10.1016/B978-0-08-100693-1.00008-4.

[28] S. Gaboreau, D. Prêt, V. Montouillout, P. Henocq, J.-C. Robinet, C. Tournassat, Quantitative mineralogical mapping of hydrated low pH concrete, Cem. Concr. Compos. 83 (2017) 360–373. https://doi.org/10.1016/j.cemconcomp.2017.08.003.

[29] ASTM_C192, Standard practice for making and curing concrete test specimens in the laboratory, (n.d.). https://www.astm.org/Standards/C192 (accessed September 12, 2018).

[30] ASTM_C31, Standard practice for making and curing concrete test specimens in the field, 2019. https://www.astm.org/Standards/C31.htm (accessed September 12, 2018).

[31] R.J.-M. Pellenq, H. Van Damme, Why does concrete set?: The nature of cohesion forces in hardened cement-based materials, MRS Bull. 29 (2004) 319–323. https://doi.org/10.1557/mrs2004.97.

[32] R.J.-M. Pellenq, N. Lequeux, H. Van Damme, Engineering the bonding scheme in C–S–H: The iono-covalent framework, Cem. Concr. Res. 38 (2008) 159–174. https://doi.org/10.1016/j.cemconres.2007.09.026.

[33] H. Manzano, S. Moeini, F. Marinelli, A.C.T. van Duin, F.-J. Ulm, R.J.-M. Pellenq, Confined water dissociation in microporous defective silicates: Mechanism, dipole distribution, and impact on substrate properties, J. Am. Chem. Soc. 134 (2012) 2208–2215. https://doi.org/10.1021/ja209152n.

[34] P.A. Bonnaud, Q. Ji, B. Coasne, R.J.-M. Pellenq, K.J. Van Vliet, Thermodynamics of water confined in porous calcium-silicate-hydrates, Langmuir. 28 (2012) 11422–11432. https://doi.org/10.1021/la301738p.

[35] P.A. Bonnaud, Q. Ji, K.J. Van Vliet, Effects of elevated temperature on the structure and properties of calcium–silicate–hydrate gels: the role of confined water, Soft Matter. 9 (2013) 6418. https://doi.org/10.1039/c3sm50975c.

[36] P. Blanc, X. Bourbon, A. Lassin, E.C. Gaucher, Chemical model for cement-based materials: Temperature dependence of thermodynamic functions for nanocrystalline and crystalline C–S–H phases, Cem. Concr. Res. 40 (2010) 851–866. https://doi.org/10.1016/j.cemconres.2009.12.004.

[37] P. Blanc, X. Bourbon, A. Lassin, E.C. Gaucher, Chemical model for cement-based materials: Thermodynamic data assessment for phases other than C–S–H, Cem. Concr. Res. 40 (2010) 1360–1374. https://doi.org/10.1016/j.cemconres.2010.04.003.

[38] C. Roosz, S. Gaboreau, S. Grangeon, D. Prêt, V. Montouillout, N. Maubec, S. Ory, P. Blanc, P. Vieillard, P. Henocq, Distribution of water in synthetic calcium silicate hydrates, Langmuir. 32 (2016) 6794–6805. https://doi.org/10.1021/acs.langmuir.6b00878.

[39] C. Roosz, P. Vieillard, P. Blanc, S. Gaboreau, H. Gailhanou, D. Braithwaite, V. Montouillout, R. Denoyel, P. Henocq, B. Madé, Thermodynamic properties of C-S-H, C-A-S-H and M-S-H phases: Results from direct measurements and predictive modelling, Appl. Geochemistry. 92 (2018) 140–156. https://doi.org/10.1016/j.apgeochem.2018.03.004.

[40] B. Lothenbach, M. Zajac, Application of thermodynamic modelling to hydrated cements, Cem. Concr. Res. 123 (2019) 105779. https://doi.org/10.1016/j.cemconres.2019.105779.

[41] S. Gaboreau, S. Grangeon, F. Claret, D. Ihiawakrim, O. Ersen, V. Montouillout, N. Maubec, C. Roosz, P. Henocq, C. Carteret, Hydration properties and interlayer organization in synthetic C-

S-H, Langmuir. 36 (2020) 9449–9464. https://doi.org/10.1021/acs.langmuir.0c01335.

[42] B. Lothenbach, A. Nonat, Calcium silicate hydrates: Solid and liquid phase composition, Cem. Concr. Res. 78 (2015) 57–70. https://doi.org/10.1016/j.cemconres.2015.03.019.

[43] C.S. Walker, S. Sutou, C. Oda, M. Mihara, A. Honda, Calcium silicate hydrate (C-S-H) gel solubility data and a discrete solid phase model at 25 °C based on two binary non-ideal solid solutions, Cem. Concr. Res. 79 (2016) 1–30. https://doi.org/10.1016/j.cemconres.2015.07.006.

[44] G.M.N. Baston, A.P. Clacher, T.G. Heath, F.M.I. Hunter, V. Smith, S.W. Swanton, Calcium silicate hydrate (C-S-H) gel dissolution and pH buffering in a cementitious near field, Mineral. Mag. 76 (2012) 3045–3053. https://doi.org/10.1180/minmag.2012.076.8.20.

[45] H.W. Whittington, J. McCarter, M.C. Forde, The conduction of electricity through concrete, Mag. Concr. Res. 33 (1981) 48–60. https://doi.org/10.1680/macr.1981.33.114.48.

[46] R.A. Patel, Q.T. Phung, S.C. Seetharam, J. Perko, D. Jacques, N. Maes, G. De Schutter, G. Ye, K. Van Breugel, Diffusivity of saturated ordinary Portland cement-based materials: A critical review of experimental and analytical modelling approaches, Cem. Concr. Res. 90 (2016) 52–72. https://doi.org/10.1016/j.cemconres.2016.09.015.

[47] M. Parisatto, M.C. Dalconi, L. Valentini, G. Artioli, A. Rack, R. Tucoulou, G. Cruciani, G. Ferrari, Examining microstructural evolution of Portland cements by in-situ synchrotron micro-tomography, J. Mater. Sci. 50 (2015) 1805–1817. https://doi.org/10.1007/s10853-014-8743-9.

[48] M. Moradian, Q. Hu, M. Aboustait, M.T. Ley, J.C. Hanan, X. Xiao, G.W. Scherer, Z. Zhang, Direct observation of void evolution during cement hydration, Mater. Des. 136 (2017) 137–149. https://doi.org/10.1016/j.matdes.2017.09.056.

[49] Z. Zhang, G.W. Scherer, A. Bauer, Morphology of cementitious material during early hydration, Cem. Concr. Res. 107 (2018) 85–100. https://doi.org/10.1016/j.cemconres.2018.02.004.

[50] A. Elsharief, M.D. Cohen, J. Olek, Influence of aggregate size, water cement ratio and age on the microstructure of the interfacial transition zone, Cem. Concr. Res. 33 (2003) 1837–1849. https://doi.org/10.1016/S0008-8846(03)00205-9.

[51] Z. Zhang, U. Angst, A discussion of the paper “Effect of design parameters on microstructure of steel-concrete interface in reinforced concrete,” Cem. Concr. Res. 128 (2020) 105949. https://doi.org/10.1016/j.cemconres.2019.105949.

[52] A.B. Abell, K.L. Willis, D.A. Lange, Mercury intrusion porosimetry and image analysis of cement-based materials, J. Colloid Interface Sci. 211 (1999) 39–44. https://doi.org/10.1006/jcis.1998.5986.

[53] S. Diamond, The microstructure of cement paste and concrete––a visual primer, Cem. Concr. Compos. 26 (2004) 919–933. https://doi.org/10.1016/j.cemconcomp.2004.02.028.

[54] K.L. Scrivener, Backscattered electron imaging of cementitious microstructures: understanding and quantification, Cem. Concr. Compos. 26 (2004) 935–945. https://doi.org/10.1016/j.cemconcomp.2004.02.029.

[55] H.S. Wong, M.K. Head, N.R. Buenfeld, Pore segmentation of cement-based materials from backscattered electron images, Cem. Concr. Res. 36 (2006) 1083–1090. https://doi.org/10.1016/j.cemconres.2005.10.006.

[56] S.-Y. Chung, J.-S. Kim, D. Stephan, T.-S. Han, Overview of the use of micro-computed

tomography (micro-CT) to investigate the relation between the material characteristics and properties of cement-based materials, Constr. Build. Mater. 229 (2019) 116843. https://doi.org/10.1016/j.conbuildmat.2019.116843.

[57] S. Brisard, M. Serdar, P.J.M. Monteiro, Multiscale X-ray tomography of cementitious materials: A review, Cem. Concr. Res. 128 (2020) 105824. https://doi.org/10.1016/j.cemconres.2019.105824.

[58] P. Leroy, A. Hördt, S. Gaboreau, E. Zimmermann, F. Claret, M. Bücker, H. Stebner, J.A. Huisman, Spectral induced polarization of low-pH cement and concrete, Cem. Concr. Compos. 104 (2019) 103397. https://doi.org/10.1016/j.cemconcomp.2019.103397.

[59] D. Clover, B. Kinsella, B. Pejcic, R. De Marco, The influence of microstructure on the corrosion rate of various carbon steels, J. Appl. Electrochem. 35 (2005) 139–149. https://doi.org/10.1007/s10800-004-6207-7.

[60] R.R. Hussain, J.K. Singh, A. Alhozaimy, A. Al-Negheimish, C. Bhattacharya, R.S. Pathania, D.D.N. Singh, Effect of reinforcing bar microstructure on passive film exposed to simulated concrete pore solution, ACI Mater. J. 115 (2018) 181–190. https://doi.org/10.14359/51701237.

[61] P.K. Katiyar, P.K. Behera, S. Misra, K. Mondal, Comparative corrosion behavior of five different microstructures of rebar steels in simulated concrete pore solution with and without chloride addition, J. Mater. Eng. Perform. 28 (2019) 6275–6286. https://doi.org/10.1007/s11665-019-04339-x.

[62] H. Torbati-Sarraf, A. Poursaee, The influence of phase distribution and microstructure of the carbon steel on its chloride threshold value in a simulated concrete pore solution, Constr. Build. Mater. 259 (2020) 119784. https://doi.org/10.1016/j.conbuildmat.2020.119784.

[63] U.M. Angst, M.R. Geiker, A. Michel, C. Gehlen, H. Wong, O.B. Isgor, B. Elsener, C.M. Hansson, R. François, K. Hornbostel, R. Polder, M.C. Alonso, M. Sanchez, M.J. Correia, M. Criado, A. Sagüés, N. Buenfeld, The steel–concrete interface, Mater. Struct. 50 (2017) 143. https://doi.org/10.1617/s11527-017-1010-1.

[64] P. Ghods, O.B. Isgor, G.A. McRae, J. Li, G.P. Gu, Microscopic investigation of mill scale and its proposed effect on the variability of chloride-induced depassivation of carbon steel rebar, Corros. Sci. 53 (2011) 946–954. https://doi.org/10.1016/j.corsci.2010.11.025.

[65] L. Tang, J.M. Frederiksen, U.M. Angst, R. Polder, M.C. Alonso, B. Elsener, D. Hooton, J. Pacheco, Experiences from RILEM TC 235-CTC in recommending a test method for chloride threshold values in concrete, RILEM Tech. Lett. 3 (2018) 25–31. https://doi.org/10.21809/rilemtechlett.2018.55.

[66] L. Ding, H. Torbati-Sarraf, A. Poursaee, The influence of the sandblasting as a surface mechanical attrition treatment on the electrochemical behavior of carbon steel in different pH solutions, Surf. Coatings Technol. 352 (2018) 112–119. https://doi.org/10.1016/j.surfcoat.2018.08.013.

[67] L.T. Mammoliti, L.C. Brown, C.M. Hansson, B.B. Hope, The influence of surface finish of reinforcing steel and pH of the test solution on the chloride threshold concentration for corrosion initiation in synthetic pore solutions, Cem. Concr. Res. 26 (1996) 545–550. https://doi.org/10.1016/0008-8846(96)00018-X.

[68] H. Tamura, The role of rusts in corrosion and corrosion protection of iron and steel, Corros. Sci. 50 (2008) 1872–1883. https://doi.org/10.1016/j.corsci.2008.03.008.

[69] J. Ming, J. Shi, W. Sun, Effect of mill scale on the long-term corrosion resistance of a low-alloy

reinforcing steel in concrete subjected to chloride solution, Constr. Build. Mater. 163 (2018) 508–517. https://doi.org/10.1016/j.conbuildmat.2017.12.125.

[70] A.J. Al-Tayyib, M.S. Khan, I.M. Allam, A.I. Al-Mana, Corrosion behavior of pre-rusted rebars after placement in concrete, Cem. Concr. Res. 20 (1990) 955–960. https://doi.org/10.1016/0008-8846(90)90059-7.

[71] C. Hansson, B. Sørensen, The threshold concentration of chloride in concrete for the initiation of reinforcement corrosion, in: Corros. Rates Steel Concr., ASTM International, 100 Barr Harbor Drive, PO Box C700, West Conshohocken, PA 19428-2959, 1990: pp. 3-3–14. https://doi.org/10.1520/STP25011S.

[72] P. Novak, R. Mala, L. Joska, Influence of pre-rusting on steel corrosion in concrete, Cem. Concr. Res. 31 (2001) 589–593. https://doi.org/10.1016/S0008-8846(01)00459-8.

[73] E. Mahallati, M. Saremi, An assessment on the mill scale effects on the electrochemical characteristics of steel bars in concrete under DC-polarization, Cem. Concr. Res. 36 (2006) 1324–1329. https://doi.org/10.1016/j.cemconres.2006.03.015.

[74] T.U. Mohammed, H. Hamada, Corrosion of steel bars in concrete with various steel surface conditions, ACI Mater. J. 103 (2006) 233–242. https://doi.org/10.14359/16606.

[75] D. Boubitsas, L. Tang, The influence of reinforcement steel surface condition on initiation of chloride induced corrosion, Mater. Struct. 48 (2015) 2641–2658. https://doi.org/10.1617/s11527-014-0343-2.

[76] J.A. González, E. Ramírez, A. Bautista, S. Feliu, The behaviour of pre-rusted steel in concrete, Cem. Concr. Res. 26 (1996) 501–511. https://doi.org/10.1016/S0008-8846(96)85037-X.

[77] C. Chalhoub, R. François, M. Carcasses, Critical chloride threshold values as a function of cement type and steel surface condition, Cem. Concr. Res. 134 (2020) 106086. https://doi.org/10.1016/j.cemconres.2020.106086.

[78] M.J. Martinez-Echevarria, M. Lopez-Alonso, D. Cantero Romero, J. Rodríguez Montero, Influence of the previous state of corrosion of rebars in predicting the service life of reinforced concrete structures, Constr. Build. Mater. 188 (2018) 915–923. https://doi.org/10.1016/j.conbuildmat.2018.08.173.

[79] L. Michel, U. Angst, Towards understanding corrosion initiation in concrete – Influence of local electrochemical properties of reinforcing steel, MATEC Web Conf. 199 (2018) 04001. https://doi.org/10.1051/matecconf/201819904001.

[80] U.M. Angst, M.R. Geiker, M.C. Alonso, R. Polder, O.B. Isgor, B. Elsener, H. Wong, A. Michel, K. Hornbostel, C. Gehlen, R. François, M. Sanchez, M. Criado, H. Sørensen, C. Hansson, R. Pillai, S. Mundra, J. Gulikers, M. Raupach, J. Pacheco, A. Sagüés, The effect of the steel–concrete interface on chloride-induced corrosion initiation in concrete: a critical review by RILEM TC 262-SCI, Mater. Struct. 52 (2019) 88. https://doi.org/10.1617/s11527-019-1387-0.

[81] X.R. Nóvoa, Electrochemical aspects of the steel-concrete system. A review, J. Solid State Electrochem. 20 (2016) 2113–2125. https://doi.org/10.1007/s10008-016-3238-z.

[82] S. Joiret, M. Keddam, X.R. Nóvoa, M.C. Pérez, C. Rangel, H. Takenouti, Use of EIS, ring-disk electrode, EQCM and Raman spectroscopy to study the film of oxides formed on iron in 1 M NaOH, Cem. Concr. Compos. 24 (2002) 7–15. https://doi.org/10.1016/S0958-9465(01)00022-1.

[83] A. Poursaee, C.M. Hansson, Reinforcing steel passivation in mortar and pore solution, Cem.

Concr. Res. 37 (2007) 1127–1133. https://doi.org/10.1016/j.cemconres.2007.04.005.

[84] S.M. Abd El Haleem, E.E. Abd El Aal, S. Abd El Wanees, A. Diab, Environmental factors affecting the corrosion behaviour of reinforcing steel: I. The early stage of passive film formation in Ca(OH)2 solutions, Corros. Sci. 52 (2010) 3875–3882. https://doi.org/10.1016/j.corsci.2010.07.035.

[85] H. DorMohammadi, Q. Pang, P. Murkute, L. Arnadottir, O. Burkan Isgor, Investigation of iron passivity in highly alkaline media using reactive-force field molecular dynamics, Corros. Sci. (2019). https://doi.org/10.1016/j.corsci.2019.05.016.

[86] E. Volpi, A. Olietti, M. Stefanoni, S.P. Trasatti, Electrochemical characterization of mild steel in alkaline solutions simulating concrete environment, J. Electroanal. Chem. 736 (2015) 38–46. https://doi.org/10.1016/j.jelechem.2014.10.023.

[87] B. Elsener, A. Rossi, Passivation of steel and stainless steel in alkaline media simulating concrete, in: Encycl. Interfacial Chem., Elsevier, 2018: pp. 365–375. https://doi.org/10.1016/B978-0-12-409547-2.13772-2.

[88] C. Andrade, P. Merino, X.R. Nóvoa, M.C. Pérez, L. Soler, Passivation of reinforcing steel in concrete, Mater. Sci. Forum. 192–194 (1995) 891–898. https://doi.org/10.4028/www.scientific.net/MSF.192-194.891.

[89] X.R. Nóvoa, M.C. Pérez, On the role of iron oxides in the electrochemical behaviour of steel embedded in concrete, Corros. Rev. 23 (2005) 195–216. https://doi.org/10.1515/corrrev.2005.23.2-3.195.

[90] M. Sánchez, J. Gregori, C. Alonso, J.J. García-Jareño, H. Takenouti, F. Vicente, Electrochemical impedance spectroscopy for studying passive layers on steel rebars immersed in alkaline solutions simulating concrete pores, Electrochim. Acta. 52 (2007) 7634–7641. https://doi.org/10.1016/j.electacta.2007.02.012.

[91] J. Williamson, O.B. Isgor, The effect of simulated concrete pore solution composition and chlorides on the electronic properties of passive films on carbon steel rebar, Corros. Sci. 106 (2016) 82–95. https://doi.org/10.1016/j.corsci.2016.01.027.

[92] A. Poursaee, Corrosion of steel in concrete structures, in: Corros. Steel Concr. Struct., Woodhead Publishing, 2016: pp. 19–33. https://doi.org/10.1016/B978-1-78242-381-2.00002-X.

[93] H.B. Gunay, O.B. Isgor, P. Ghods, Kinetics of passivation and chloride-induced depassivation of iron in simulated concrete pore solutions using electrochemical quartz crystal nanobalance, Corrosion. 71 (2015) 615–627. https://doi.org/10.5006/1346.

[94] M.F. Montemor, A.M.P. Simões, M.G.S. Ferreira, Analytical characterization of the passive film formed on steel in solutions simulating the concrete interstitial electrolyte, Corrosion. 54 (1998) 347–353. https://doi.org/10.5006/1.3284861.

[95] P. Ghods, O.B. Isgor, G. McRae, T. Miller, The effect of concrete pore solution composition on the quality of passive oxide films on black steel reinforcement, Cem. Concr. Compos. 31 (2009) 2–11. https://doi.org/10.1016/j.cemconcomp.2008.10.003.

[96] A.T. Horne, I.G. Richardson, R.M.D. Brydson, Quantitative analysis of the microstructure of interfaces in steel reinforced concrete, Cem. Concr. Res. 37 (2007) 1613–1623. https://doi.org/10.1016/j.cemconres.2007.08.026.

[97] A. Kenny, A. Katz, Statistical relationship between mix properties and the interfacial transition

zone around embedded rebar, Cem. Concr. Compos. 60 (2015) 82–91. https://doi.org/10.1016/j.cemconcomp.2015.04.002.

[98] Y. Cai, W. Zhang, L. Yu, M. Chen, C. Yang, R. François, K. Yang, Characteristics of the steel-concrete interface and their effect on the corrosion of steel bars in concrete, Constr. Build. Mater. 253 (2020) 119162. https://doi.org/10.1016/j.conbuildmat.2020.119162.

[99] T.A. Soylev, R. François, Quality of steel–concrete interface and corrosion of reinforcing steel, Cem. Concr. Res. 33 (2003) 1407–1415. https://doi.org/10.1016/S0008-8846(03)00087-5.

[100] G.K. Glass, R. Yang, T. Dickhaus, N.R. Buenfeld, Backscattered electron imaging of the steel–concrete interface, Corros. Sci. 43 (2001) 605–610. https://doi.org/10.1016/S0010-938X(00)00146-3.

[101] F. Chen, C.-Q. Li, H. Baji, B. Ma, Quantification of steel-concrete interface in reinforced concrete using backscattered electron imaging technique, Constr. Build. Mater. 179 (2018) 420–429. https://doi.org/10.1016/j.conbuildmat.2018.05.246.

[102] S.K. Goudar, B.B. Das, S.B. Arya, K.N. Shivaprasad, Influence of sample preparation techniques on microstructure and nano-mechanical properties of steel-concrete interface, Constr. Build. Mater. 256 (2020) 119242. https://doi.org/10.1016/j.conbuildmat.2020.119242.

[103] Z. Zhang, M. Shakoorioskooie, M. Griffa, P. Lura, U. Angst, A laboratory investigation of cutting damage to the steel-concrete interface, Cem. Concr. Res. 138 (2020) 106229. https://doi.org/10.1016/j.cemconres.2020.106229.

[104] K. Tuutti, Corrosion of Steel in Concrete, Swedish Cement and Concrete Research Institute, Stockholm, 1982.

[105] C. Andrade, C. Alonso, J. Gulikers, R. Polder, R. Cigna, Ø. Vennesland, M. Salta, A. Raharinaivo, B. Elsener, Test methods for on-site corrosion rate measurement of steel reinforcement in concrete by means of the polarization resistance method, Mater. Struct. 37 (2004) 623–642. https://doi.org/10.1007/BF02483292.

[106] C. Qing Li, Reliability based service life prediction of corrosion affected concrete structures, J. Struct. Eng. 130 (2004) 1570–1577. https://doi.org/10.1061/(ASCE)0733-9445(2004)130:10(1570).

[107] M. Raupach, Models for the propagation phase of reinforcement corrosion – an overview, Mater. Corros. 57 (2006) 605–613. https://doi.org/10.1002/maco.200603991.

[108] M.B. Otieno, H.D. Beushausen, M.G. Alexander, Modelling corrosion propagation in reinforced concrete structures – A critical review, Cem. Concr. Compos. 33 (2011) 240–245. https://doi.org/10.1016/j.cemconcomp.2010.11.002.

[109] D. Chen, S. Mahadevan, Chloride-induced reinforcement corrosion and concrete cracking simulation, Cem. Concr. Compos. 30 (2008) 227–238. https://doi.org/10.1016/.cemconcomp.2006.10.007.

[110] F. Chen, H. Baji, C.-Q. Li, A comparative study on factors affecting time to cover cracking as a service life indicator, Constr. Build. Mater. 163 (2018) 681–694. https://doi.org/10.1016/j.conbuildmat.2017.12.120.

[111] M. Alexander, H. Beushausen, Durability, service life prediction, and modelling for reinforced concrete structures – review and critique, Cem. Concr. Res. 122 (2019) 17–29. https://doi.org/10.1016/j.cemconres.2019.04.018.

[112] O.B. Isgor, A.G. Razaqpur, Modelling steel corrosion in concrete structures, Mater. Struct. 39

(2006) 291–302. https://doi.org/10.1007/s11527-005-9022-7.

[113] Z.M. Mir, D. Höche, C. Gomes, R. Sampaio, A.C. Bastos, P. Maincon, M.G.S. Ferreira, M.L. Zheludkevich, Enhanced predictive modelling of steel corrosion in concrete in submerged zone based on a dynamic activation approach, Int. J. Concr. Struct. Mater. 13 (2019) 11. https://doi.org/10.1186/s40069-018-0321-0.

[114] O.A. Kayyali, M.N. Haque, Effect of carbonation on the chloride concentration in pore solution of mortars with and without flyash, Cem. Concr. Res. 18 (1988) 636–648. https://doi.org/10.1016/0008-8846(88)90056-7.

[115] X. Zhu, G. Zi, Z. Cao, X. Cheng, Combined effect of carbonation and chloride ingress in concrete, Constr. Build. Mater. 110 (2016) 369–380. https://doi.org/10.1016/j.conbuildmat.2016.02.034.

[116] J. Geng, D. Easterbrook, Q.-F. Liu, L.-Y. Li, Effect of carbonation on release of bound chlorides in chloride-contaminated concrete, Mag. Concr. Res. 68 (2016) 353–363. https://doi.org/10.1680/jmacr.15.00234.

[117] J.A. Gonzalez, J.S. Algaba, C. Andrade, Corrosion of reinforcing bars in carbonated concrete, Br. Corros. J. 15 (1980) 135–139. https://doi.org/10.1179/bcj.1980.15.3.135.

[118] C. Alonso, C. Andrade, Corrosion of steel reinforcement in carbonated mortar containing chlorides, Adv. Cem. Res. 1 (1988) 155–163. https://doi.org/10.1680/1988.1.3.155.

[119] D.A. Hausmann, Steel corrosion in concrete. How does it occur?, J. Mater. Prot. 6 (1967) 19–23.

[120] M. Stratmann, J. Müller, The mechanism of the oxygen reduction on rust-covered metal substrates, Corros. Sci. 36 (1994) 327–359. https://doi.org/10.1016/0010-938X(94)90161-9.

[121] C.M. Hansson, Comments on electrochemical measurements of the rate of corrosion of steel in concrete, Cem. Concr. Res. 14 (1984) 574–584. https://doi.org/10.1016/0008-8846(84)90135-2.

[122] M. Pourbaix, Thermodynamics and corrosion, Corros. Sci. 30 (1990) 963–988. https://doi.org/10.1016/0010-938X(90)90205-J.

[123] R. François, S. Laurens, F. Deby, Steel Corrosion in Reinforced Concrete, in: Corros. Its Consequences Reinf. Concr. Struct., Elsevier, 2018: pp. 1–41. https://doi.org/10.1016/B978-1-78548-234-2.50001-9.

[124] M. Stefanoni, U.M. Angst, B. Elsener, Electrochemistry and capillary condensation theory reveal the mechanism of corrosion in dense porous media, Sci. Rep. 8 (2018) 7407. https://doi.org/10.1038/s41598-018-25794-x.

[125] M. Stefanoni, U.M. Angst, B. Elsener, Kinetics of electrochemical dissolution of metals in porous media, Nat. Mater. 18 (2019) 942–947. https://doi.org/10.1038/s41563-019-0439-8.

[126] M. Pour-Ghaz, O. Burkan Isgor, P. Ghods, The effect of temperature on the corrosion of steel in concrete. Part 1: Simulated polarization resistance tests and model development, Corros. Sci. 51 (2009) 415–425. https://doi.org/10.1016/j.corsci.2008.10.034.

[127] M. Pour-Ghaz, O. Burkan Isgor, P. Ghods, The effect of temperature on the corrosion of steel in concrete. Part 2: Model verification and parametric study, Corros. Sci. 51 (2009) 426–433. https://doi.org/10.1016/j.corsci.2008.10.036.

[128] E. Rossi, R. Polder, O. Copuroglu, T. Nijland, B. Šavija, The influence of defects at the

steel/concrete interface for chloride-induced pitting corrosion of naturally-deteriorated 20-years-old specimens studied through X-ray Computed Tomography, Constr. Build. Mater. 235 (2020) 117474. https://doi.org/10.1016/j.conbuildmat.2019.117474.

[129] B. Huet, V. L'Hostis, G. Santarini, D. Feron, H. Idrissi, Steel corrosion in concrete: Determinist modeling of cathodic reaction as a function of water saturation degree, Corros. Sci. 49 (2007) 1918–1932. https://doi.org/10.1016/j.corsci.2006.10.005.

[130] C. Cao, M.M.S. Cheung, B.Y.B. Chan, Modelling of interaction between corrosion-induced concrete cover crack and steel corrosion rate, Corros. Sci. 69 (2013) 97–109. https://doi.org/10.1016/j.corsci.2012.11.028.

[131] Y. Zhao, W. Jin, Steel Corrosion in Concrete, in: Steel Corros. Concr. Crack., Butterworth-Heinemann, 2016: pp. 19–29. https://doi.org/10.1016/B978-0-12-809197-5.00002-5.

[132] M. Stefanoni, Z. Zhang, U. Angst, B. Elsener, The kinetic competition between transport and oxidation of ferrous ions governs precipitation of corrosion products in carbonated concrete, RILEM Tech. Lett. 3 (2018) 8–16. https://doi.org/10.21809/rilemtechlett.2018.57.

[133] P. Blanc, A. Lassin, P. Piantone, M. Azaroual, N. Jacquemet, A. Fabbri, E.C. Gaucher, Thermoddem: A geochemical database focused on low temperature water/rock interactions and waste materials, Appl. Geochemistry. 27 (2012) 2107–2116. https://doi.org/10.1016/j.apgeochem.2012.06.002.

[134] B. Šavija, M. Luković, Carbonation of cement paste: Understanding, challenges, and opportunities, Constr. Build. Mater. 117 (2016) 285–301. https://doi.org/10.1016/j.conbuildmat.2016.04.138.

[135] V.G. Papadakis, C.G. Vayenas, M.N. Fardis, Fundamental modeling and experimental investigation of concrete carbonation, ACI Mater. J. 88 (1991) 363–373. https://doi.org/10.14359/1863.

[136] V.G. Papadakis, C.G. Vayenas, M.N. Fardis, Physical and chemical characteristics affecting the durability of concrete, ACI Mater. J. 88 (1991) 186–196. https://doi.org/10.14359/1993.

[137] Y.F. Houst, F.H. Wittmann, Influence of porosity and water content on the diffusivity of CO2 and O2 through hydrated cement paste, Cem. Concr. Res. 24 (1994) 1165–1176. https://doi.org/10.1016/0008-8846(94)90040-X.

[138] P. Castro, M.A. Sanjuán, J. Genescá, Carbonation of concretes in the Mexican Gulf, Build. Environ. 35 (2000) 145–149. https://doi.org/10.1016/S0360-1323(99)00009-8.

[139] J.H.M. Visser, Influence of the carbon dioxide concentration on the resistance to carbonation of concrete, Constr. Build. Mater. 67 (2014) 8–13. https://doi.org/10.1016/j.conbuildmat.2013.11.005.

[140] A. Morandeau, M. Thiéry, P. Dangla, Investigation of the carbonation mechanism of CH and C-S-H in terms of kinetics, microstructure changes and moisture properties, Cem. Concr. Res. 56 (2014) 153–170. https://doi.org/10.1016/j.cemconres.2013.11.015.

[141] I. Galan, C. Andrade, M. Castellote, Natural and accelerated CO2 binding kinetics in cement paste at different relative humidities, Cem. Concr. Res. 49 (2013) 21–28. https://doi.org/10.1016/j.cemconres.2013.03.009.

[142] Q. Huy Vu, G. Pham, A. Chonier, E. Brouard, S. Rathnarajan, R. Pillai, R. Gettu, M. Santhanam, F. Aguayo, K.J. Folliard, M.D. Thomas, T. Moffat, C. Shi, A. Sarnot, Impact of different climates on the resistance of concrete to natural carbonation, Constr. Build. Mater. 216 (2019) 450–

467. https://doi.org/10.1016/j.conbuildmat.2019.04.263.

[143] S.K. Roy, P.K. Beng, D.O. Northwood, The carbonation of concrete structures in the tropical environment of singapore and a comparison with published data for temperate climates, Mag. Concr. Res. 48 (1996) 293–300. https://doi.org/10.1680/macr.1996.48.177.293.

[144] M.N. Haque, H. Al-Khaiat, Carbonation of concrete structures in hot dry coastal regions, Cem. Concr. Compos. 19 (1997) 123–129. https://doi.org/10.1016/s0958-9465(96)00047-9.

[145] A. Leemann, F. Moro, Carbonation of concrete: the role of CO2 concentration, relative humidity and CO2 buffer capacity, Mater. Struct. 50 (2017) 30. https://doi.org/10.1617/s11527-016-0917-2.

[146] E. Drouet, S. Poyet, P. Le Bescop, J.-M. Torrenti, X. Bourbon, Carbonation of hardened cement pastes: Influence of temperature, Cem. Concr. Res. 115 (2019) 445–459. https://doi.org/10.1016/j.cemconres.2018.09.019.

[147] A. V. Saetta, B.A. Schrefler, R. V. Vitaliani, The carbonation of concrete and the mechanism of moisture, heat and carbon dioxide flow through porous materials, Cem. Concr. Res. 23 (1993) 761–772. https://doi.org/10.1016/0008-8846(93)90030-D.

[148] A. V. Saetta, R. V. Vitaliani, Experimental investigation and numerical modeling of carbonation process in reinforced concrete structures Part I: Theoretical formulation, Cem. Concr. Res. 34 (2004) 571–579. https://doi.org/10.1016/j.cemconres.2003.09.009.

[149] O.B. Isgor, A.G.G. Razaqpur, Finite element modeling of coupled heat transfer, moisture transport and carbonation processes in concrete structures, Cem. Concr. Compos. 26 (2004) 57–73. https://doi.org/10.1016/S0958-9465(02)00125-7.

[150] V.G. Papadakis, C.G. Vayenas, M.N. Fardis, A reaction engineering approach to the problem of concrete carbonation, AIChE J. 35 (1989) 1639–1650. https://doi.org/10.1002/aic.690351008.

[151] B. Johannesson, P. Utgenannt, Microstructural changes caused by carbonation of cement mortar, Cem. Concr. Res. 31 (2001) 925–931. https://doi.org/10.1016/S0008-8846(01)00498-7.

[152] W. Ashraf, Carbonation of cement-based materials: Challenges and opportunities, Constr. Build. Mater. 120 (2016) 558–570. https://doi.org/10.1016/j.conbuildmat.2016.05.080.

[153] S.E. Pihlajavaara, Some results of the effect of carbonation on the porosity and pore size distribution of cement paste, Matériaux Constr. 1 (1968) 521–527. https://doi.org/10.1007/BF02473640.

[154] M. Auroy, S. Poyet, P. Le Bescop, J.-M. Torrenti, T. Charpentier, M. Moskura, X. Bourbon, Impact of carbonation on unsaturated water transport properties of cement-based materials, Cem. Concr. Res. 74 (2015) 44–58. https://doi.org/10.1016/j.cemconres.2015.04.002.

[155] V.T. Ngala, C.L. Page, Effects of carbonation on pore structure and diffusional properties of hydrated cement pastes, Cem. Concr. Res. 27 (1997) 995–1007. https://doi.org/10.1016/S0008-8846(97)00102-6.

[156] S. Laurens, F. Deby, Electrochemical Methods, in: Non-Destructive Test. Eval. Civ. Eng. Struct., Elsevier, 2018: pp. 173–197. https://doi.org/10.1016/B978-1-78548-229-8.50005-4.

[157] M. Castellote, L. Fernandez, C. Andrade, C. Alonso, Chemical changes and phase analysis of OPC pastes carbonated at different CO2 concentrations, Mater. Struct. 42 (2009) 515–525. https://doi.org/10.1617/s11527-008-9399-1.

[158] M. Auroy, S. Poyet, P. Le Bescop, J.-M. Torrenti, T. Charpentier, M. Moskura, X. Bourbon, Comparison between natural and accelerated carbonation (3% CO2): Impact on mineralogy, microstructure, water retention and cracking, Cem. Concr. Res. 109 (2018) 64–80. https://doi.org/10.1016/j.cemconres.2018.04.012.

[159] B. Huet, V. L'Hostis, F. Miserque, H. Idrissi, Electrochemical behavior of mild steel in concrete: Influence of pH and carbonate content of concrete pore solution, Electrochim. Acta. 51 (2005) 172–180. https://doi.org/10.1016/j.electacta.2005.04.014.

[160] V. Marcos-Meson, A. Michel, A. Solgaard, G. Fischer, C. Edvardsen, T.L. Skovhus, Corrosion resistance of steel fibre reinforced concrete - A literature review, Cem. Concr. Res. 103 (2018) 1–20. https://doi.org/10.1016/j.cemconres.2017.05.016.

[161] M. Thiery, Modelling of atmospheric carbonation of cement based materials considering the kinetic effects and modifications of the microstructure and the hydric state, Ecole des Ponts ParisTech, 2005.

[162] M.G. Sohail, S. Laurens, F. Deby, J.P. Balayssac, Significance of macrocell corrosion of reinforcing steel in partially carbonated concrete: numerical and experimental investigation, Mater. Struct. 48 (2015) 217–233. https://doi.org/10.1617/s11527-013-0178-2.

[163] A.B. Revert, K. De Weerdt, K. Hornbostel, M.R. Geiker, Carbonation-induced corrosion: Investigation of the corrosion onset, Constr. Build. Mater. 162 (2018) 847–856. https://doi.org/10.1016/j.conbuildmat.2017.12.066.

[164] L.J. Parrott, D.C. Killoh, Carbonation in a 36 year old, in-situ concrete, Cem. Concr. Res. 19 (1989) 649–656. https://doi.org/10.1016/0008-8846(89)90017-3.

[165] R.M. Ghantous, R. François, S. Poyet, V. L'Hostis, F. Bernachy-Barbe, D. Meinel, L. Portier, N.-C. Tran, Relation between crack opening and extent of the damage induced at the steel/mortar interface, Constr. Build. Mater. 193 (2018) 97–104. https://doi.org/10.1016/j.conbuildmat.2018.10.176.

[166] A. Nasser, A. Clément, S. Laurens, A. Castel, Influence of steel–concrete interface condition on galvanic corrosion currents in carbonated concrete, Corros. Sci. 52 (2010) 2878–2890. https://doi.org/10.1016/j.corsci.2010.04.037.

[167] C.M. Hansson, A. Poursaee, A. Laurent, Macrocell and microcell corrosion of steel in ordinary Portland cement and high performance concretes, Cem. Concr. Res. 36 (2006) 2098–2102. https://doi.org/10.1016/j.cemconres.2006.07.005.

[168] A. Poursaee, C.M. Hansson, Potential pitfalls in assessing chloride-induced corrosion of steel in concrete, Cem. Concr. Res. 39 (2009) 391–400. https://doi.org/10.1016/j.cemconres.2009.01.015.

[169] A.B. Revert, K. Hornbostel, K. De Weerdt, M.R. Geiker, Macrocell corrosion in carbonated Portland and Portland-fly ash concrete - Contribution and mechanism, Cem. Concr. Res. 116 (2019) 273–283. https://doi.org/10.1016/j.cemconres.2018.12.005.

[170] M. Stefanoni, U. Angst, B. Elsener, Corrosion rate of carbon steel in carbonated concrete – A critical review, Cem. Concr. Res. 103 (2018) 35–48. https://doi.org/10.1016/j.cemconres.2017.10.007.

[171] P. Dangla, W. Dridi, Rebar corrosion in carbonated concrete exposed to variable humidity conditions. Interpretation of Tuutti's curve, Corros. Sci. 51 (2009) 1747–1756. https://doi.org/10.1016/j.corsci.2009.04.029.

[172] M. Stefanoni, U. Angst, B. Elsener, The mechanism controlling corrosion of steel in carbonated cementitious materials in wetting and drying exposure, Cem. Concr. Compos. 113 (2020) 103717. https://doi.org/10.1016/j.cemconcomp.2020.103717.

[173] M.U. Khan, S. Ahmad, H.J. Al-Gahtani, Chloride-induced corrosion of steel in concrete: An overview on chloride diffusion and prediction of corrosion initiation time, Int. J. Corros. 2017 (2017) 1–9. https://doi.org/10.1155/2017/5819202.

[174] M.. Pech-Canul, P. Castro, Corrosion measurements of steel reinforcement in concrete exposed to a tropical marine atmosphere, Cem. Concr. Res. 32 (2002) 491–498. https://doi.org/10.1016/S0008-8846(01)00713-X.

[175] M. Balonis, B. Lothenbach, G. Le Saout, F.P. Glasser, Impact of chloride on the mineralogy of hydrated Portland cement systems, Cem. Concr. Res. 40 (2010) 1009–1022. https://doi.org/10.1016/j.cemconres.2010.03.002.

[176] B. Guo, Y. Hong, G. Qiao, J. Ou, Z. Li, Thermodynamic modeling of the essential physicochemical interactions between the pore solution and the cement hydrates in chloride-contaminated cement-based materials, J. Colloid Interface Sci. 531 (2018) 56–63. https://doi.org/10.1016/j.jcis.2018.07.005.

[177] Y. Guo, T. Zhang, W. Tian, J. Wei, Q. Yu, Physically and chemically bound chlorides in hydrated cement pastes: a comparison study of the effects of silica fume and metakaolin, J. Mater. Sci. 54 (2019) 2152–2169. https://doi.org/10.1007/s10853-018-2953-5.

[178] P.T. Nguyen, O. Amiri, Study of the chloride transport in unsaturated concrete: Highlighting of electrical double layer, temperature and hysteresis effects, Constr. Build. Mater. 122 (2016) 284–293. https://doi.org/10.1016/j.conbuildmat.2016.05.154.

[179] Y. Zhang, M. Zhang, G. Ye, Influence of moisture condition on chloride diffusion in partially saturated ordinary Portland cement mortar, Mater. Struct. 51 (2018) 36. https://doi.org/10.1617/s11527-018-1162-7.

[180] S. Caré, Influence of aggregates on chloride diffusion coefficient into mortar, Cem. Concr. Res. 33 (2003) 1021–1028. https://doi.org/10.1016/S0008-8846(03)00009-7.

[181] P.P. Win, M. Watanabe, A. Machida, Penetration profile of chloride ion in cracked reinforced concrete, Cem. Concr. Res. 34 (2004) 1073–1079. https://doi.org/10.1016/j.cemconres.2003.11.020.

[182] A. Poursaee, C.M. Hansson, The influence of longitudinal cracks on the corrosion protection afforded reinforcing steel in high performance concrete, Cem. Concr. Res. 38 (2008) 1098–1105. https://doi.org/10.1016/j.cemconres.2008.03.018.

[183] J. Shi, J. Ming, Influence of defects at the steel-mortar interface on the corrosion behavior of steel, Constr. Build. Mater. 136 (2017) 118–125. https://doi.org/10.1016/j.conbuildmat.2017.01.007.

[184] F.U.A. Shaikh, Effect of cracking on corrosion of steel in concrete, Int. J. Concr. Struct. Mater. 12 (2018) 3. https://doi.org/10.1186/s40069-018-0234-y.

[185] E. Samson, J. Marchand, Modeling the transport of ions in unsaturated cement-based materials, Comput. Struct. 85 (2007) 1740–1756. https://doi.org/10.1016/j.compstruc.2007.04.008.

[186] V.Q. Tran, A. Soive, V. Baroghel-Bouny, Modelisation of chloride reactive transport in concrete including thermodynamic equilibrium, kinetic control and surface complexation, Cem. Concr.

Res. 110 (2018) 70–85. https://doi.org/10.1016/j.cemconres.2018.05.007.

[187] U.M. Angst, Predicting the time to corrosion initiation in reinforced concrete structures exposed to chlorides, Cem. Concr. Res. 115 (2019) 559–567. https://doi.org/10.1016/j.cemconres.2018.08.007.

[188] A. Covelo, B. Díaz, L. Freire, X.R. Nóvoa, M.C. Pérez, Microstructural changes in a cementitious membrane due to the application of a DC electric field, J. Environ. Sci. Heal. Part A. 43 (2008) 985–993. https://doi.org/10.1080/10934520801974632.

[189] M.A. Heine, D.S. Keir, M.J. Pryor, The specific effects of chloride and sulfate ions on oxide covered aluminum, J. Electrochem. Soc. 112 (1965) 24–32. https://doi.org/10.1149/1.2423459.

[190] D.D. Macdonald, The point defect model for the passive state, J. Electrochem. Soc. 139 (1992) 3434. https://doi.org/10.1149/1.2069096.

[191] P. Marcus, V. Maurice, H.-H. Strehblow, Localized corrosion (pitting): A model of passivity breakdown including the role of the oxide layer nanostructure, Corros. Sci. 50 (2008) 2698–2704. https://doi.org/10.1016/j.corsci.2008.06.047.

[192] P. Ghods, O. Burkan Isgor, F. Bensebaa, D. Kingston, Angle-resolved XPS study of carbon steel passivity and chloride-induced depassivation in simulated concrete pore solution, Corros. Sci. (2012). https://doi.org/10.1016/j.corsci.2012.01.019.

[193] P. Ghods, O. Burkan Isgor, G.J.C. Carpenter, J. Li, G.A. McRae, G.P. Gu, Nano-scale study of passive films and chloride-induced depassivation of carbon steel rebar in simulated concrete pore solutions using FIB/TEM, Cem. Concr. Res. 47 (2013) 55–68. https://doi.org/10.1016/j.cemconres.2013.01.009.

[194] H.B. Gunay, P. Ghods, O. Burkan Isgor, G.J.C. Carpenter, X. Wu, Characterization of atomic structure of oxide films on carbon steel in simulated concrete pore solutions using EELS, Appl. Surf. Sci. 274 (2013) 195–202. https://doi.org/10.1016/j.apsusc.2013.03.014.

[195] J. Xu, L. Jiang, Investigation on chloride threshold level for corrosion of reinforcing steel in the saturated Ca(OH)2 solution simulating the electrolytic environments of concrete, in: Adv. Civ. Eng. Mater. 50-Year Teach. Res. Anniv. Prof. Sun Wei, Nanjing, China, 2008: pp. 111–119.

[196] Q. Pang, H. DorMohammadi, O. Burkan Isgor, L. Árnadóttir, The effect of surface vacancies on the interactions of Cl with the α-Fe2O3 (0001) surface and the role of Cl in depassivation, Corros. Sci. (2019). https://doi.org/10.1016/j.corsci.2019.03.052.

[197] H. DorMohammadi, Q. Pang, P. Murkute, L. Árnadóttir, O.B. Isgor, Investigation of chloride-induced depassivation of iron in alkaline media by reactive force field molecular dynamics, Npj Mater. Degrad. 3 (2019) 19. https://doi.org/10.1038/s41529-019-0081-6.

[198] G.K. Glass, N.R. Buenfeld, The presentation of the chloride threshold level for corrosion of steel in concrete, Corros. Sci. 39 (1997) 1001–1013. https://doi.org/10.1016/S0010-938X(97)00009-7.

[199] U. Angst, B. Elsener, C.K. Larsen, Ø. Vennesland, Critical chloride content in reinforced concrete - A review, Cem. Concr. Res. 39 (2009) 1122–1138. https://doi.org/10.1016/j.cemconres.2009.08.006.

[200] B. Martín-Pérez, H. Zibara, R.D. Hooton, M.D.A. Thomas, A study of the effect of chloride binding on service life predictions, Cem. Concr. Res. 30 (2000) 1215–1223. https://doi.org/10.1016/S0008-8846(00)00339-2.

[201] M. Saillio, V. Baroghel-Bouny, F. Barberon, Chloride binding in sound and carbonated cementitious materials with various types of binder, Constr. Build. Mater. 68 (2014) 82–91. https://doi.org/10.1016/j.conbuildmat.2014.05.049.

[202] C. Alonso, C. Andrade, M. Castellote, P. Castro, Chloride threshold values to depassivate reinforcing bars embedded in a standardized OPC mortar, Cem. Concr. Res. 30 (2000) 1047–1055. https://doi.org/10.1016/S0008-8846(00)00265-9.

[203] U.M. Angst, B. Elsener, C.K. Larsen, Ø. Vennesland, Chloride induced reinforcement corrosion: Electrochemical monitoring of initiation stage and chloride threshold values, Corros. Sci. 53 (2011) 1451–1464. https://doi.org/10.1016/j.corsci.2011.01.025.

[204] N. Silva, Chloride Induced Corrosion of Reinforcement Steel in Concrete, Chalmers University of Technology, 2013.

[205] R.B. Figueira, A. Sadovski, A.P. Melo, E. V. Pereira, Chloride threshold value to initiate reinforcement corrosion in simulated concrete pore solutions: The influence of surface finishing and pH, Constr. Build. Mater. 141 (2017) 183–200. https://doi.org/10.1016/j.conbuildmat.2017.03.004.

[206] K.Y. Ann, H.-W. Song, Chloride threshold level for corrosion of steel in concrete, Corros. Sci. 49 (2007) 4113–4133. https://doi.org/10.1016/j.corsci.2007.05.007.

[207] Y. Cao, C. Gehlen, U. Angst, L. Wang, Z. Wang, Y. Yao, Critical chloride content in reinforced concrete — An updated review considering Chinese experience, Cem. Concr. Res. 117 (2019) 58–68. https://doi.org/10.1016/j.cemconres.2018.11.020.

[208] A. Kenny, A. Katz, Steel-concrete interface influence on chloride threshold for corrosion – Empirical reinforcement to theory, Constr. Build. Mater. 244 (2020) 118376. https://doi.org/10.1016/j.conbuildmat.2020.118376.

[209] U.M. Angst, B. Elsener, Chloride threshold values in concrete - A look back and ahead, Spec. Publ. 308 (2016) 1–12.

[210] C.L. Page, Initiation of chloride-induced corrosion of steel in concrete: role of the interfacial zone, Mater. Corros. 60 (2009) 586–592. https://doi.org/10.1002/maco.200905278.

[211] U.M. Angst, B. Elsener, The size effect in corrosion greatly influences the predicted life span of concrete infrastructures, Sci. Adv. 3 (2017) e1700751. https://doi.org/10.1126/sciadv.1700751.

[212] J.A. Gonzalez, A. Molina, E. Otero, W. López, On the mechanism of steel corrosion in concrete: the role of oxygen diffusion, Mag. Concr. Res. 42 (1990) 23–27. https://doi.org/10.1680/macr.1990.42.150.23.

[213] J.A. González, E. Otero, S. Feliu, W. López, Initial steps of corrosion in the steel/Ca(OH)2 + Cl– system: The role of heterogeneities on the steel surface and oxygen supply, Cem. Concr. Res. 23 (1993) 33–40. https://doi.org/10.1016/0008-8846(93)90132-S.

[214] T.D. Marcotte, Characterization of chloride-induced corrosion products that form in steel-reinforced cementitious materials, University of Waterloo, 2001.

[215] K.K. Sagoe-Crentsil, F.P. Glasser, “Green rust”, iron solubility and the role of chloride in the corrosion of steel at high pH, Cem. Concr. Res. 23 (1993) 785–791. https://doi.org/10.1016/0008-8846(93)90032-5.

[216] U. Angst, B. Elsener, C.K. Larsen, Ø. Vennesland, Chloride induced reinforcement corrosion: Rate limiting step of early pitting corrosion, Electrochim. Acta. 56 (2011) 5877–5889.

https://doi.org/10.1016/j.electacta.2011.04.124.

[217] M. Pourbaix, Applications of electrochemistry in corrosion science and in practice, Corros. Sci. 14 (1974) 25–82. https://doi.org/10.1016/S0010-938X(74)80006-5.

[218] U. Angst, B. Elsener, A. Jamali, B. Adey, Concrete cover cracking owing to reinforcement corrosion - theoretical considerations and practical experience, Mater. Corros. 63 (2012) 1069–1077. https://doi.org/10.1002/maco.201206669.

[219] J. Warkus, M. Raupach, Modelling of reinforcement corrosion - geometrical effects on macrocell corrosion, Mater. Corros. 61 (2009) 494–504. https://doi.org/10.1002/maco.200905437.

[220] J.A. González, C. Andrade, C. Alonso, S. Feliu, Comparison of rates of general corrosion and maximum pitting penetration on concrete embedded steel reinforcement, Cem. Concr. Res. 25 (1995) 257–264. https://doi.org/10.1016/0008-8846(95)00006-2.

[221] L. Yu, R. François, V.H. Dang, V. L'Hostis, R. Gagné, Distribution of corrosion and pitting factor of steel in corroded RC beams, Constr. Build. Mater. 95 (2015) 384–392. https://doi.org/10.1016/j.conbuildmat.2015.07.119.

[222] R. François, S. Laurens, F. Deby, Which parameter to quantify corrosion intensity?, in: Corros. Its Consequences Reinf. Concr. Struct., Elsevier, 2018: pp. 63–76. https://doi.org/10.1016/B978-1-78548-234-2.50003-2.

[223] C. Arya, P.R.. Vassie, Influence of cathode-to-anode area ratio and separation distance on galvanic corrosion currents of steel in concrete containing chlorides, Cem. Concr. Res. 25 (1995) 989–998. https://doi.org/10.1016/0008-8846(95)00094-S.

[224] C. Chalhoub, R. François, M. Carcasses, Effect of cathode–anode distance and electrical resistivity on macrocell corrosion currents and cathodic response in cases of chloride induced corrosion in reinforced concrete structures, Constr. Build. Mater. 245 (2020) 118337. https://doi.org/10.1016/j.conbuildmat.2020.118337.

[225] L. Bourreau, L. Gaillet, V. Bouteiller, F. Schoefs, B. Thauvin, J. Schneider, S. Naar, Spatial identification of exposure zones of concrete structures exposed to a marine environment with respect to reinforcement corrosion, Struct. Infrastruct. Eng. 16 (2020) 346–354. https://doi.org/10.1080/15732479.2019.1655072.

[226] S.J. Jaffer, C.M. Hansson, Chloride-induced corrosion products of steel in cracked-concrete subjected to different loading conditions, Cem. Concr. Res. 39 (2009) 116–125. https://doi.org/10.1016/j.cemconres.2008.11.001.

[227] R.M. Cornell, U. Schwertmann, The Iron Oxides: Structure, Properties, Reactions, Occurrences, and Uses, Wiley-VCH, 2003.

[228] J.A. González, J.M. Miranda, E. Otero, S. Feliu, Effect of electrochemically reactive rust layers on the corrosion of steel in a Ca(OH)2 solution, Corros. Sci. 49 (2007) 436–448. https://doi.org/10.1016/j.corsci.2006.04.014.

[229] M. Stefanoni, U. Angst, B. Elsener, Local electrochemistry of reinforcement steel – Distribution of open circuit and pitting potentials on steels with different surface condition, Corros. Sci. 98 (2015) 610–618. https://doi.org/10.1016/j.corsci.2015.06.004.

[230] Y. Ji, M. Wu, Z. Tan, F. Gao, F. Liu, Process control of reinforcement corrosion in concrete. Part 2: Time-dependent dominating factors under different environmental conditions, Constr. Build. Mater. 73 (2014) 214–221. https://doi.org/10.1016/j.conbuildmat.2014.09.103.

[231] Y. Ji, G. Zhan, Z. Tan, Y. Hu, F. Gao, Process control of reinforcement corrosion in concrete. Part 1: Effect of corrosion products, Constr. Build. Mater. 79 (2015) 214–222. https://doi.org/10.1016/j.conbuildmat.2014.12.083.

[232] E. Burger, J. Monnier, P. Berger, D. Neff, V. L'Hostis, S. Perrin, P. Dillmann, The long-term corrosion of mild steel in depassivated concrete: Localizing the oxygen reduction sites in corrosion products by isotopic tracer method, J. Mater. Res. 26 (2011) 3107–3115. https://doi.org/10.1557/jmr.2011.391.

[233] I. Azoulay, C. Rémazeilles, P. Refait, Corrosion of steel in carbonated media: The oxidation processes of chukanovite (Fe2(OH)2CO3), Corros. Sci. 85 (2014) 101–108. https://doi.org/10.1016/j.corsci.2014.04.004.

[234] A. Köliö, M. Honkanen, J. Lahdensivu, M. Vippola, M. Pentti, Corrosion products of carbonation induced corrosion in existing reinforced concrete facades, Cem. Concr. Res. 78 (2015) 200–207. https://doi.org/10.1016/j.cemconres.2015.07.009.

[235] J. Hadi, P. Wersin, V. Serneels, J.-M. Greneche, Eighteen years of steel–bentonite interaction in the FEBEX in situ test at the Grimsel Test Site in Switzerland, Clays Clay Miner. 67 (2019) 111–131. https://doi.org/10.1007/s42860-019-00012-5.

[236] K.K. Sagoe-Crentsil, F.P. Glasser, Constitution of green rust and its significance to the corrosion of steel in Portland cement, Corrosion. 49 (1993) 457–463. https://doi.org/10.5006/1.3316072.

[237] K. Suda, S. Misra, K. Motohashi, Corrosion products of reinforcing bars embedded in concrete, Corros. Sci. 35 (1993) 1543–1549. https://doi.org/10.1016/0010-938X(93)90382-Q.

[238] V. L'Hostis, E. Amblard, W. Guillot, C. Paris, L. Bellot-Gurlet, Characterisation of the steel concrete interface submitted to chloride-induced-corrosion, Mater. Corros. 64 (2013) 185–194. https://doi.org/10.1002/maco.201106488.

[239] J. Shi, J. Ming, Y. Zhang, J. Jiang, Corrosion products and corrosion-induced cracks of low-alloy steel and low-carbon steel in concrete, Cem. Concr. Compos. 88 (2018) 121–129. https://doi.org/10.1016/j.cemconcomp.2018.02.002.

[240] P. Refait, J.-M.R. Génin, The mechanisms of oxidation of ferrous hydroxychloride β-Fe2(OH)3Cl in aqueous solution: The formation of akaganeite vs goethite, Corros. Sci. 39 (1997) 539–553. https://doi.org/10.1016/S0010-938X(97)86102-1.

[241] C. Rémazeilles, P. Refait, On the formation of β-FeOOH (Akaganéite) in chloride-containing environments, Corros. Sci. 49 (2007) 844–857. https://doi.org/10.1016/j.corsci.2006.06.003.

[242] Y. Zhao, Y. Wu, W. Jin, Distribution of millscale on corroded steel bars and penetration of steel corrosion products in concrete, Corros. Sci. 66 (2013) 160–168. https://doi.org/10.1016/j.corsci.2012.09.014.

[243] K.K. Aligizaki, M.R. de Rooij, D.D. Macdonald, Analysis of iron oxides accumulating at the interface between aggregates and cement paste, Cem. Concr. Res. 30 (2000) 1941–1945. https://doi.org/10.1016/S0008-8846(00)00392-6.

[244] H.S. Wong, Y.X. Zhao, A.R. Karimi, N.R. Buenfeld, W.L. Jin, On the penetration of corrosion products from reinforcing steel into concrete due to chloride-induced corrosion, Corros. Sci. 52 (2010) 2469–2480. https://doi.org/10.1016/j.corsci.2010.03.025.

[245] T.D. Marcotte, C.M. Hansson, Corrosion products that form on steel within cement paste, Mater. Struct. 40 (2007) 325–340. https://doi.org/10.1617/s11527-006-9170-4.

[246] Y. Zhao, H. Ren, H. Dai, W. Jin, Composition and expansion coefficient of rust based on X-ray diffraction and thermal analysis, Corros. Sci. 53 (2011) 1646–1658. https://doi.org/10.1016/j.corsci.2011.01.007.

[247] G. Fang, W. Ding, Y. Liu, J. Zhang, F. Xing, B. Dong, Identification of corrosion products and 3D distribution in reinforced concrete using X-ray micro computed tomography, Constr. Build. Mater. 207 (2019) 304–315. https://doi.org/10.1016/j.conbuildmat.2019.02.133.

[248] C. Lu, W. Jin, R. Liu, Reinforcement corrosion-induced cover cracking and its time prediction for reinforced concrete structures, Corros. Sci. 53 (2011) 1337–1347. https://doi.org/10.1016/j.corsci.2010.12.026.

[249] B. Sanz, J. Planas, J.M. Sancho, A closer look to the mechanical behavior of the oxide layer in concrete reinforcement corrosion, Int. J. Solids Struct. 62 (2015) 256–268. https://doi.org/10.1016/j.ijsolstr.2015.02.040.

[250] Y. Liu, R.E. Weyers, Modeling the time-to-corrosion cracking in chloride contaminated reinforced concrete structures, ACI Mater. J. 95 (1998) 675–680. https://doi.org/10.14359/410.

[251] A. Poursaee, Temperature dependence of the formation of the passivation layer on carbon steel in high alkaline environment of concrete pore solution, Electrochem. Commun. 73 (2016) 24–28. https://doi.org/10.1016/j.elecom.2016.10.003.

[252] B. Díaz, B. Guitián, X.R. Nóvoa, M.C. Pérez, The effect of long-term atmospheric aging and temperature on the electrochemical behaviour of steel rebars in mortar, Corros. Sci. 140 (2018) 143–150. https://doi.org/10.1016/j.corsci.2018.06.007.

[253] J.M. Deus, L. Freire, M.F. Montemor, X.R. Nóvoa, The corrosion potential of stainless steel rebars in concrete: Temperature effect, Corros. Sci. 65 (2012) 556–560. https://doi.org/10.1016/j.corsci.2012.09.001.

[254] A. Česen, T. Kosec, A. Legat, Characterization of steel corrosion in mortar by various electrochemical and physical techniques, Corros. Sci. 75 (2013) 47–57. https://doi.org/10.1016/j.corsci.2013.05.015.

[255] B. Šavija, M. Luković, S.A.S. Hosseini, J. Pacheco, E. Schlangen, Corrosion induced cover cracking studied by X-ray computed tomography, nanoindentation, and energy dispersive X-ray spectrometry (EDS), Mater. Struct. 48 (2015) 2043–2062. https://doi.org/10.1617/s11527-014-0292-9.

[256] B. Dong, G. Fang, Y. Liu, P. Dong, J. Zhang, F. Xing, S. Hong, Monitoring reinforcement corrosion and corrosion-induced cracking by X-ray microcomputed tomography method, Cem. Concr. Res. 100 (2017) 311–321. https://doi.org/10.1016/j.cemconres.2017.07.009.

[257] G. Fang, Y. Liu, S. Qin, W. Ding, J. Zhang, S. Hong, F. Xing, B. Dong, Visualized tracing of crack self-healing features in cement/microcapsule system with X-ray microcomputed tomography, Constr. Build. Mater. 179 (2018) 336–347. https://doi.org/10.1016/j.conbuildmat.2018.05.193.

[258] B. Dong, G. Shi, P. Dong, W. Ding, X. Teng, S. Qin, Y. Liu, F. Xing, S. Hong, Visualized tracing of rebar corrosion evolution in concrete with X-ray micro-computed tomography method, Cem. Concr. Compos. 92 (2018) 102–109. https://doi.org/10.1016/j.cemconcomp.2018.06.003.

[259] W.-J. Chitty, P. Dillmann, V. L'Hostis, C. Lombard, Long-term corrosion resistance of metallic reinforcements in concrete—a study of corrosion mechanisms based on archaeological artefacts, Corros. Sci. 47 (2005) 1555–1581. https://doi.org/10.1016/j.corsci.2004.07.032.

[260] V. L'Hostis, D. Neff, L. Bellot-Gurlet, P. Dillmann, Characterization of long-term corrosion of rebars embedded in concretes sampled on French historical buildings aged from 50 to 80 years, Mater. Corros. 60 (2009) 93–98. https://doi.org/10.1002/maco.200805019.

[261] Y. Zhao, H. Ding, W. Jin, Development of the corrosion-filled paste and corrosion layer at the steel/concrete interface, Corros. Sci. 87 (2014) 199–210. https://doi.org/10.1016/j.corsci.2014.06.032.

[262] Y. Zhao, X. Zhang, W. Jin, Influence of environment on the development of corrosion product-filled paste and a corrosion layer at the steel/concrete interface, Corros. Sci. 124 (2017) 1–9. https://doi.org/10.1016/j.corsci.2017.03.026.

[263] Y. Zhao, B. Hu, J. Yu, W. Jin, Non-uniform distribution of rust layer around steel bar in concrete, Corros. Sci. 53 (2011) 4300–4308. https://doi.org/10.1016/j.corsci.2011.08.045.

[264] C. Cao, M.M.S. Cheung, Non-uniform rust expansion for chloride-induced pitting corrosion in RC structures, Constr. Build. Mater. (2014). https://doi.org/10.1016/j.conbuildmat.2013.10.042.

[265] Y. Zhao, J. Dong, Y. Wu, W. Jin, Corrosion-induced concrete cracking model considering corrosion product-filled paste at the concrete/steel interface, Constr. Build. Mater. 116 (2016) 273–280. https://doi.org/10.1016/j.conbuildmat.2016.04.097.

[266] X. Xi, S. Yang, C.-Q. Li, A non-uniform corrosion model and meso-scale fracture modelling of concrete, Cem. Concr. Res. 108 (2018) 87–102. https://doi.org/10.1016/j.cemconres.2018.03.009.

[267] A. Jamali, U. Angst, B. Adey, B. Elsener, Modeling of corrosion-induced concrete cover cracking: A critical analysis, Constr. Build. Mater. 42 (2013) 225–237. https://doi.org/10.1016/j.conbuildmat.2013.01.019.

[268] C. Andrade, I. Martínez, Techniques for measuring the corrosion rate (polarization resistance) and the corrosion potential of reinforced concrete structures, Non-Destructive Eval. Reinf. Concr. Struct. (2010) 284–316. https://doi.org/10.1533/9781845699604.2.284.

[269] R. Francois, G. Arliguie, D. Bardy, Electrode potential measurements of concrete reinforcement for corrosion evaluation, Cem. Concr. Res. 24 (1994) 401–412. https://doi.org/10.1016/0008-8846(94)90127-9.

[270] K. Reichling, M. Raupach, Method to determine electrochemical potential gradients without reinforcement connection in concrete structures, Cem. Concr. Compos. 47 (2014) 3–8. https://doi.org/10.1016/j.cemconcomp.2013.12.007.

[271] S. Garcia, F. Deby, Numerical and experimental development of gradient potential measurement for corrosion detection of reinforced concrete slab, in: Serv. Life Durab. Reinf. Concr. Struct., Cefracor, 2019: pp. 71–86. https://doi.org/10.1007/978-3-319-90236-4_6.

[272] M. Pour-Ghaz, O.B. Isgor, P. Ghods, Quantitative interpretation of half-cell potential measurements in concrete structures, J. Mater. Civ. Eng. 21 (2009) 467–475. https://doi.org/10.1061/(ASCE)0899-1561(2009)21:9(467).

[273] S.K. Verma, S.S. Bhadauria, S. Akhtar, Monitoring corrosion of steel bars in reinforced concrete structures, Sci. World J. 2014 (2014) 957904. https://doi.org/10.1155/2014/957904.

[274] U. Angst, Ø. Vennesland, R. Myrdal, Diffusion potentials as source of error in electrochemical measurements in concrete, Mater. Struct. 42 (2009) 365–375. https://doi.org/10.1617/s11527-008-9387-5.

[275] P. Castro, A.A. Sagüés, E.I. Moreno, L. Maldonado, J. Genescá, Characterization of activated titanium solid reference electrodes for corrosion testing of steel in concrete, Corrosion. 52 (1996) 609–617. https://doi.org/10.5006/1.3292151.

[276] G.S. Duffó, S.B. Farina, Development of an embeddable sensor to monitor the corrosion process of new and existing reinforced concrete structures, Constr. Build. Mater. 23 (2009) 2746–2751. https://doi.org/10.1016/j.conbuildmat.2009.04.001.

[277] S.P. Karthick, S. Muralidharan, V. Saraswathy, K. Thangavel, Long-term relative performance of embedded sensor and surface mounted electrode for corrosion monitoring of steel in concrete structures, Sensors Actuators B Chem. 192 (2014) 303–309. https://doi.org/10.1016/j.snb.2013.10.123.

[278] M. Jin, Y. Jiang, L. Jiang, H. Chu, F. Zhi, S. Gao, Fabrication and characterization of pseudo reference electrode based on graphene-cement composites for corrosion monitoring in reinforced concrete structure, Constr. Build. Mater. 204 (2019) 144–157. https://doi.org/10.1016/j.conbuildmat.2019.01.169.

[279] A. Sassolini, N. Colozza, E. Papa, K. Hermansson, I. Cacciotti, F. Arduini, Screen-printed electrode as a cost-effective and miniaturized analytical tool for corrosion monitoring of reinforced concrete, Electrochem. Commun. 98 (2019) 69–72. https://doi.org/10.1016/j.elecom.2018.11.023.

[280] Ø. Vennesland, M. Raupach, C. Andrade, Recommendation of Rilem TC 154-EMC: "Electrochemical techniques for measuring corrosion in concrete"—measurements with embedded probes, Mater. Struct. 40 (2007) 745–758. https://doi.org/10.1617/s11527-006-9219-4.

[281] A. Leibbrandt, B. Elsener, C. Hürzeler, G. Caprati, R. Flatt, R. Siegwart, Climbing robot for corrosion monitoring and sensor for potential mapping, WO2013156142A1, 2013. https://doi.org/10.2749/2221378027963366.

[282] B. Elsener, C. Andrade, J. Gulikers, R. Polder, M. Raupach, Half-cell potential measurements - Potential mapping on reinforced concrete structures, Mater. Struct. 36 (2003) 461–671. https://doi.org/10.1007/BF02481526.

[283] ASTM_C876-09, Standard test method for corrosion potentials of uncoated reinforcing steel in concrete (2009), (n.d.). https://www.astm.org/Standards/C876.htm.

[284] K. Reichling, M. Raupach, J. Broomfield, J. Gulikers, V. L'Hostis, S. Kessler, K. Osterminski, I. Pepenar, U. Schneck, G. Sergi, G. Taché, Full surface inspection methods regarding reinforcement corrosion of concrete structures, Mater. Corros. 64 (2013) 116–127. https://doi.org/10.1002/maco.201206625.

[285] E. Sassine, S. Laurens, R. François, E. Ringot, A critical discussion on rebar electrical continuity and usual interpretation thresholds in the field of half-cell potential measurements in steel reinforced concrete, Mater. Struct. 51 (2018) 93. https://doi.org/10.1617/s11527-018-1221-0.

[286] G.Y. Koga, B. Albert, R.P. Nogueira, Revisiting the ASTM C876 standard for corrosion of reinforcing steel: On the correlation between corrosion potential and polarization resistance during the curing of different cement mortars, Electrochem. Commun. 94 (2018) 1–4. https://doi.org/10.1016/j.elecom.2018.07.017.

[287] P. Gu, J.J. Beaudoin, Obtaining Effective Half-Cell Potential Measurements in Reinforced Concrete Structures, National R, 1998.

[288] W. Yodsudjai, T. Pattarakittam, Factors influencing half-cell potential measurement and its

relationship with corrosion level, Measurement. 104 (2017) 159–168. https://doi.org/10.1016/j.measurement.2017.03.027.

[289] J.-F. Lataste, G. Villain, Electrical Methods, in: Non-Destructive Test. Eval. Civ. Eng. Struct., Elsevier, 2018: pp. 139–172. https://doi.org/10.1016/B978-1-78548-229-8.50004-2.

[290] R.B. Polder, Test methods for on site measurement of resistivity of concrete — a RILEM TC-154 technical recommendation, Constr. Build. Mater. 15 (2001) 125–131. https://doi.org/10.1016/S0950-0618(00)00061-1.

[291] P. Azarsa, R. Gupta, Electrical resistivity of concrete for durability evaluation: A review, Adv. Mater. Sci. Eng. 2017 (2017) 1–30. https://doi.org/10.1155/2017/8453095.

[292] F. Presuel-Moreno, Y.-Y. Wu, Y. Liu, Effect of curing regime on concrete resistivity and aging factor over time, Constr. Build. Mater. 48 (2013) 874–882. https://doi.org/10.1016/j.conbuildmat.2013.07.094.

[293] R. du Plooy, S. Palma Lopes, G. Villain, X. Dérobert, Development of a multi-ring resistivity cell and multi-electrode resistivity probe for investigation of cover concrete condition, NDT E Int. 54 (2013) 27–36. https://doi.org/10.1016/j.ndteint.2012.11.007.

[294] R. Spragg, C. Qiao, T. Barrett, J. Weiss, Assessing a concrete’s resistance to chloride ion ingress using the formation factor, Corros. Steel Concr. Struct. (2016) 211–238. https://doi.org/10.1016/B978-1-78242-381-2.00011-0.

[295] A.J. Garzon, J. Sanchez, C. Andrade, N. Rebolledo, E. Menéndez, J. Fullea, Modification of four point method to measure the concrete electrical resistivity in presence of reinforcing bars, Cem. Concr. Compos. 53 (2014) 249–257. https://doi.org/10.1016/j.cemconcomp.2014.07.013.

[296] R. Polder, C. Andrade, B. Elsener, Ø. Vennesland, J. Gulikers, R. Weidert, M. Raupach, Test methods for on site measurement of resistivity of concrete, Mater. Struct. 33 (2000) 603–611. https://doi.org/10.1007/BF02480599.

[297] H. Layssi, P. Ghods, A.R. Alizadeh, M. Salehi, Electrical resistivity of concrete: Concepts, applications, and measurement techniques, Concr. Int. (2015) 41–46.

[298] W.J. Weiss, R.P. Spragg, O.B. Isgor, M.T. Ley, T. Van Dam, Toward performance specifications for concrete: Linking resistivity, RCPT and diffusion predictions using the formation factor for use in specifications, in: High Tech Concr. Where Technol. Eng. Meet, Springer International Publishing, Cham, 2018: pp. 2057–2065. https://doi.org/10.1007/978-3-319-59471-2_235.

[299] W.J. Weiss, T.J. Barrett, C. Qiao, H. Todak, Toward a specification for transport properties of concrete based on the formation factor of a sealed specimen, Adv. Civ. Eng. Mater. 5 (2016) 20160004. https://doi.org/10.1520/ACEM20160004.

[300] R. He, H. Ma, R.B. Hafiz, C. Fu, X. Jin, J. He, Determining porosity and pore network connectivity of cement-based materials by a modified non-contact electrical resistivity measurement: Experiment and theory, Mater. Des. 156 (2018) 82–92. https://doi.org/10.1016/j.matdes.2018.06.045.

[301] H. Sallehi, P. Ghods, O.B. Isgor, Formation factor of fresh cementitious pastes, Cem. Concr. Compos. 91 (2018) 174–188. https://doi.org/10.1016/j.cemconcomp.2018.05.011.

[302] X. Lu, Application of the Nernst-Einstein equation to concrete, Cem. Concr. Res. 27 (1997) 293–302. https://doi.org/10.1016/S0008-8846(96)00200-1.

[303] K.A. Snyder, The relationship between the formation factor and the diffusion coefficient of

porous materials saturated with concentrated electrolytes: theoretical and experimental considerations, Concr. Sci. Eng. 3 (2001).

[304] K.A. Snyder, X. Feng, B.D. Keen, T.O. Mason, Estimating the electrical conductivity of cement paste pore solutions from OH−, K+ and Na+ concentrations, Cem. Concr. Res. 33 (2003) 793–798. https://doi.org/10.1016/S0008-8846(02)01068-2.

[305] D.P. Bentz, A virtual rapid chloride permeability test, Cem. Concr. Compos. 29 (2007) 723–731. https://doi.org/10.1016/j.cemconcomp.2007.06.006.

[306] M. Tsui Chang, P. Suraneni, O.B. Isgor, D. Trejo, W.J. Weiss, Using X-ray fluorescence to assess the chemical composition and resistivity of simulated cementitious pore solutions, Int. J. Adv. Eng. Sci. Appl. Math. 9 (2017) 136–143. https://doi.org/10.1007/s12572-017-0181-x.

[307] Y. Bu, D. Luo, J. Weiss, Using Fick’s second law and Nernst–Planck approach in prediction of chloride ingress in concrete materials, Adv. Civ. Eng. Mater. 3 (2014) 20140018. https://doi.org/10.1520/ACEM20140018.

[308] C.A.J. Appelo, Solute transport solved with the Nernst-Planck equation for concrete pores with ‘free’ water and a double layer, Cem. Concr. Res. 101 (2017) 102–113. https://doi.org/10.1016/j.cemconres.2017.08.030.

[309] C. Qiao, A.T. Coyle, O.B. Isgor, W.J. Weiss, Prediction of chloride ingress in saturated concrete using formation factor and chloride binding isotherm, Adv. Civ. Eng. Mater. 7 (2018) 20170141. https://doi.org/10.1520/ACEM20170141.

[310] V. Jafari Azad, A.R. Erbektas, C. Qiao, O.B. Isgor, W.J. Weiss, Relating the formation factor and chloride binding parameters to the apparent chloride diffusion coefficient of concrete, J. Mater. Civ. Eng. 31 (2019) 04018392. https://doi.org/10.1061/(ASCE)MT.1943-5533.0002615.

[311] O. Sengul, Use of electrical resistivity as an indicator for durability, Constr. Build. Mater. 73 (2014) 434–441. https://doi.org/10.1016/j.conbuildmat.2014.09.077.

[312] M.K. Moradllo, C. Qiao, B. Isgor, S. Reese, W.J. Weiss, Relating formation factor of concrete to water absorption, ACI Mater. J. 115 (2018) 887–898. https://doi.org/10.14359/51706844.

[313] O.B. Isgor, W.J. Weiss, A nearly self-sufficient framework for modelling reactive-transport processes in concrete, Mater. Struct. 52 (2019) 3. https://doi.org/10.1617/s11527-018-1305-x.

[314] R. Spragg, C. Villani, K. Snyder, D. Bentz, J.W. Bullard, J. Weiss, Factors that influence electrical resistivity measurements in cementitious systems, Transp. Res. Rec. J. Transp. Res. Board. 2342 (2013) 90–98. https://doi.org/10.3141/2342-11.

[315] Y. Wang, Y. Xi, The effect of temperature on moisture transport in concrete, Materials (Basel). 10 (2017) 926. https://doi.org/10.3390/ma10080926.

[316] A. Aït-Mokhtar, R. Belarbi, F. Benboudjema, N. Burlion, B. Capra, M. Carcassès, J.B. Colliat, F. Cussigh, F. Deby, F. Jacquemot, T. De Larrard, J.F. Lataste, P. Le Bescop, M. Pierre, S. Poyet, P. Rougeau, T. Rougelot, A. Sellier, J. Séménadisse, J.M. Torrenti, A. Trabelsi, P. Turcry, H. Yanez-Godoy, Experimental investigation of the variability of concrete durability properties, Cem. Concr. Res. 45 (2013) 21–36. https://doi.org/10.1016/j.cemconres.2012.11.002.

[317] B. Lothenbach, F. Winnefeld, C. Alder, E. Wieland, P. Lunk, Effect of temperature on the pore solution, microstructure and hydration products of Portland cement pastes, Cem. Concr. Res. 37 (2007) 483–491. https://doi.org/10.1016/j.cemconres.2006.11.016.

[318] Y. Liu, F.J. Presuel-Moreno, Normalization of temperature effect on concrete resistivity by

method using Arrhenius law, ACI Mater. J. 111 (2014) 433–442. https://doi.org/10.14359/51686725.

[319] P.A. Claisse, H.I. El-Sayad, I.G. Shaaban, Permeability and pore volume of carbonated concrete, ACI Mater. J. 96 (1999) 378–381. https://doi.org/10.14359/636.

[320] U.M. Angst, B. Elsener, On the applicability of Wenner method for resistivity measurements of concrete, ACI Mater. J. 111 (2014) 661–672. https://doi.org/10.14359/51686831.

[321] C.-T. Chen, J.-J. Chang, W. Yeih, The effects of specimen parameters on the resistivity of concrete, Constr. Build. Mater. 71 (2014) 35–43. https://doi.org/10.1016/j.conbuildmat.2014.08.009.

[322] M. Salehi, P. Ghods, O.B. Isgor, Numerical study on the effect of cracking on surface resistivity of plain and reinforced concrete elements, J. Mater. Civ. Eng. 27 (2015) 04015053. https://doi.org/10.1061/(ASCE)MT.1943-5533.0001328.

[323] Ł. Sadowski, New non-destructive method for linear polarisation resistance corrosion rate measurement, Arch. Civ. Mech. Eng. 10 (2010) 109–116. https://doi.org/10.1016/S1644-9665(12)60053-3.

[324] A.Q. Nguyen, G. Klysz, F. Deby, J.-P. Balayssac, Evaluation of water content gradient using a new configuration of linear array four-point probe for electrical resistivity measurement, Cem. Concr. Compos. 83 (2017) 308–322. https://doi.org/10.1016/j.cemconcomp.2017.07.020.

[325] S.G. Millard, Reinforced concrete resistivity measurement techniques, Proc. Inst. Civ. Eng. 91 (1991) 71–88. https://doi.org/10.1680/iicep.1991.13583.

[326] K.R. Gowers, S.G. Millard, Measurement of concrete resistivity for assessment of corrosion severity of steel using Wenner technique, ACI Mater. J. 96 (1999) 536–541. https://doi.org/10.14359/655.

[327] O. Sengul, O.E. Gjorv, Effect of embedded steel on electrical resistivity measurements on concrete structures, ACI Mater. J. 106 (2009) 11–18. https://doi.org/10.14359/56311.

[328] F. Presuel-Moreno, Y. Liu, Y.-Y. Wu, Numerical modeling of the effects of rebar presence and/or multilayered concrete resistivity on the apparent resistivity measured via the Wenner method, Constr. Build. Mater. 48 (2013) 16–25. https://doi.org/10.1016/j.conbuildmat.2013.06.053.

[329] M. Salehi, P. Ghods, O. Burkan Isgor, Numerical investigation of the role of embedded reinforcement mesh on electrical resistivity measurements of concrete using the Wenner probe technique, Mater. Struct. 49 (2016) 301–316. https://doi.org/10.1617/s11527-014-0498-x.

[330] W. Morris, E.I. Moreno, A.A. Sagüés, Practical evaluation of resistivity of concrete in test cylinders using a Wenner array probe, Cem. Concr. Res. 26 (1996) 1779–1787. https://doi.org/10.1016/S0008-8846(96)00175-5.

[331] O. Sengul, O.E. Gjorv, Electrical resistivity measurements for quality control during concrete construction, ACI Mater. J. 105 (2008) 541–547. https://doi.org/10.14359/20195.

[332] P. Ghosh, Q. Tran, Influence of parameters on surface resistivity of concrete, Cem. Concr. Compos. 62 (2015) 134–145. https://doi.org/10.1016/j.cemconcomp.2015.06.003.

[333] J. Sanchez, C. Andrade, J. Torres, N. Rebolledo, J. Fullea, Determination of reinforced concrete durability with on-site resistivity measurements, Mater. Struct. 50 (2017) 41. https://doi.org/10.1617/s11527-016-0884-7.

[334] K. Hornbostel, C.K. Larsen, M.R. Geiker, Relationship between concrete resistivity and corrosion rate – A literature review, Cem. Concr. Compos. 39 (2013) 60–72. https://doi.org/10.1016/j.cemconcomp.2013.03.019.

[335] C. Alonso, C. Andrade, J.A. González, Relation between resistivity and corrosion rate of reinforcements in carbonated mortar made with several cement types, Cem. Concr. Res. 18 (1988) 687–698. https://doi.org/10.1016/0008-8846(88)90091-9.

[336] S. Feliu, J.A. González, S. Feliu, C. Andrade, Relationship between conductivity of concrete and corrosion of reinforcing bars, Br. Corros. J. 24 (1989) 195–198. https://doi.org/10.1179/000705989798270027.

[337] B. Yu, J. Liu, Z. Chen, Probabilistic evaluation method for corrosion risk of steel reinforcement based on concrete resistivity, Constr. Build. Mater. 138 (2017) 101–113. https://doi.org/10.1016/j.conbuildmat.2017.01.100.

[338] R.B. Figueira, Electrochemical sensors for monitoring the corrosion conditions of reinforced concrete structures: A review, Appl. Sci. 7 (2017) 1157. https://doi.org/10.3390/app7111157.

[339] W. Morris, A. Vico, M. Vazquez, S.R. de Sanchez, Corrosion of reinforcing steel evaluated by means of concrete resistivity measurements, Corros. Sci. 44 (2002) 81–99. https://doi.org/10.1016/S0010-938X(01)00033-6.

[340] J. Gulikers, Theoretical considerations on the supposed linear relationship between concrete resistivity and corrosion rate of steel reinforcement, Mater. Corros. 56 (2005) 393–403. https://doi.org/10.1002/maco.200403841.

[341] S. Ahmad, An experimental study on correlation between concrete resistivity and reinforcement corrosion rate, Anti-Corrosion Methods Mater. 61 (2014) 158–165. https://doi.org/10.1108/ACMM-07-2013-1285.

[342] F. Akgul, Inspection and evaluation of a network of concrete bridges based on multiple NDT techniques, Struct. Infrastruct. Eng. (2020) 1–20. https://doi.org/10.1080/15732479.2020.1790016.

[343] K. Hornbostel, B. Elsener, U.M. Angst, C.K. Larsen, M.R. Geiker, Limitations of the use of concrete bulk resistivity as an indicator for the rate of chloride-induced macro-cell corrosion, Struct. Concr. 18 (2017) 326–333. https://doi.org/10.1002/suco.201500141.

[344] K. Hornbostel, U.M. Angst, B. Elsener, C.K. Larsen, M.R. Geiker, On the limitations of predicting the ohmic resistance in a macro-cell in mortar from bulk resistivity measurements, Cem. Concr. Res. 76 (2015) 147–158. https://doi.org/10.1016/j.cemconres.2015.05.023.

[345] K. Hornbostel, U.M. Angst, B. Elsener, C.K. Larsen, M.R. Geiker, Influence of mortar resistivity on the rate-limiting step of chloride-induced macro-cell corrosion of reinforcing steel, Corros. Sci. 110 (2016) 46–56. https://doi.org/10.1016/j.corsci.2016.04.011.

[346] A.T. Coyle, R.P. Spragg, P. Suraneni, A.N. Amirkhanian, W.J. Weiss, Comparison of linear temperature corrections and activation energy temperature corrections for electrical resistivity measurements of concrete, Adv. Civ. Eng. Mater. 7 (2018) 20170135. https://doi.org/10.1520/ACEM20170135.

[347] J.M. Deus, B. Díaz, L. Freire, X.R. Nóvoa, The electrochemical behaviour of steel rebars in concrete: an electrochemical impedance spectroscopy study of the effect of temperature, Electrochim. Acta. 131 (2014) 106–115. https://doi.org/10.1016/j.electacta.2013.12.012.

[348] K. Reichling, M. Raupach, N. Klitzsch, Determination of the distribution of electrical resistivity

in reinforced concrete structures using electrical resistivity tomography, Mater. Corros. 66 (2015) 763–771. https://doi.org/10.1002/maco.201407763.

[349] K. Karhunen, A. Seppänen, A. Lehikoinen, P.J.M. Monteiro, J.P. Kaipio, Electrical resistance tomography imaging of concrete, Cem. Concr. Res. 40 (2010) 137–145. https://doi.org/10.1016/j.cemconres.2009.08.023.

[350] M.H. Loke, Tutorial: 2-D and 3-D electrical imaging surveys, 2004. www.geoelectrical.com (accessed July 13, 2018).

[351] D. Smyl, Electrical tomography for characterizing transport properties in cement-based materials: A review, Constr. Build. Mater. 244 (2020) 118299. https://doi.org/10.1016/j.conbuildmat.2020.118299.

[352] M.A. Alhajj, S. Palma-Lopes, G. Villain, Accounting for steel rebar effect on resistivity profiles in view of reinforced concrete structure survey, Constr. Build. Mater. 223 (2019) 898–909. https://doi.org/10.1016/j.conbuildmat.2019.07.208.

[353] J. Priou, Y. Lecieux, M. Chevreuil, V. Gaillard, C. Lupi, D. Leduc, E. Rozière, R. Guyard, F. Schoefs, In situ DC electrical resistivity mapping performed in a reinforced concrete wharf using embedded sensors, Constr. Build. Mater. 211 (2019) 244–260. https://doi.org/10.1016/j.conbuildmat.2019.03.152.

[354] J. Badr, Y. Fargier, S. Palma-Lopes, F. Deby, J.-P. Balayssac, S. Delepine-Lesoille, L.-M. Cottineau, G. Villain, Design and validation of a multi-electrode embedded sensor to monitor resistivity profiles over depth in concrete, Constr. Build. Mater. 223 (2019) 310–321. https://doi.org/10.1016/j.conbuildmat.2019.06.226.

[355] M. Fares, G. Villain, S. Bonnet, S. Palma Lopes, B. Thauvin, M. Thiery, Determining chloride content profiles in concrete using an electrical resistivity tomography device, Cem. Concr. Compos. 94 (2018) 315–326. https://doi.org/10.1016/j.cemconcomp.2018.08.001.

[356] S. Bonnet, J.-P. Balayssac, Combination of the Wenner resistivimeter and Torrent permeameter methods for assessing carbonation depth and saturation level of concrete, Constr. Build. Mater. 188 (2018) 1149–1165. https://doi.org/10.1016/j.conbuildmat.2018.07.151.

[357] D. Smyl, M. Hallaji, A. Seppänen, M. Pour-Ghaz, Three-dimensional electrical impedance tomography to monitor unsaturated moisture ingress in cement-based materials, Transp. Porous Media. 115 (2016) 101–124. https://doi.org/10.1007/s11242-016-0756-1.

[358] D. Smyl, R. Rashetnia, A. Seppänen, M. Pour-Ghaz, Can electrical resistance tomography be used for imaging unsaturated moisture flow in cement-based materials with discrete cracks?, Cem. Concr. Res. 91 (2017) 61–72. https://doi.org/10.1016/j.cemconres.2016.10.009.

[359] E. V. Pereira, M.M. Salta, I.T.E. Fonseca, On the measurement of the polarisation resistance of reinforcing steel with embedded sensors: A comparative study, Mater. Corros. 66 (2015) 1029–1038. https://doi.org/10.1002/maco.201407910.

[360] C. Andrade, L. Soler, C. Alonso, X.R. Nóvoa, M. Keddam, The importance of geometrical considerations in the measurement of steel corrosion in concrete by means of AC impedance, Corros. Sci. 37 (1995) 2013–2023. https://doi.org/10.1016/0010-938X(95)00095-2.

[361] S. Rengaraju, L. Neelakantan, R.G. Pillai, Investigation on the polarization resistance of steel embedded in highly resistive cementitious systems – An attempt and challenges, Electrochim. Acta. 308 (2019) 131–141. https://doi.org/10.1016/j.electacta.2019.03.200.

[362] O.B. Isgor, U. Angst, M. Geiker, C. Halmen, C. Hansson, J. Pacheco, D. Tepke, D. Trejo, P. Vaddey, Recommended practice for reporting experimental data produced from studies on corrosion of steel in cementitious systems, RILEM Tech. Lett. 4 (2019) 22–32. https://doi.org/10.21809/rilemtechlett.2019.90.

[363] M. Stern, A.L. Geary, Electrochemical polarization, J. Electrochem. Soc. 104 (1957) 56. https://doi.org/10.1149/1.2428496.

[364] A. Guyader, F. Huet, R.P. Nogueira, Polarization resistance measurements: Potentiostatically or galvanostatically?, Corrosion. 65 (2009) 136–144. https://doi.org/10.5006/1.3319118.

[365] S. Ahmad, B. Bhattacharjee, A simple arrangement and procedure for in-situ measurement of corrosion rate of rebar embedded in concrete, Corros. Sci. 37 (1995) 781–791. https://doi.org/10.1016/0010-938X(95)80008-5.

[366] A. Fahim, P. Ghods, O.B. Isgor, M.D.A. Thomas, A critical examination of corrosion rate measurement techniques applied to reinforcing steel in concrete, Mater. Corros. 69 (2018) 1784–1799. https://doi.org/10.1002/maco.201810263.

[367] A.A. Sagüés, S.C. Kranc, E.I. Moreno, The time-domain response of a corroding system with constant phase angle interfacial component: Application to steel in concrete, Corros. Sci. 37 (1995) 1097–1113. https://doi.org/10.1016/0010-938X(95)00017-E.

[368] C.J. Newton, J.M. Sykes, A galvanostatic pulse technique for investigation of steel corrosion in concrete, Corros. Sci. 28 (1988) 1051–1074. https://doi.org/10.1016/0010-938X(88)90101-1.

[369] B. Elsener, O. Klinghoffer, T. Frolund, E. Rislund, Y. Schiegg, H. Böhni, Assessment of reinforcement corrosion by means of galvanostatic pulse technique, in: Repair Concr. Struct., Svolvær, Norway, 1997: pp. 391–400.

[370] A. Poursaee, Potentiostatic transient technique, a simple approach to estimate the corrosion current density and Stern–Geary constant of reinforcing steel in concrete, Cem. Concr. Res. 40 (2010) 1451–1458. https://doi.org/10.1016/j.cemconres.2010.04.006.

[371] J.E. Ramón, J.M. Gandía-Romero, R. Bataller, M. Alcañiz, M. Valcuende, J. Soto, Potential step voltammetry: an approach for corrosion rate measurement of reinforcements in concrete, Cem. Concr. Compos. (2020) 103590. https://doi.org/10.1016/j.cemconcomp.2020.103590.

[372] D.M. Bastidas, J.A. González, S. Feliu, A. Cobo, J.M. Miranda, A quantitative study of concrete-embedded steel corrosion using potentiostatic pulses, Corrosion. 63 (2007) 1094–1100. https://doi.org/10.5006/1.3278327.

[373] P. Rodrí, J.A. González, Use of the coulostatic method for measuring corrosion rates of embedded metal in concrete, Mag. Concr. Res. 46 (1994) 91–97. https://doi.org/10.1680/macr.1994.46.167.91.

[374] G.K. Glass, An assessment of the coulostatic method applied to the corrosion of steel in concrete, Corros. Sci. 37 (1995) 597–605. https://doi.org/10.1016/0010-938X(94)00156-Z.

[375] V. Feliu, J.A. Gonzàlez, S. Feliu, Modelling of the steel-concrete interface to obtain information on reinforcement bar corrosion, J. Appl. Electrochem. 35 (2005) 429–436. https://doi.org/10.1007/s10800-004-8348-0.

[376] S. Feliu, J.A. González, M.L. Escudero, S. Feliu, M.C. Andrade, Possibilities of the guard ring for electrical signal confinement in the polarization measurements of reinforcements, Corrosion. 46 (1990) 1015–1020. https://doi.org/10.5006/1.3585049.

[377] A. Fahim, Corrosion of reinforcing steel in concrete: monitoring techniques and mitigation

strategies, University of New Brunswick, 2018.

[378] P. V. Nygaard, M.R. Geiker, Measuring the corrosion rate of steel in concrete - effect of measurement technique, polarisation time and current, Mater. Corros. 63 (2012) 200–214. https://doi.org/10.1002/maco.201005792.

[379] S. Laurens, P. Hénocq, N. Rouleau, F. Deby, E. Samson, J. Marchand, B. Bissonnette, Steady-state polarization response of chloride-induced macrocell corrosion systems in steel reinforced concrete — numerical and experimental investigations, Cem. Concr. Res. 79 (2016) 272–290. https://doi.org/10.1016/j.cemconres.2015.09.021.

[380] U. Angst, M. Büchler, A new perspective on measuring the corrosion rate of localized corrosion, Mater. Corros. 71 (2020) 808–823. https://doi.org/10.1002/maco.201911467.

[381] D.G. John, P.C. Searson, J.L. Dawson, Use of AC impedance technique in studies on steel in concrete in immersed conditions, Br. Corros. J. 16 (1981) 102–106. https://doi.org/10.1179/000705981798275002.

[382] M.E. Orazem, B. Tribollet, Electrochemical Impedance Spectroscopy, 2nd Edition, Wiley, 2017.

[383] D. V. Ribeiro, J.C.C. Abrantes, Application of electrochemical impedance spectroscopy (EIS) to monitor the corrosion of reinforced concrete: A new approach, Constr. Build. Mater. 111 (2016) 98–104. https://doi.org/10.1016/j.conbuildmat.2016.02.047.

[384] G. Liu, Y. Zhang, M. Wu, R. Huang, Study of depassivation of carbon steel in simulated concrete pore solution using different equivalent circuits, Constr. Build. Mater. 157 (2017) 357–362. https://doi.org/10.1016/j.conbuildmat.2017.09.104.

[385] J.-P. Diard, B. Le Gorrec, C. Montella, Handbook of Electrochemical Impedance Spectroscopy - Electrical Circuits Containing CPEs, 2013.

[386] M.E. Orazem, B. Tribollet, Electrical Circuits, in: Electrochem. Impedance Spectrosc., John Wiley & Sons, Inc., Hoboken, NJ, USA, 2017: pp. 75–88. https://doi.org/10.1002/9781119363682.ch4.

[387] M.E. Orazem, B. Tribollet, Equivalent Circuit Analogs, in: Electrochem. Impedance Spectrosc., John Wiley & Sons, Inc., Hoboken, NJ, USA, 2017: pp. 191–206. https://doi.org/10.1002/9781119363682.ch9.

[388] M.E. Orazem, B. Tribollet, Constant-Phase Elements, in: Electrochem. Impedance Spectrosc., John Wiley & Sons, Inc., Hoboken, NJ, USA, 2017: pp. 395–419. https://doi.org/10.1002/9781119363682.ch14.

[389] M.R. Shoar Abouzari, F. Berkemeier, G. Schmitz, D. Wilmer, On the physical interpretation of constant phase elements, Solid State Ionics. 180 (2009) 922–927. https://doi.org/10.1016/j.ssi.2009.04.002.

[390] M. Keddam, H. Takenouti, X.R. Nóvoa, C. Andrade, C. Alonso, Impedance measurements on cement paste, Cem. Concr. Res. 27 (1997) 1191–1201. https://doi.org/10.1016/S0008-8846(97)00117-8.

[391] Z. Xu, P. Gu, P. Xie, J.J. Beaudoin, Application of A.C. impedance techniques in studies of porous cementitious materials: (II): Relationship between ACIS behavior and the porous microstructure, Cem. Concr. Res. 23 (1993) 853–862. https://doi.org/10.1016/0008-8846(93)90039-C.

[392] X. Hu, C. Shi, X. Liu, J. Zhang, G. de Schutter, A review on microstructural characterization of cement-based materials by AC impedance spectroscopy, Cem. Concr. Compos. 100 (2019) 1–

14. https://doi.org/10.1016/j.cemconcomp.2019.03.018.

[393] B. Díaz, X.R. Nóvoa, M.C. Pérez, Study of the chloride diffusion in mortar: A new method of determining diffusion coefficients based on impedance measurements, Cem. Concr. Compos. 28 (2006) 237–245. https://doi.org/10.1016/j.cemconsomp.2006.01.009.

[394] I. Sánchez, M.P. López, J.M. Ortega, M.Á. Climent, Impedance spectroscopy: An efficient tool to determine the non-steady-state chloride diffusion coefficient in building materials, Mater. Corros. 62 (2011) 139–145. https://doi.org/10.1002/maco.201005775.

[395] H. Mercado-Mendoza, S. Lorente, X. Bourbon, The diffusion coefficient of ionic species through unsaturated materials, Transp. Porous Media. 96 (2013) 469–481. https://doi.org/10.1007/s11242-012-0100-3.

[396] S. Chakri, I. Frateur, M.E. Orazem, E.M.M. Sutter, T.T.M. Tran, B. Tribollet, V. Vivier, Improved EIS analysis of the electrochemical behaviour of carbon steel in alkaline solution, Electrochim. Acta. 246 (2017) 924–930. https://doi.org/10.1016/j.electacta.2017.06.096.

[397] R. Vedalakshmi, S. Manoharan, H.-W. Song, N. Palaniswamy, Application of harmonic analysis in measuring the corrosion rate of rebar in concrete, Corros. Sci. 51 (2009) 2777–2789. https://doi.org/10.1016/j.corsci.2009.07.014.

[398] U.M. Angst, B. Elsener, Measuring corrosion rates: A novel AC method based on processing and analysing signals recorded in the time domain, Corros. Sci. 89 (2014) 307–317. https://doi.org/10.1016/j.corsci.2014.09.013.

[399] H. Wojtas, Determination of corrosion rate of reinforcement with a modulated guard ring electrode; analysis of errors due to lateral current distribution, Corros. Sci. 46 (2004) 1621–1632. https://doi.org/10.1016/j.corsci.2003.10.007.

[400] S. Feliu, J.A. González, J.M. Miranda, V. Feliu, Possibilities and problems of in situ techniques for measuring steel corrosion rates in large reinforced concrete structures, Corros. Sci. 47 (2005) 217–238. https://doi.org/10.1016/j.corsci.2004.04.011.

[401] A. Poursaee, C.M. Hansson, Galvanostatic pulse technique with the current confinement guard ring: The laboratory and finite element analysis, Corros. Sci. 50 (2008) 2739–2746. https://doi.org/10.1016/j.corsci.2008.07.017.

[402] P. V. Nygaard, M.R. Geiker, B. Elsener, Corrosion rate of steel in concrete: evaluation of confinement techniques for on-site corrosion rate measurements, Mater. Struct. 42 (2009) 1059–1076. https://doi.org/10.1617/s11527-008-9443-1.

[403] A. Clément, S. Laurens, G. Arliguie, F. Deby, Numerical study of the linear polarisation resistance technique applied to reinforced concrete for corrosion assessment, Eur. J. Environ. Civ. Eng. 16 (2012) 491–504. https://doi.org/10.1080/19648189.2012.668012.

[404] O. Gepraegs, C. Hansson, A comparative evaluation of three commercial unstruments for field measurements of reinforcing steel corrosion rates, J. ASTM Int. (2005). https://doi.org/10.1520/JAI11789.

[405] J. Marchand, S. Laurens, Y. Protière, E. Samson, A numerical study of polarization tests applied to corrosion in reinforced concrete, Spec. Publ. 312 (2016) 1–12.

[406] J. Zhang, P.J.M. Monteiro, H.F. Morrison, Noninvasive surface measurement of corrosion impedance of reinforcing bar in concrete—Part 1: Experimental results, ACI Mater. J. 98 (2001) 116–125. https://doi.org/10.14359/10195.

[407] S.S. Hubbard, J. Zhang, P.J.M. Monteiro, J.E. Peterson, Y. Rubin, Experimental detection of

reinforcing bar corrosion using nondestructive geophysical techniques, ACI Mater. J. 100 (2003) 501–510. https://doi.org/10.14359/12957.

[408] P.J.M. Monteiro, F. Morrison, W. Frangos, Non-destructive measurement of corrosion state of reinforcing steel in concrete, ACI Mater. J. 95 (1998) 704–709. https://doi.org/10.14359/414.

[409] J. Zhang, P.J.M. Monteiro, H.F. Morrison, Noninvasive surface measurement of corrosion impedance of reinforcing bar in concrete—Part 2: Forward modeling, ACI Mater. J. 99 (2002) 242–249. https://doi.org/10.14359/11969.

[410] J. Zhang, P.J.M. Monteiro, H.F. Morrison, M. Mancio, Noninvasive surface measurement of corrosion impedance of reinforcing bar in concrete—Part 3: Effect of geometry and material properties, ACI Mater. J. 101 (2004) 273–280.

[411] A. Fahim, P. Ghods, R. Alizaded, M. Salehi, S. Decarufel, CEPRA: A new test method for rebar corrosion rate measurement, Adv. Electrochem. Tech. Corros. Monit. Lab. Corros. Meas. STP1609 (2019) 59–80. https://doi.org/10.1520/STP160920170227.

[412] Y.-C. Lim, T. Noguchi, S.-W. Shin, Formulation of a nondestructive technique for evaluating steel corrosion in concrete structures, ISIJ Int. 49 (2009) 275–283. https://doi.org/10.2355/isijinternational.49.275.

[413] Y.-C. Lim, T. Noguchi, S. Shin, Corrosion evaluation by estimating the surface resistivity of reinforcing bar, J. Adv. Concr. Technol. 8 (2010) 113–119. https://doi.org/10.3151/jact.8.113.

[414] C. Andrade, I. Martínez, M. Castellote, Feasibility of determining corrosion rates by means of stray current-induced polarisation, J. Appl. Electrochem. 38 (2008) 1467–1476. https://doi.org/10.1007/s10800-008-9591-6.

[415] C. Andrade, I. Martínez, Metal corrosion rate determination of different solutions and reinforced concrete specimens by means of a noncontacting corrosion method, Corrosion. 66 (2010) 056001-056001–10. https://doi.org/10.5006/1.3430465.

[416] C. Andrade, J. Sanchez, I. Martinez, N. Rebolledo, Analogue circuit of the inductive polarization resistance, Electrochim. Acta. 56 (2011) 1874–1880. https://doi.org/10.1016/j.electacta.2010.09.057.

[417] M. Keddam, X.R. Nóvoa, V. Vivier, The concept of floating electrode for contact-less electrochemical measurements: Application to reinforcing steel-bar corrosion in concrete, Corros. Sci. 51 (2009) 1795–1801. https://doi.org/10.1016/j.corsci.2009.05.006.

[418] M. Keddam, X.R. Nóvoa, B. Puga, V. Vivier, Impedance based method for non-contact determination of the corrosion rate in buried metallic structures, Eur. J. Environ. Civ. Eng. 15 (2011) 1097–1103. https://doi.org/10.1080/19648189.2011.9695296.

[419] J. Yu, A. Sasamoto, M. Iwata, Wenner method of impedance measurement for health evaluation of reinforced concrete structures, Constr. Build. Mater. 197 (2019) 576–586. https://doi.org/10.1016/j.conbuildmat.2018.11.121.

[420] C.L. Alexander, M.E. Orazem, Indirect electrochemical impedance spectroscopy for corrosion detection in external post-tensioned tendons: 1. Proof of concept, Corros. Sci. 164 (2020) 108331. https://doi.org/10.1016/j.corsci.2019.108331.

[421] C.L. Alexander, M.E. Orazem, Indirect impedance for corrosion detection of external post-tensioned tendons: 2. Multiple steel strands, Corros. Sci. 164 (2020) 108330. https://doi.org/10.1016/j.corsci.2019.108330.

[422] F. Abdulsamad, N. Florsch, Assessing the high frequency behavior of non-polarizable

electrodes for spectral induced polarization measurements, J. Appl. Geophys. 135 (2016) 449–455. https://doi.org/10.1016/j.jappgeo.2016.01.001.

[423] C.L. Alexander, Impedance spectroscopy: The influence of surface heterogeneity and application to corrosion monitoring of bridge tendons, University of Florida, 2017.

[424] R. Rodrigues, J. Gance, S. Gaboreau, I. Ignatiadis, S. Betelu, Electrochemical Measurement System and Method for Monitoring a Concrete Structure, EP19188380, 2019.

[425] C. Andrade, J.A. González, Quantitative measurements of corrosion rate of reinforcing steels embedded in concrete using polarization resistance measurements, Mater. Corros. 29 (1978) 515–519. https://doi.org/10.1002/maco.19780290804.

[426] G. Song, Theoretical analysis of the measurement of polarisation resistance in reinforced concrete, Cem. Concr. Compos. 22 (2000) 407–415. https://doi.org/10.1016/S0958-9465(00)00040-8.

[427] C. Alonso, C. Andrade, X.R. Nóvoa, M. Izquierdo, M.C. Pérez, Effect of protective oxide scales in the macrogalvanic behaviour of concrete reinforcements, Corros. Sci. 40 (1998) 1379–1389. https://doi.org/10.1016/S0010-938X(98)00040-7.

[428] D.A. Jones, N.D. Greene, Electrochemical measurement of low corrosion rates, Corrosion. 22 (1966) 198–205. https://doi.org/10.5006/0010-9312-22.7.198.

[429] D.A. Jones, Principles and Prevention of Corrosion, 2nd Edition, Prentice Hall, Upper Saddle River, N.J., 1996.

[430] E. Gileadi, E. Kirowa-Eisner, Some observations concerning the Tafel equation and its relevance to charge transfer in corrosion, Corros. Sci. 47 (2005) 3068–3085. https://doi.org/10.1016/j.corsci.2005.05.044.

[431] J. Ge, O.B. Isgor, Effects of Tafel slope, exchange current density and electrode potential on the corrosion of steel in concrete, Mater. Corros. 58 (2007) 573–582. https://doi.org/10.1002/maco.200604043.

[432] J.A. González, J.M. Miranda, N. Birbilis, S. Feliu, Electrochemical techniques for studying corrosion of reinforcing steel: Limitations and advantages, Corrosion. 61 (2005) 37–50. https://doi.org/10.5006/1.3278158.

[433] B. Yu, L. Yang, M. Wu, B. Li, Practical model for predicting corrosion rate of steel reinforcement in concrete structures, Constr. Build. Mater. 54 (2014) 385–401. https://doi.org/10.1016/j.conbuildmat.2013.12.046.

[434] J.A. González, A. Molina, M.L. Escudero, C. Andrade, Errors in the electrochemical evaluation of very small corrosion rates—I. Polarization resistance method applied to corrosion of steel in concrete, Corros. Sci. 25 (1985) 917–930. https://doi.org/10.1016/0010-938X(85)90021-6.

[435] I. Martínez, C. Andrade, Polarization resistance measurements of bars embedded in concrete with different chloride concentrations: EIS and DC comparison, Mater. Corros. 62 (2011) 932–942. https://doi.org/10.1002/maco.200905596.

[436] J.A. González, A. Molina, M.L. Escudero, C. Andrade, Errors in the electrochemical evaluation of very small corrosion rates—II. Other electrochemical techniques applied to corrosion of steel in concrete, Corros. Sci. 25 (1985) 519–530. https://doi.org/10.1016/0010-938X(85)90030-7.

[437] M. Kouřil, P. Novák, M. Bojko, Limitations of the linear polarization method to determine stainless steel corrosion rate in concrete environment, Cem. Concr. Compos. 28 (2006) 220–

225. https://doi.org/10.1016/j.cemconcomp.2006.01.007.

[438] U. Angst, M. Büchler, On the applicability of the Stern-Geary relationship to determine instantaneous corrosion rates in macro-cell corrosion, Mater. Corros. 66 (2015) 1017–1028. https://doi.org/10.1002/maco.201407997.

[439] B. Elsener, Corrosion rate of steel in concrete—Measurements beyond the Tafel law, Corros. Sci. 47 (2005) 3019–3033. https://doi.org/10.1016/j.corsci.2005.06.021.

[440] C. Andrade, C. Alonso, J. Sarría, Corrosion rate evolution in concrete structures exposed to the atmosphere, Cem. Concr. Compos. 24 (2002) 55–64. https://doi.org/10.1016/S0958-9465(01)00026-9.

[441] C. Andrade, Propagation of reinforcement corrosion: principles, testing and modelling, Mater. Struct. 52 (2019) 2. https://doi.org/10.1617/s11527-018-1301-1.

[442] C. Andrade, J. Sarría, C. Alonso, Relative humidity in the interior of concrete exposed to natural and artificial weathering, Cem. Concr. Res. 29 (1999) 1249–1259. https://doi.org/10.1016/S0008-8846(99)00123-4.

[443] J. Jiang, Y. Yuan, Development and prediction strategy of steel corrosion rate in concrete under natural climate, Constr. Build. Mater. 44 (2013) 287–292. https://doi.org/10.1016/j.conbuildmat.2013.03.033.

[444] T. Jaśniok, M. Jaśniok, Influence of rapid changes of moisture content in concrete and temperature on corrosion rate of reinforcing steel, Procedia Eng. 108 (2015) 316–323. https://doi.org/10.1016/j.proeng.2015.06.153.

[445] C. Andrade, A. Castillo, Evolution of reinforcement corrosion due to climatic variations, Mater. Corros. 54 (2003) 379–386. https://doi.org/10.1002/maco.200390087.

[446] C. Boschmann Käthler, U.M. Angst, G. Ebell, B. Elsener, Chloride-induced reinforcement corrosion in cracked concrete: the influence of time of wetness on corrosion propagation, Corros. Eng. Sci. Technol. (2020) 1–10. https://doi.org/10.1080/1478422X.2020.1789371.

[447] V. Bouteiller, J.-F. Cherrier, V. L'Hostis, N. Rebolledo, C. Andrade, E. Marie-Victoire, Influence of humidity and temperature on the corrosion of reinforced concrete prisms, Eur. J. Environ. Civ. Eng. 16 (2012) 471–480. https://doi.org/10.1080/19648189.2012.668004.

[448] B. Yu, J. Liu, B. Li, Improved numerical model for steel reinforcement corrosion in concrete considering influences of temperature and relative humidity, Constr. Build. Mater. 142 (2017) 175–186. https://doi.org/10.1016/j.conbuildmat.2017.03.045.

[449] A. Chauhan, U.K. Sharma, Influence of temperature and relative humidity variations on non-uniform corrosion of reinforced concrete, Structures. 19 (2019) 296–308. https://doi.org/10.1016/j.istruc.2019.01.016.

[450] Y.A. Villagrán Zaccardi, A. Bértora, A.A. Di Maio, Temperature and humidity influences on the on-site active marine corrosion of reinforced concrete elements, Mater. Struct. 46 (2013) 1527–1535. https://doi.org/10.1617/s11527-012-9994-z.

[451] V. Bouteiller, E. Marie-Victoire, C. Cremona, Mathematical relation of steel thickness loss with time related to reinforced concrete contaminated by chlorides, Constr. Build. Mater. 124 (2016) 764–775. https://doi.org/10.1016/j.conbuildmat.2016.07.078.

[452] A. Michel, P.V. Nygaard, M.R. Geiker, Experimental investigation on the short-term impact of temperature and moisture on reinforcement corrosion, Corros. Sci. 72 (2013) 26–34. https://doi.org/10.1016/j.corsci.2013.02.006.

[453] U.M. Angst, Durable concrete structures: Cracks & corrosion and corrosion & cracks, in: G. Pijaudier-Cabot, P. Grassl, C. La Borderi (Eds.), 10th Int. Conf. Fract. Mech. Concr. Concr. Struct., Bayonne, France, 2019: pp. 1–10. https://doi.org/10.21012/FC10.233307.

[454] M. Jaśniok, T. Jaśniok, Evaluation of maximum and minimum corrosion rate of steel rebars in concrete structures, based on laboratory measurements on drilled cores, Procedia Eng. 193 (2017) 486–493. https://doi.org/10.1016/j.proeng.2017.06.241.

[455] D. Breysse, G. Klysz, X. Dérobert, C. Sirieix, J.F. Lataste, How to combine several non-destructive techniques for a better assessment of concrete structures, Cem. Concr. Res. 38 (2008) 783–793. https://doi.org/10.1016/j.cemconres.2008.01.016.

[456] G. Loreto, M. Di Benedetti, A. De Luca, A. Nanni, Assessment of reinforced concrete structures in marine environment: a case study, Corros. Rev. 37 (2019) 57–69. https://doi.org/10.1515/corrrev-2018-0046.

[457] L. Sadowski, Methodology for assessing the probability of corrosion in concrete structures on the basis of half-cell potential and concrete resistivity measurements, Sci. World J. 2013 (2013) 714501. https://doi.org/10.1155/2013/714501.

[458] V. Garnier, B. Piwakowski, O. Abraham, G. Villain, C. Payan, J.F. Chaix, Acoustic techniques for concrete evaluation: Improvements, comparisons and consistency, Constr. Build. Mater. 43 (2013) 598–613. https://doi.org/10.1016/j.conbuildmat.2013.01.035.

[459] P. Ziehl, M. ElBatanouny, Acoustic emission monitoring for corrosion damage detection and classification, in: Corros. Steel Concr. Struct., Woodhead Publishing, 2016: pp. 193–209. https://doi.org/10.1016/B978-1-78242-381-2.00010-9.

[460] C. Van Steen, L. Pahlavan, M. Wevers, E. Verstrynge, Localisation and characterisation of corrosion damage in reinforced concrete by means of acoustic emission and X-ray computed tomography, Constr. Build. Mater. 197 (2019) 21–29. https://doi.org/10.1016/j.conbuildmat.2018.11.159.

[461] M.R. Clark, D.M. McCann, M.C. Forde, Application of infrared thermography to the non-destructive testing of concrete and masonry bridges, NDT E Int. 36 (2003) 265–275. https://doi.org/10.1016/S0963-8695(02)00060-9.

[462] X. Dérobert, Z.M. Sbartaï, J. Dumoulin, Electromagnetic Methods, in: Non-Destructive Test. Eval. Civ. Eng. Struct., Elsevier, 2018: pp. 87–137. https://doi.org/10.1016/B978-1-78548-229-8.50003-0.

[463] W. Wai-Lok Lai, X. Dérobert, P. Annan, A review of ground penetrating radar application in civil engineering: A 30-year journey from locating and testing to imaging and diagnosis, NDT E Int. 96 (2018) 58–78. https://doi.org/10.1016/j.ndteint.2017.04.002.

[464] F. Tosti, C. Ferrante, Using ground penetrating radar methods to investigate reinforced concrete structures, Surv. Geophys. (2019) 1–46. https://doi.org/10.1007/s10712-019-09565-5.

[465] X. Dérobert, J. Iaquinta, G. Klysz, J.-P. Balayssac, Use of capacitive and GPR techniques for the non-destructive evaluation of cover concrete, NDT E Int. 41 (2008) 44–52. https://doi.org/10.1016/j.ndteint.2007.06.004.

[466] S. Hong, H. Wiggenhauser, R. Helmerich, B. Dong, P. Dong, F. Xing, Long-term monitoring of reinforcement corrosion in concrete using ground penetrating radar, Corros. Sci. 114 (2017) 123–132. https://doi.org/10.1016/j.corsci.2016.11.003.

[467] M. Fares, Y. Fargier, G. Villain, X. Derobert, S. Palma Lopes, Determining the permittivity profile inside reinforced concrete using capacitive probes, NDT E Int. 79 (2016) 150–161. https://doi.org/10.1016/j.ndteint.2016.01.002.

[468] A. Voss, P. Hosseini, M. Pour-Ghaz, M. Vauhkonen, A. Seppänen, Three-dimensional electrical capacitance tomography – A tool for characterizing moisture transport properties of cement-based materials, Mater. Des. 181 (2019) 107967. https://doi.org/10.1016/j.matdes.2019.107967.

[469] R. du Plooy, G. Villain, S. Palma Lopes, A. Ihamouten, X. Dérobert, B. Thauvin, Electromagnetic non-destructive evaluation techniques for the monitoring of water and chloride ingress into concrete: a comparative study, Mater. Struct. 48 (2015) 369–386. https://doi.org/10.1617/s11527-013-0189-z.

[470] X. Dérobert, J.F. Lataste, J.-P. Balayssac, S. Laurens, Evaluation of chloride contamination in concrete using electromagnetic non-destructive testing methods, NDT E Int. 89 (2017) 19–29. https://doi.org/10.1016/j.ndteint.2017.03.006.

[471] Y. Seguí Femenias, U. Angst, F. Moro, B. Elsener, Development of a novel methodology to assess the corrosion threshold in concrete based on simultaneous monitoring of pH and free chloride concentration, Sensors. 18 (2018) 3101. https://doi.org/10.3390/s18093101.

[472] Z. Zhang, J. Hu, Y. Ma, Y. Wang, H. Huang, Z. Zhang, J. Wei, S. Yin, Q. Yu, A state-of-the-art review on Ag/AgCl ion-selective electrode used for non-destructive chloride detection in concrete, Compos. Part B Eng. (2020) 108289. https://doi.org/10.1016/j.compositesb.2020.108289.

[473] O. Anterrieu, B. Giroux, E. Gloaguen, C. Carde, Non-destructive data assimilation as a tool to diagnose corrosion rate in reinforced concrete structures, J. Build. Eng. 23 (2019) 193–206. https://doi.org/10.1016/j.jobe.2019.01.033.